The Thesis committee for Guangyao Wang

Certifies that this is the approved version of the following thesis：

PIV Experiment and CFD Simulation of Flow around Cylinder

APPROVED BY

SUPERVISING COMMITTEE:

Spyridon A. Kinnas, Supervisor

David G. Bogard

PIV Experiment and CFD Simulation of Flow around Cylinder

by

Guangyao Wang, B.S.E.

Thesis

Presented to the Faculty of the Graduate School of

The University of Texas at Austin

in Partial Fulfillment

of the Requirements

for the Degree of

MASTER OF SCIENCE IN ENGINEERING

The University of Texas at Austin

May 2015

Dedicated to my family for their enduring support, especially my father, Yanguo, my mother, Guiying, my wife, Li, and my sister, Manman.

Acknowledgment

I wish to thank the people who helped me make the work possible: my advisor, Dr. Kinnas, the members of the Ocean Engineering Group, especially Ye Tian, Yiran Su, Weikang Du and Hongyang Fan. I would also like to thank Dr. Bogard for his thoughts and suggestions as the second reader.

PIV Experiment and CFD Simulation of Flow around Cylinder

by

Guangyao Wang, M.S.E.

The University of Texas at Austin, 2015

SUPERVISOR: Spyridon A. Kinnas

This work focuses on the study of flow around cylinder with both Particle Image Velocimetry (PIV) experiment and Computational Fluid Dynamics (CFD) simulation. PIV measurements of the flow field at the downstream of the cylinder are first presented. The boundary conditions for CFD simulations are measured in the PIV experiment. Then the PIV flow is compared with both RANS (2D) and LES (3D) simulations performed with ANSYS Fluent. The velocity vector fields and time histories of velocity are analyzed. In addition, the time-averaged velocity profiles and Reynolds stresses are analyzed. It is found that, in general, LES (3D) gives a better prediction of flow characteristics than RANS (2D).

Table of Contents

List of Figures

List of Tables

Nomenclature

C_x	Inline force coefficient $C_x = F/(1/2\rho U_m^2 D)$
C_D	Drag coefficient
C_M	Inertia coefficient
D	Diameter of cylinder
F	Total inline force on the cylinder
F_D	Drag force
F_I	Inertial force
KC	Keulegan-Carpernter Number $KC = U_m T/D$
Re	Reynolds number $Re = U_m D/\nu$
T	Period of flow velocity
$\dot{u}$	Flow acceleration
u	Flow velocity
U_m	Amplitude of oscillating flow velocity
ρ	Density of fluid
ω	Frequency of flow velocity $\omega = 2\pi/T$
ν	Kinematic viscosity

Chapter 1 Introduction and literature review

1.1 Introduction

Turbulent flow around a cylinder is a complex phenomenon within fluid mechanics, to which a lot of researchers have devoted efforts. When the natural frequency of the cylinder approaches that of the vortex shedding at the downstream of the cylinder, vortex-induced vibrations (VIV) occur and can lead to fatigue-driven failure(Stetson 2013). It is meaningful to model VIV, and there are a large number of studies addressing the problem of VIV prediction.

In the field of ocean engineering, VIV is a very common phenomenon. When the flow of ocean currents passes large aspect ratio cylinders, such as risers, pipelines and cables，unexpected failure of such cylinders can have a catastrophic impact. Although few examples of cylinder failure due to VIV exist in the literature, VIV is still regularly considered when designing such cylinders. A lot of experiments have been conducted on the large aspect ratio cylinders in the past several years. While these experiments contribute a lot to the research of VIV, experiments have limitations as well, such as devices availability, capacity limits, model scale limit, difficulty of current profile generation, cost concerns, etc. (Huang 2011). Under such conditions, Computational Fluid Dynamics (CFD) can be an effective alternative to experiments in studying large aspect ratio cylinders.

1.2 Literature Review

There are many experimental studies on the vortex-induced vibration of cylinders. Bearman (1984) presented a comprehensive review of experimental studies related to vortex shedding. The principal reason for vortex shedding is the presence of two shear layers. He also discussed the absence of two-dimensionality in the vortex shedding from a 2D body in a uniform flow. The unsteady quantities (e.g., surface pressure) which are related to vortex shedding are not constant in the spanwise direction of the body. Three dimensional features naturally arise in the VIV problem as the real domain is considered as spanwise extended (Gabbai and Benaroya 2005).

Williamson (1988) discussed the transition to three-dimensionality in the near wake of a cylinder. When Reynolds number is greater than about 178, the three-dimensional structures in the wake will occur. The main reason for the appearance of three dimensional structures is the deformation of the primary wake vortices. The transition to three-dimensionality is related to two successive transitions, which are characterized by a discontinuity in the Strouhal-Reynolds number relationship. The relationship between Strouhal number and Reynolds number is presented in Figure 1.1. The first discontinuity occurs when $170 < Re < 180$ and it is related with the transition from periodic and laminar vortex shedding to shedding involving the formation of vortex loop. When $225 < Re < 270$, the second discontinuity appears, which is associated with the transition from vortex loops to finer-scale streamwise vortices. It is found that the first discontinuity is hysteretic while the second one is not.

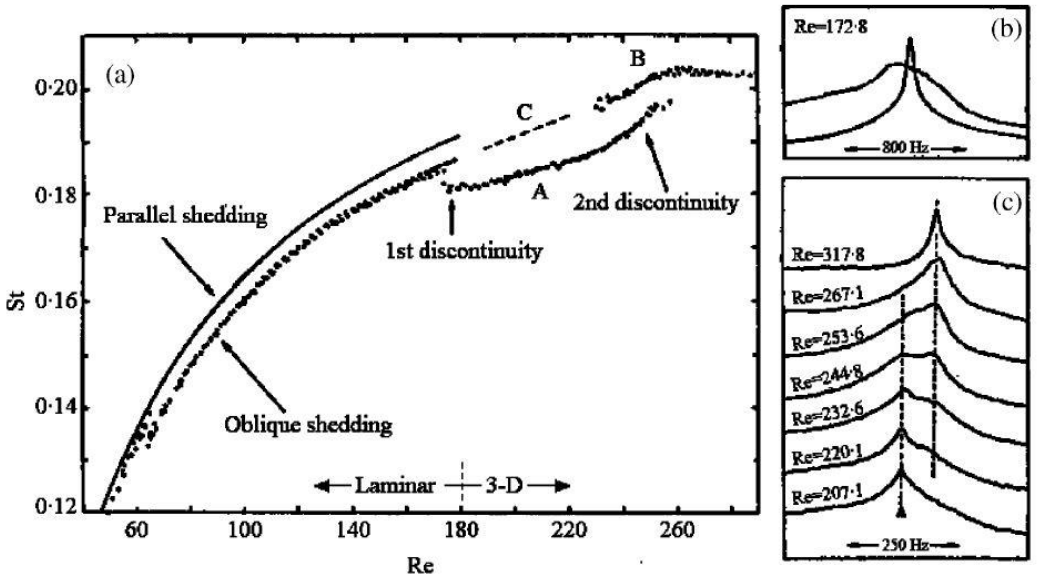

Figure 1.1(a) Variation in Strouhal number as a function of Reynolds number; (b) frequency spectra at first discontinuity; (c) frequency spectra at second discontinuity (William 1988)

Particle image velocimetry (PIV) is an optical method of flow visualization, which has been widely applied in education and research. It is able to capture instantaneous velocity and related properties in fluid flow. Wilde, Huijsmans et al. (2006) used the three-dimensional PIV system to investigate the complex three-dimensional vortex flow around the cylinder at high Reynolds numbers. The Reynolds number in the experiment ranged from 40,000 to 200,000. They observed an important three-dimensionality of the flow in the center of the vortex. Stetson (2013) applied the two-dimensional PIV system to measure the flow field around the fixed cylinder with and without fairing. Kang and Jia (2013) presented the results of experiments on the vortex-induced vibration of a horizontal cylinder with two degrees of freedom. The vibration of the cylinder in the in-line direction

was found to have four frequencies. Wang, Li et al. (2014) used an X-wire, a novel phase locked particle image velocimetry (PIV), and an acceleration sensor at a low speed wind tunnel to investigate the wake structures and VIV of a spring-supported cylinder. The 2P (two pairs) vortex mode rather than S (single vortex) mode exists in the wake. It shows that after a strong interaction between the cylinder and fluid, the cylinder vibration and vortex shedding come to a stable state.

As a trend in recent years, people are paying more and more attention to the CFD approach with the development of computational capability. More importantly, the CFD approach is able to provide the flow field which is necessary and significant to understand the phenomenon of VIV. Thus, it is usually regarded as a good alternative and valuable compensation to the water basin experiments. Al-Jamal and Dalton (2004) presented the results of hydrodynamic variables by performing a 2D LES study of the VIV response of a circular cylinder at a Reynolds number of 8,000 with a range of damping ratios and natural frequencies. They thought that two dimensional CFD could be accurate enough to capture the hydrodynamic variables, i.e. drag and lift coefficients, based on the comparison with three dimensional CFD.

Asyikin (2012) performed the 2D RANS simulation to investigate the flow characteristics and VIV of cylinder due to the incompressible laminar and turbulent flow at Reynolds number 40, 100, 200 and 1,000. The drag and lift coefficients showed a good agreement with the previous studies. Stetson (2013) performed both 2D RANS and LES simulations of flow past cylinder with and without fairing and compared the results with the PIV experiment. The 2D CFD was able to capture the period of vortex shedding.

However, it cannot provide a good prediction of the flow field characteristics, such as time history of velocity at specific points, vortex patterns, etc.

The application of the 3D CFD approach to cylinder VIV study is still a relatively new research area due to its onerous computational requirements. Blackburn, Govardhan et al. (2001) applied both the experimental method and CFD (2D and 3D) to investigate VIV. They thought that the two dimensional simulations were inadequate for the task of predicting the full nature both of the response envelope and of vortex shedding, even at low Reynolds number. Shur, Spalart et al. (2005) applied three-dimensional URANS to investigate the flow past a cylinder. It is shown that the three-dimensional URANS is much more accurate than two-dimensional URANS. Also URANS is found to be sensitive to the spanwise period and turbulence models. Verma and Mahesh (2012) presented the results of 3D LES simulation of flow past fixed cylinder, including time-averaged velocities and Reynolds stresses. Huang (2011) presented a CFD approach for 3D simulation of long risers. The flow field vorticities, riser motion trajectories, modal components, etc. are studied. It is found that the vortex shedding pattern in the shear current is different from the uniform flow.

Usually, offshore structures are subject to waves or currents. When the vertical velocity component is neglected, the wave flow around a cylinder is very similar to a sinusoidally oscillating planar flow around a cylinder (Zhou and Graham 2000). For a planar oscillating flow around a cylinder, there are numerous experimental and numerical studies in the past few decades, which provide the basis to understand more complex flows.

The in-line force F_x on a cylinder can be represented as a summation of drag and inertial forces, which is known as Morison's equation (Morison, Johnson et al. 1950)

$$F_X = \underbrace{C_M \rho \frac{\pi}{4} D^2 \dot{u}}_{F_I} + \underbrace{C_D \frac{1}{2} \rho D u |u|}_{F_D} \tag{1.1}$$

Where, F_x is the total in-line force on the cylinder, $\dot{u} \equiv \frac{du}{dt}$ is the flow acceleration, C_M is the inertia coefficient, C_D is the drag coefficient, ρ is the density of the fluid, D is the diameter of the cylinder, F_I is the inertial force, and F_D is the drag force. There are two important numbers, $Reynolds\ number(Re) = \frac{U_m D}{\nu}$, where U_m is the amplitude of velocity of the oscillatory flow, and $Keulegan - Carpenter\ number(KC) = \frac{U_m T}{D}$ ($T = \frac{2\pi}{\omega}$), where T is the period of the oscillating flow. C_D and C_M are functions of both Re and KC (Keulegan, Keulegan et al. 1958).

When the records of flow characteristics are known, it is possible to determine Morison coefficients C_D and C_M in any of the potential domains of investigation. The time domain solutions can be achieved by least squares error fitting methods. The recorded force and particle kinematics can be used in establishing the fit to Morison's equation. (Burrows, Tickell et al. 1997).Wade and Dwyer (1978) presented four methods of wave force calculation according to Morison's equation. The seemingly minor error differences among the four methods result in a significant variation of the results. Garrison (1980) discussed the relationship between fixed and oscillating cylinders. The oscillatory motion of a cylinder in still water is kinematically identical to oscillating the fluid past the fixed

cylinder. Thus data from both types of experiments are applicable to the wave force situation.

For most offshore structures in the extreme design environment, Reynolds number are well into the post-critical flow regime, where C_D for cylinders is independent of Reynolds number. American Petroleum Institution presented the suggested values of both drag and inertia coefficients for a wide range of KC numbers (0<KC<100) (RP2A-WSD 2000).

1.3 Objectives

The objective of this thesis is to study the flow around a cylinder with both PIV experiment and CFD simulations. In the PIV experiment, measurements will be performed around the cylinder and at the boundaries of the flow field. In CFD simulations, both RANS (2D) and LES (3D) will be adopted and compared with PIV experiment. In addition, the assessment of Morison's equation will be discussed. Results from CFD simulations and Morison's equation will be compared.

Chapter 2 Particle Image Velocimetry

2.1 Methods

The PIV experiment is performed with the open channel flume in the Fluids and Hydraulics Lab at the University of Texas at Austin (Figure 2.1). The width of the flume is 0.3m. The flow field downstream of the cylinder is captured with a two-dimensional PIV system which is manufactured by Dantec Dynamics. The PIV system is comprised of a Nd:YAG laser and a NanoSense Mk III CCD camera taking images at 1000Hz in single frame mode. The water is seeded with 10 μm diameter, silver-coated, hollow glass spheres. A uniform inflow (0.35m/s) is used around a cylinder with 0.018m diameter (Re=6300). The cylinder is set across the span of the flume, perpendicular to the flow and above the boundary layer (image of cylinder during measurement is shown in Figure 2.2 and schematic of cylinder in flume is shown in Figure 2.3). For each run, the length-scale (for correlating velocity vectors from the images) is calibrated with the image of a ruler in the path of the laser (Figure 2.4). When measuring the flow field, the ruler is removed (Figure 2.5).

To determine the best laser shooting frequency, several values are tested: 100Hz, 200Hz, 500Hz, and 1000Hz. The results show that a shooting frequency of 1000Hz in single frame mode best captures the flow at Re=6,300.

Due to the limitation of the mobility of the laser beam, we can only measure a part of the region above the cylinder and the whole region under the cylinder (Figure 2.6). For

all measurements, due to the limitation of storage of the camera, the measured time is 3 seconds, so there are 3,000 images taken in each measurement.

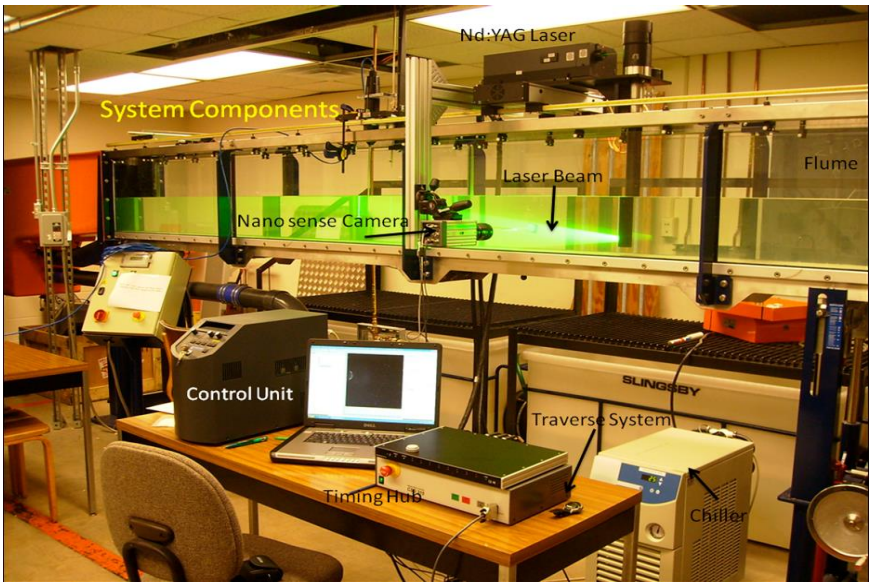

Figure 2.1 Open channel flume and Dantec PIV system setup

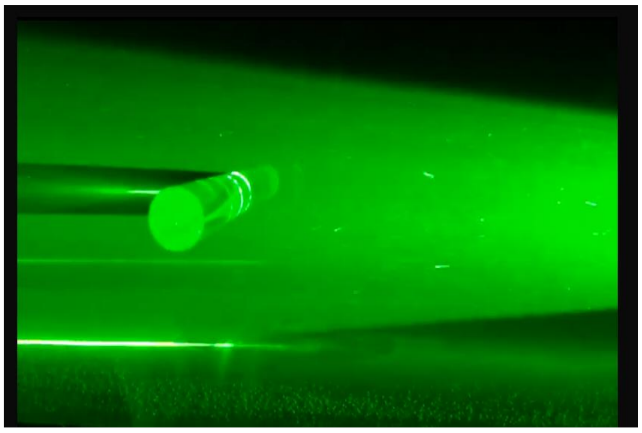

Figure 2.2 Image of cylinder during measurement

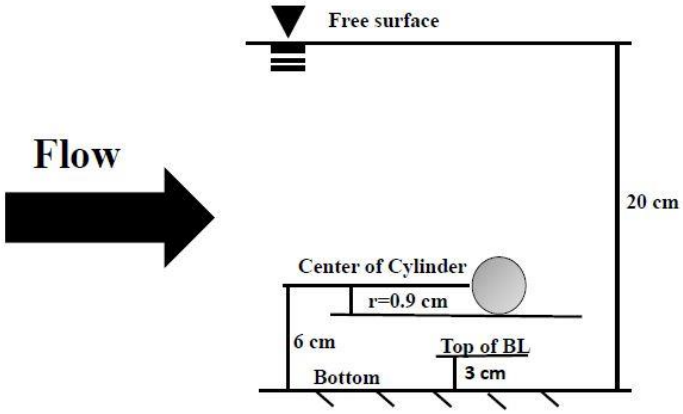

Figure 2.3 Schematic of cylinder in flume

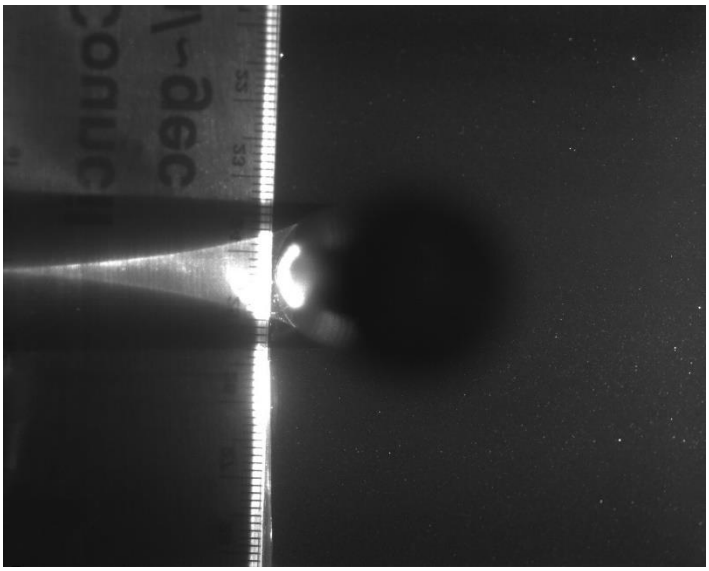

Figure 2.4 PIV calibration image

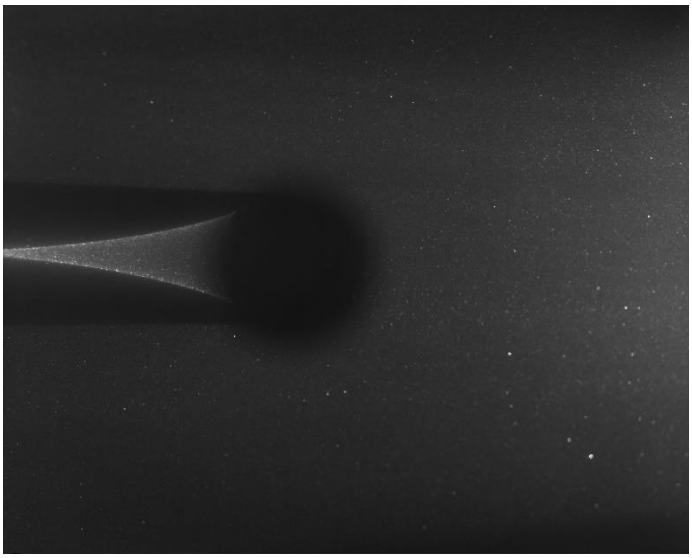

Figure 2.5 Image of particles without the ruler

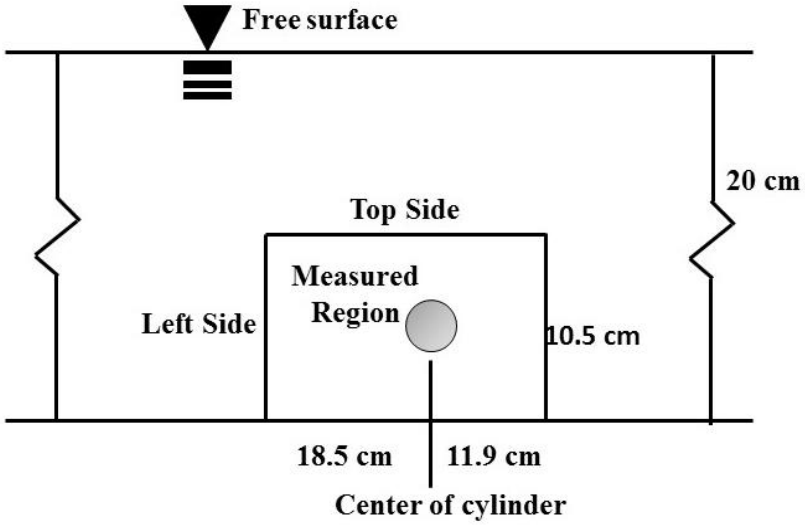

Figure 2.6 Schematic of measured region

In the CFD simulations, the boundary conditions of the simulated region are required. So, measurements are performed at both left and top sides of the region (Figure 2.7). Due to the shadow of cylinder, the light behind cylinder is not strong enough to ensure a good quality of the measurement. Thus, there is no cylinder when measuring the left side. To make sure that the effect of cylinder on the inflow is negligible, the velocity is checked using potential flow theory. According to the potential flow theory, the flow velocities are given as

$$u_r = U(1 - \frac{a^2}{r^2})cos\theta \tag{2.1}$$

$$u_\theta = -U(1 + \frac{a^2}{r^2})sin\theta \tag{2.2}$$

Where, u_r is the radial velocity, u_θ is the tangential velocity, U is the free stream velocity, r is the distance between the point and center of cylinder and a is the radius of cylinder. In this study, $\frac{a^2}{r^2} \approx 0.01$, so $1 - \frac{a^2}{r^2} \approx 1$ and $1 + \frac{a^2}{r^2} \approx 1$. So that the effect of the cylinder on the inflow is negligible. To make sure that the data are continuous, there are overlapping regions between adjacent measured regions. The region which we are really interested in is the one around the cylinder, especially downstream of the cylinder. Finally, the flow field around the cylinder is measured (Figure 2.8). To ensure the quality of data, two measurements are performed at the same region around the cylinder.

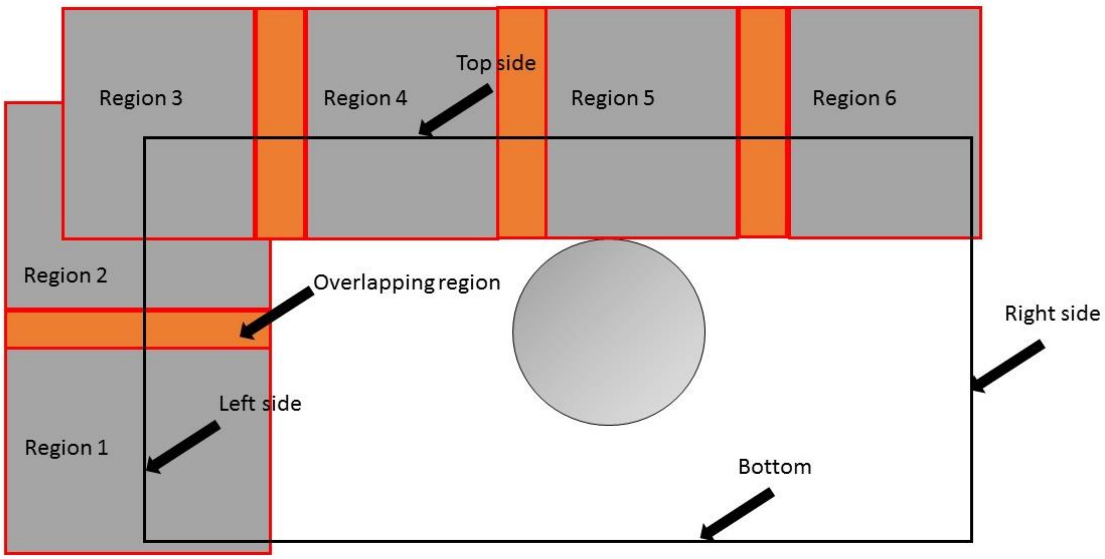

Figure 2.7 Measurements of the left and top sides

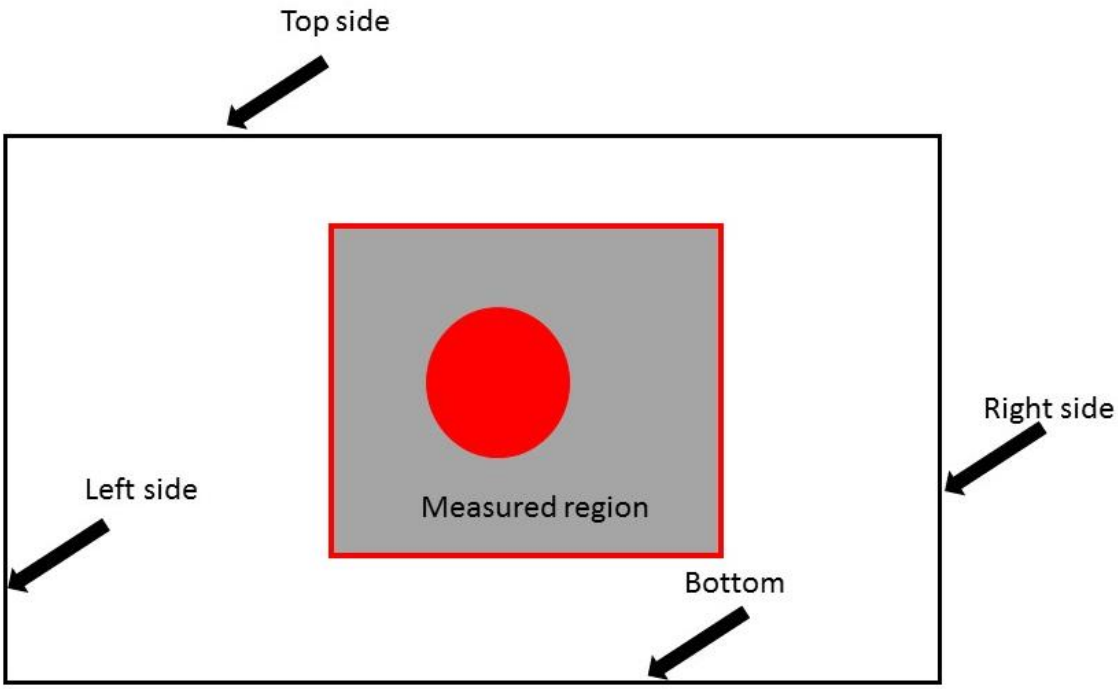

Figure 2.8 Measured region around cylinder

2.2 Data Processing

The flow images are analyzed to create flow velocity vector fields in Dantec Dynamics PIV software, Dynamic Studio, version 3.40.82. Based on the suggestions provided by the previous user of PIV system, the adaptive PIV method is adopted to generate velocity vectors from the PIV images even though it is considerably more time consuming than other methods. The adaptive PIV method iteratively optimizes the size and shape of each interrogation area to better adapt to local flow gradients and seeding densities. The following settings are found to provide accurate velocity fields as suggested by Dantec Dynamics: 16×16 pixel grid step size, a low pass Gaussian filter (k=3), peak height ratio validation (minimum=1.15), and S/N ratio (4.0). Universal outlier detection is not optional with the method and used a 5 pixel by 5 pixel neighborhood with an acceptance limit of 2. Vectors are validated after the last iteration. Less finely resolved and less filtered methods are found to produce too many erroneous vectors. More finely resolved or more filtered methods do not greatly increase the accuracy with which the flow are represented relative to the increase in computational time required. Also, over filtering leads to the removal of data and flow-complexity. Settings are adjusted to avoid this.

The mean horizontal and vertical velocity profiles are shown for the inflow and top side (Figure 2.9, Figure 2.10, Figure 2.11 and Figure 2.12). It is shown that due to the presence of cylinder, the horizontal velocity at the top side increases. In addition, at the upstream of cylinder, the flow goes away from the centerline of cylinder, and, at the downstream of cylinder, the flow goes towards the centerline.

Figure 2.13 shows a masked image used for calculating vectors. A snapshot of the flow field round the cylinder is shown in Figure 2.14.

The time history of horizontal velocity is shown for a point of the inflow (Figure 2.15). The mean horizontal velocity is 0.35m/s and the standard deviation is 0.007m/s. The standard deviation of 0.007m/s is $\approx 2\%$ of the mean horizontal velocity. This value is used in CFD runs as the free stream turbulence intensity (specified in Ansys Fluent as turbulence intensity, two percent, rather than as turbulence kinetic energy, k). To verify that the turbulence intensity is appropriate, the result from the experiment done by Stetson (2013) is shown in Figure 2.16, which also shows a similar value of the turbulence intensity. By using this value as the free stream turbulence parameter, we make the assumption that the standard deviation from the mean represents flow turbulence; some of the variation from mean flow could instead represent inaccuracy in the PIV measurement.

From the horizontal velocity profile of the inflow, we can deduce that the thickness of the boundary layer in the measured region is about 3cm. So, the vortex shedding occurs above the boundary layer.

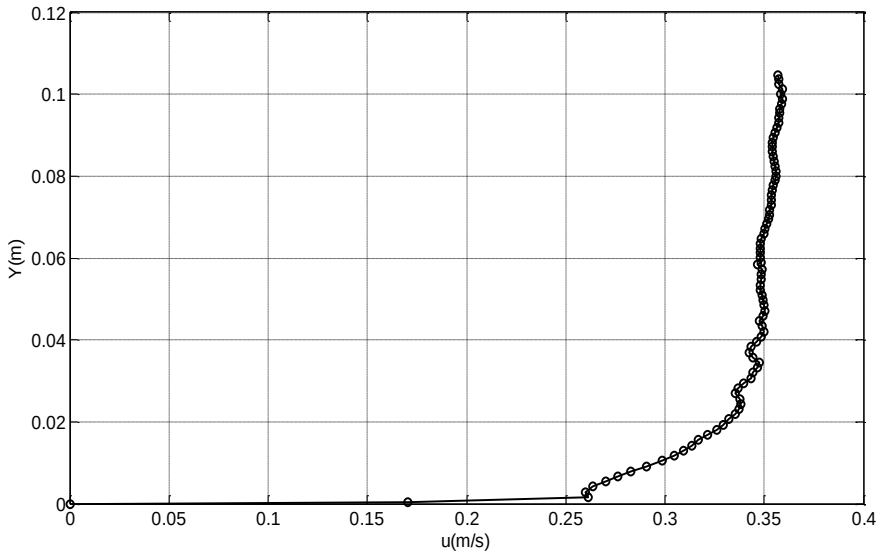

Figure 2.9 Measured horizontal velocity profile of the inflow (18.5cm from the center of cylinder), in the absence of cylinder

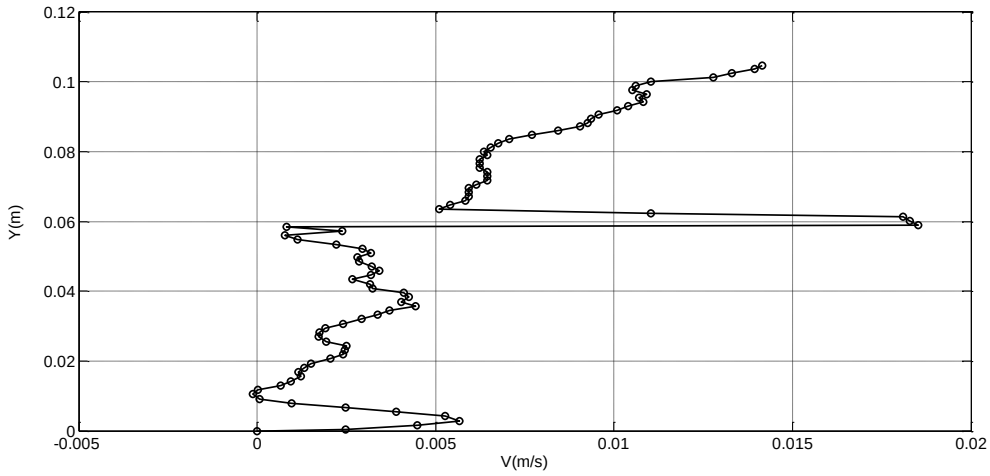

Figure 2.10 Measured vertical velocity profile of the inflow, in the absence of cylinder

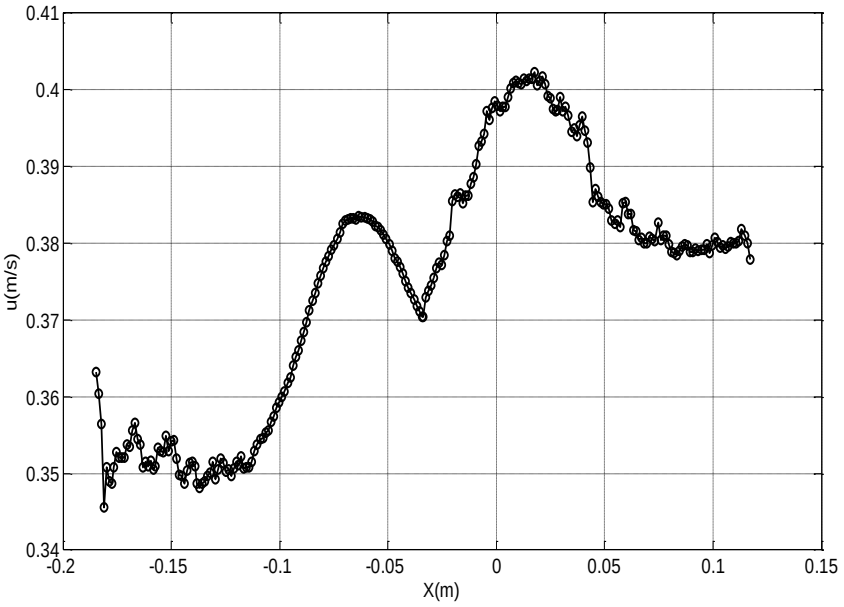

Figure 2.11 Measured horizontal velocity profile of the top side (4.5cm from the center of cylinder), in the presence of cylinder

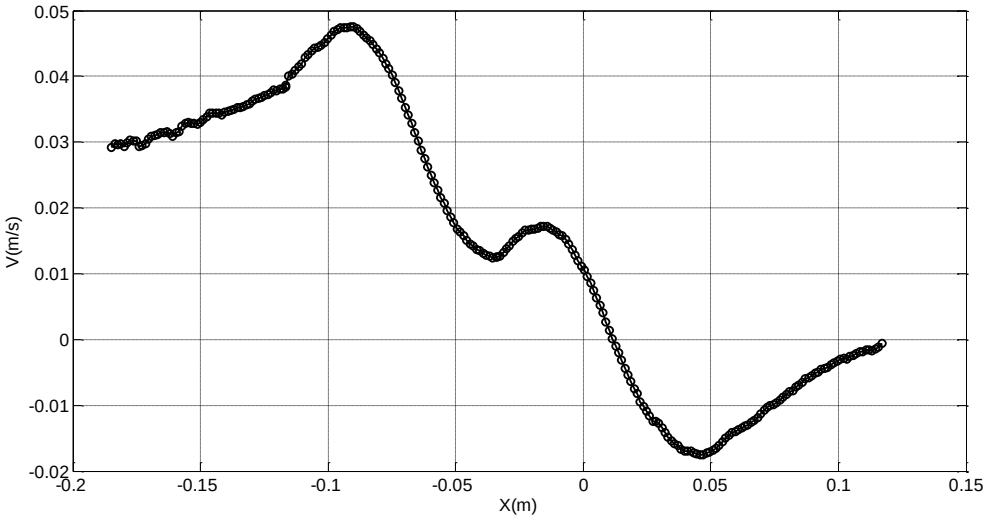

Figure 2.12 Measured vertical velocity profile of the top side, in the presence of cylinder

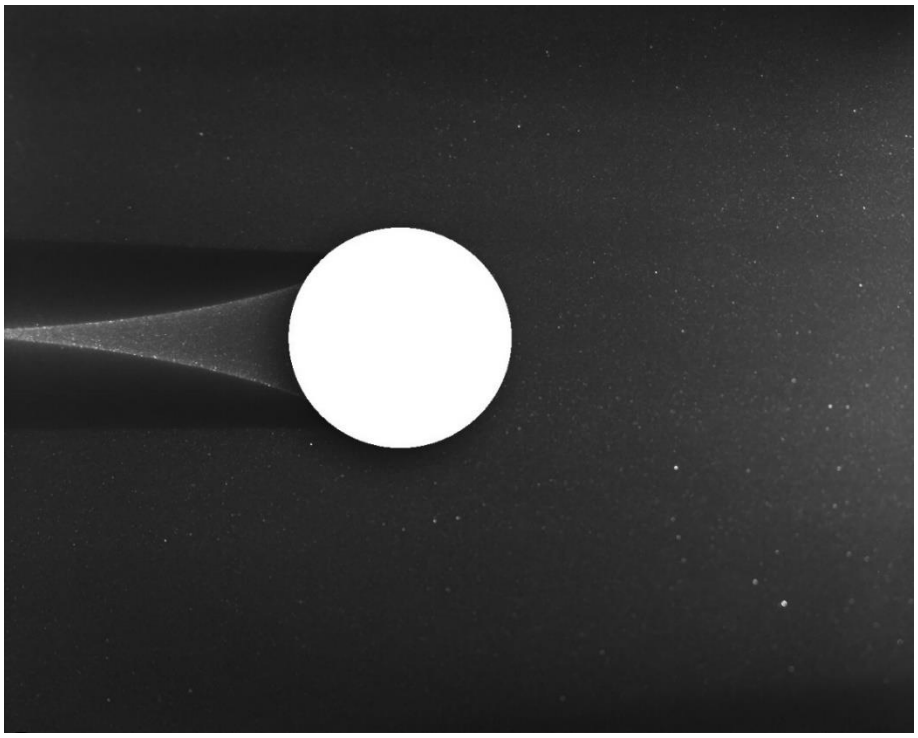

Figure 2.13 Masked cylinder

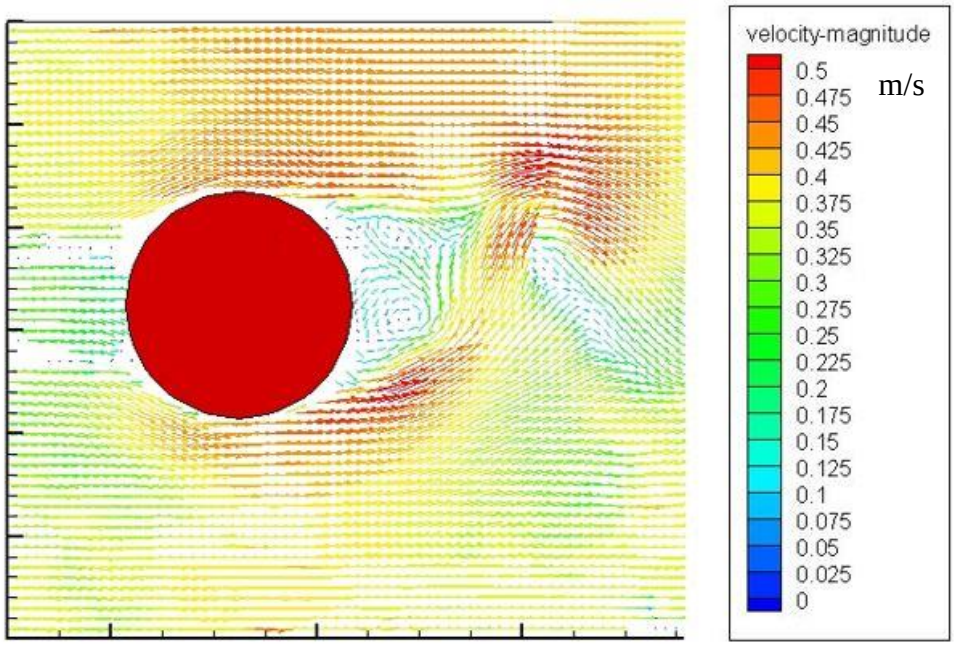

Figure 2.14 A snapshot of the measured flow field around the cylinder

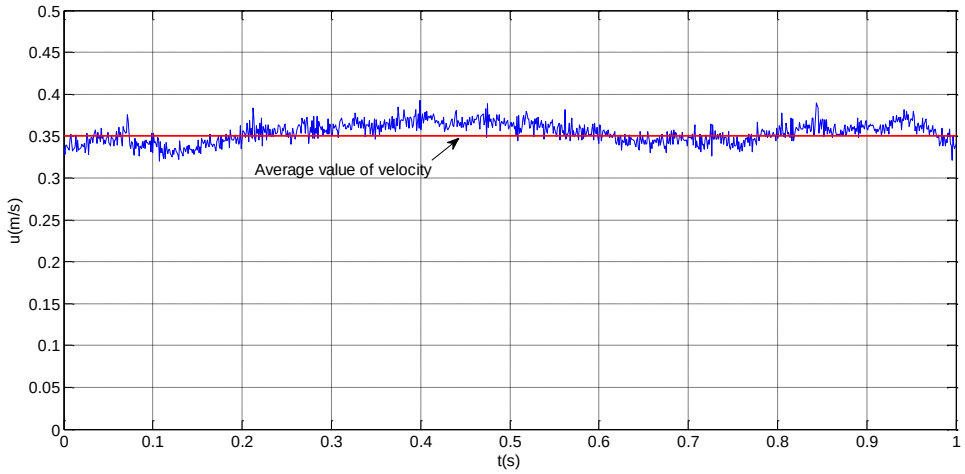

Figure 2.15 Time history of horizontal velocity at the selected point of the inflow

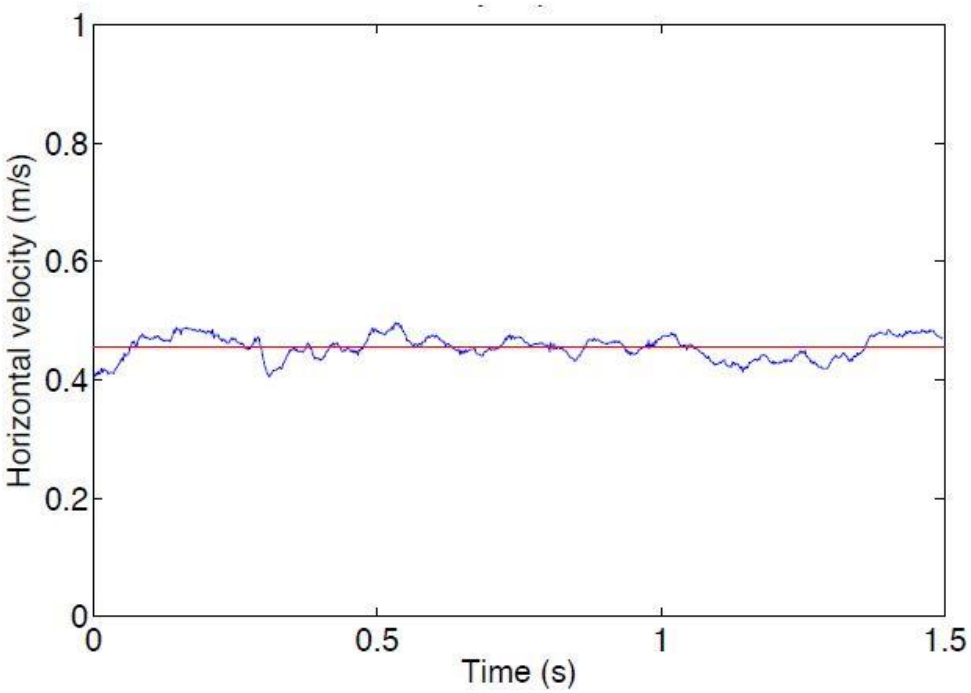

Figure 2.16 Time history of velocity from Stetson (2013)

Chapter 3 Computational Fluid Dynamics

3.1 Mesh

Two meshes (2D and 3D) replicating the dimensions of the measured region are created in ANSYS ICEM CFD meshing software. The 2D mesh (Figure 3.1) consists of 45,000 cells. The length and height of the domain are exactly the same as those of the measured region in the PIV experiment. The diameter of the cylinder is 0.018m. Figure 3.2 and Figure 3.3 show closeups of the same mesh near cylinder. It is 0.06m from the bottom to the center of cylinder and 0.045m from the center of cylinder to the top side. It is 0.185m from the inlet to the center of cylinder and 0.12m from the center of cylinder to the outlet.

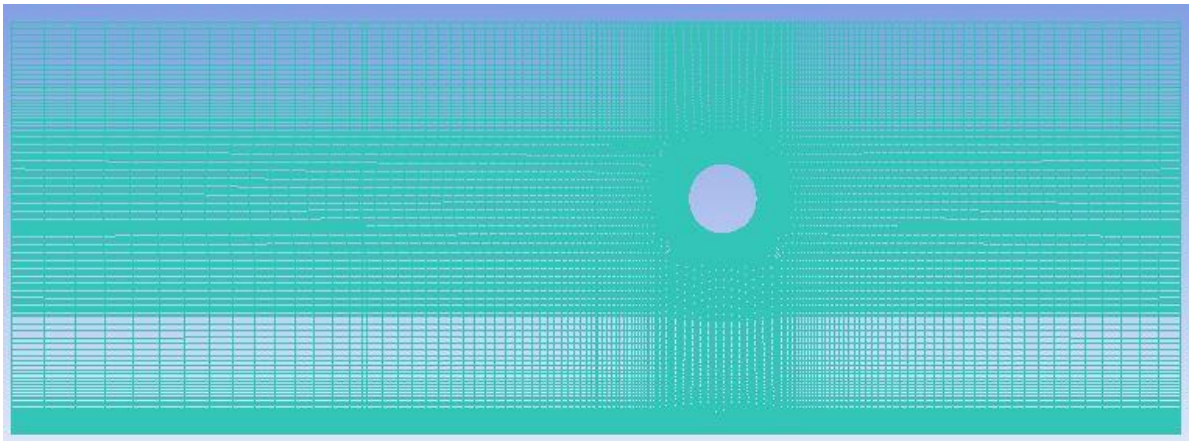

Figure 3.1 2D mesh replicating the measured region

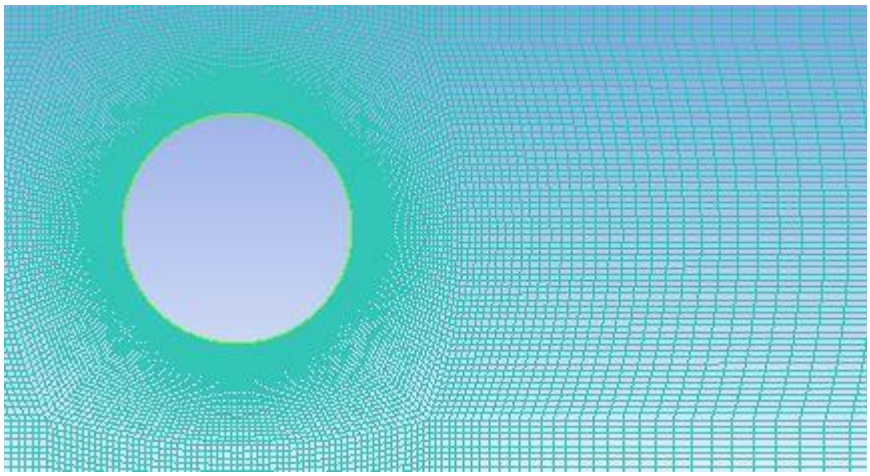

Figure 3.2 Closeup of mesh in the vicinity of cylinder

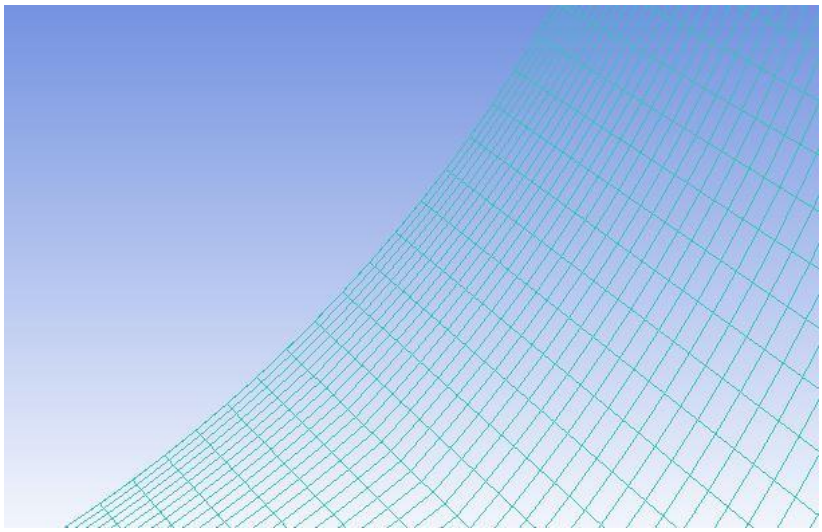

Figure 3.3 Closeup of mesh on the surface of cylinder

There are 30 layers in the spanwise direction for the 3D mesh (Figure 3.4 and Figure 3.5). At each layer, it is exactly the same as the 2D mesh. The total number of cells is 1,350,000. The spacing in the spanwise direction is constant (0.01m). So the width of the 3D mesh in the spanwise direction is the same as the width of the flume (0.3m). Since the space is constant in the spanwise direction, we do not consider the effects of the boundary

layers on the two vertical walls. In the CFD simulation, the two vertical walls are treated as symmetry.

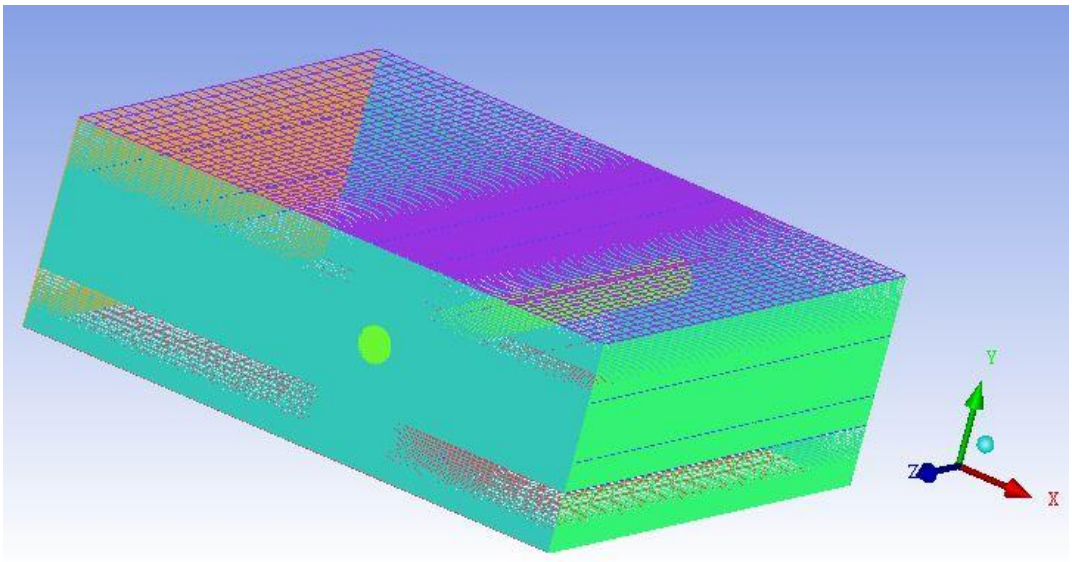

Figure 3.4 3D mesh replicating the measured region

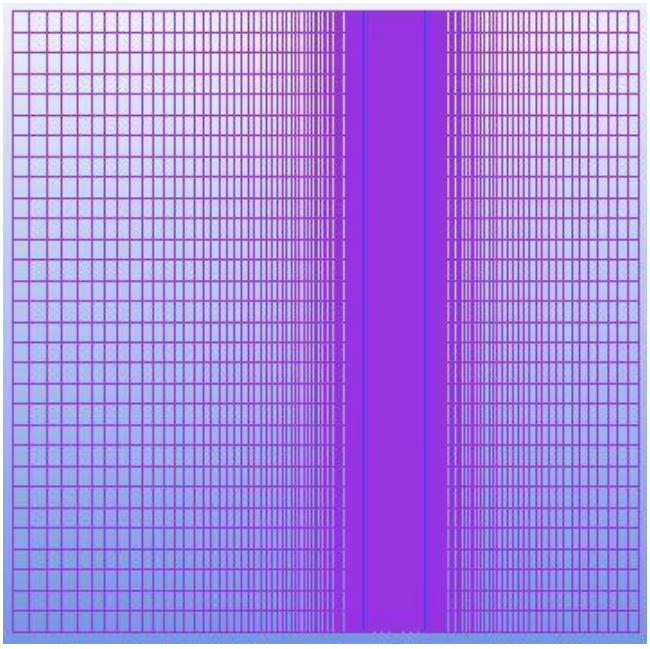

Figure 3.5 Top view of 3D mesh

3.2 Simulation approaches

In this study, two simulation approaches are adopted, Reynolds-averaged Navier–Stokes (RANS) and Large Eddy Simulation (LES).

3.2.1 RANS

RANS equations are the time-averaged equations of motion of fluid flow. The idea behind the equation is Reynolds decomposition, whereby an instantaneous quantity is decomposed into its time-averaged and fluctuating quantities(Eswaran and Biswas 2002). They govern the transport of the averaged flow quantities, with the complete range of the turbulent scales being modeled. So the advantage of RANS is that it can reduce the required computational time and efforts. There are two popular models of RANS, $k-\varepsilon$ and $k-\omega$. In this study, the $k-\omega$ model is adopted. In ANSYS Fluent, the specification method for turbulence is intensity and length scale. The turbulence intensity is 2%, which is from the PIV experiment. The length scale is about 0.086m, which is estimated based on the product of the free stream velocity and period. To decide which mesh, 2D or 3D, should be used in RANS, a simple 3D case with uniform inflow is run and results are compared at different planes in the spanwise direction (Figure 3.6). It is shown that results from different planes are exactly the same. So, the spanwise direction does not affect final results and the 2D mesh should be enough for the RANS case. Thus, 2D mesh is adopted in the RANS case. The RANS cases are unsteady and thus are URANS, however, since all RANS cases are URANS, we will use the terms interchangeably in this work.

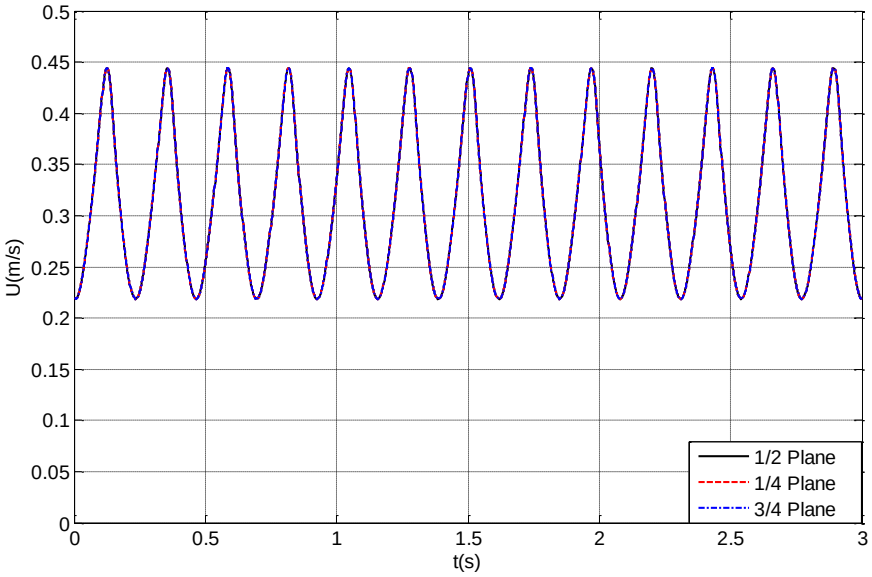

Figure 3.6 Results of RANS at three different planes in the spanwise direction

3.2.2 **LES**

The principal operation of LES is low-pass filtering (Asyikin 2012). By applying low-pass filtering, the small scales of the transport equation solution are eliminated. This reduces the computation cost of the simulation. The governing equations are transformed and solution is a filtered velocity field. . In LES the subgrid-scale model is Smagorinsky-Lilly. The fluctuating velocity algorithm is vortex method and the number of vortices was 190. The specification method for turbulence is intensity and length scale. The turbulence intensity is 2%, which is from the PIV experiment. The length scale is 0.086m. In LES, 3D mesh is required, which means that 2D mesh cannot be adopted in LES. In LES, the velocities at different planes in the spanwise direction are also checked (Figure 3.7). It is

shown that the behaviors of velocities at different planes are similar, but there are still significant differences among different planes.

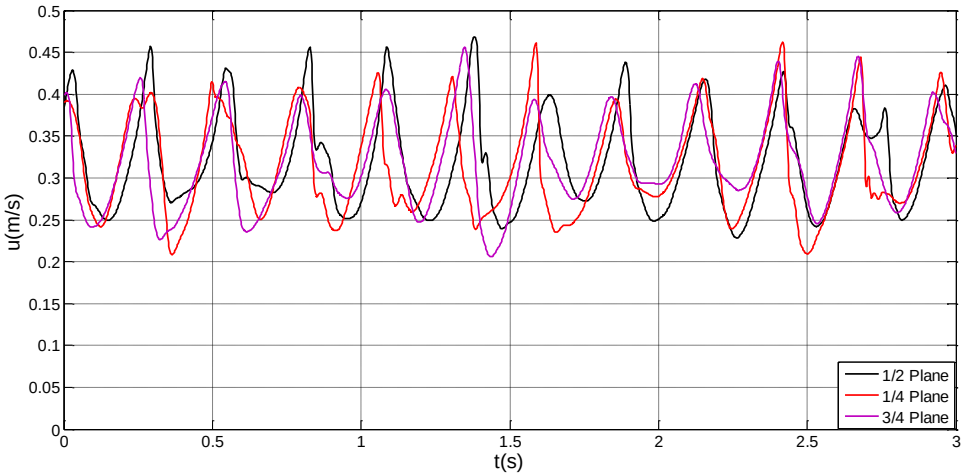

Figure 3.7 Results of LES at three different planes in the spanwise direction

3.3 Boundary conditions

3.3.1 Boundary conditions for 2D case

In the 2D case, the boundary conditions for the inflow and top side are velocity inlet, including velocity profiles and turbulence intensity from PIV experiment. To verify that the mean velocity profiles are appropriate, the time history of velocity at the specific top point, which is 0.045m downstream of the cylinder, is checked (Figure 3.8). It is shown that that standard deviation is 0.0164m/s, which is about 4% of the mean velocity. So the time variation of the boundary is not significant, indicating the mean velocity profiles are adequate for this problem. The bottom of flume and surface of cylinder are no-slip walls. It is pressure outlet for the right side. All the boundary conditions are shown in Figure 3.9.

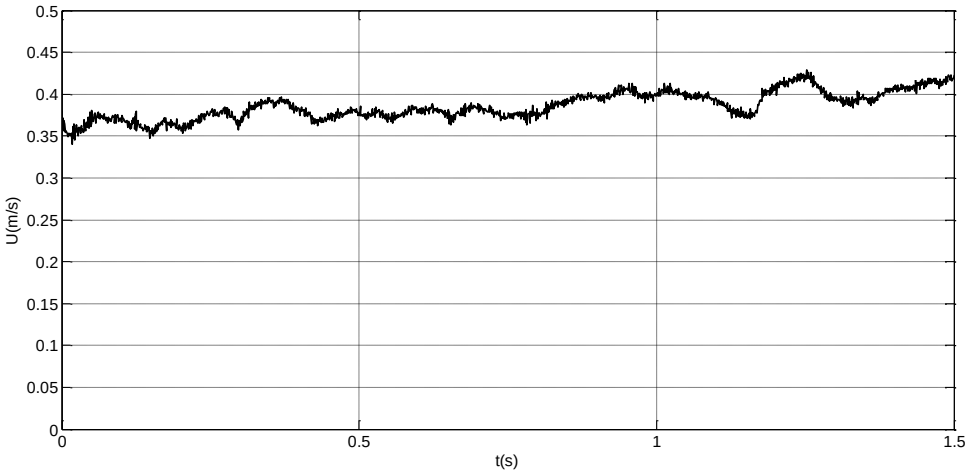

Figure 3.8 Time history of the measured horizontal velocity of the point plus1 (in Figure 3.16)

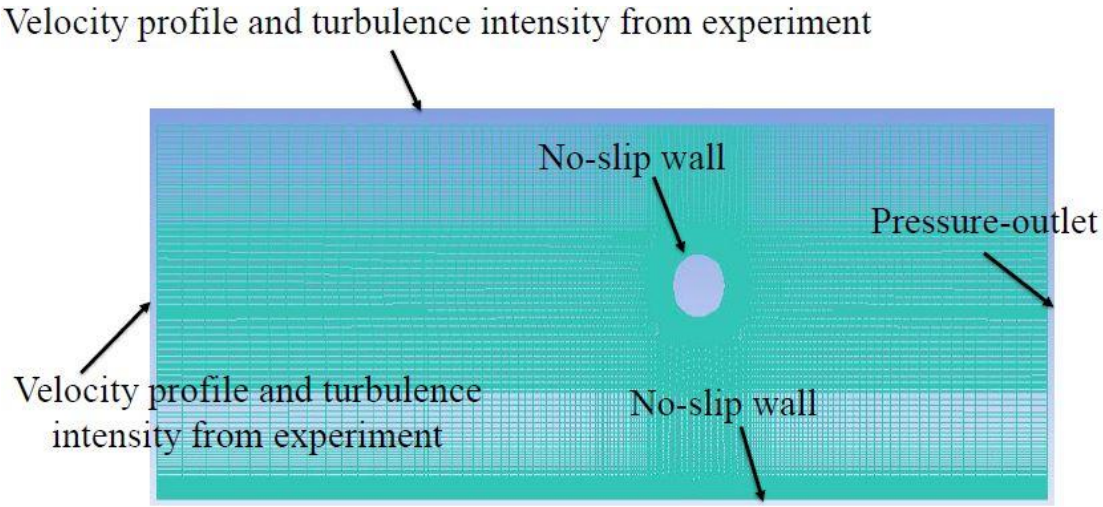

Figure 3.9 Boundary conditions for 2D case

3.3.2 Boundary conditions for 3D case

The boundary conditions in 3D case are the same at different layers in the spanwise direction and identical to those in the 2D case. Since we do not consider the effects of the boundary layers on the two vertical walls, two vertical walls are set as symmetry (Figure 3.10).

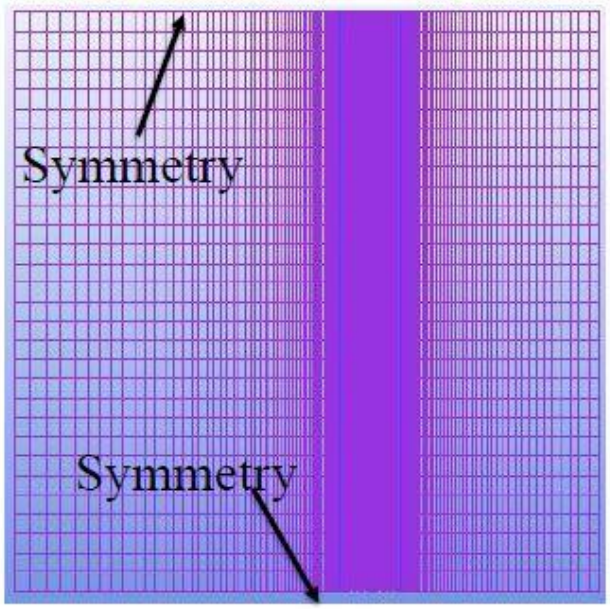

Figure 3.10 Boundary conditions for 3D case

3.4 Details of cases

2D mesh is adopted for RANS and 3D mesh is adopted for LES. In PIV experiment, the total measured time is 3 seconds. In CFD, it will take some time for the vortex shedding to occur and the flow to reach a relatively steady state. Thus the simulated time in CFD is 12 seconds. The data of the last three seconds are used. To verify that at t=9s, the flow has

reached a relatively steady state, the horizontal velocity is checked at point 10 for both RANS and LES cases from t=6s to t=12s (Figure 3.11 and Figure 3.12). It is shown that in both cases, the flow has reached a relatively steady state at t=9s. From Figure 3.13, the Strouhal number can be decided to be 0.21 based on Re=6,300. The expression for Strouhal number is $St = \frac{fD}{U}$, where f is the frequency of vortex shedding, D is the diameter of cylinder and U is the free-stream velocity. The frequency of vortex shedding can be calculated from the expression for Strouhal number, 4.08 Hz. So the period is about 0.245 second. For the purpose of convergence and stability, the time step should be equal or smaller than 1 percent of period of vortex shedding. So, the time step is 0.002s, which is about 0.8 percent of the period. For all cases, the initial condition is the same as the inflow boundary condition.

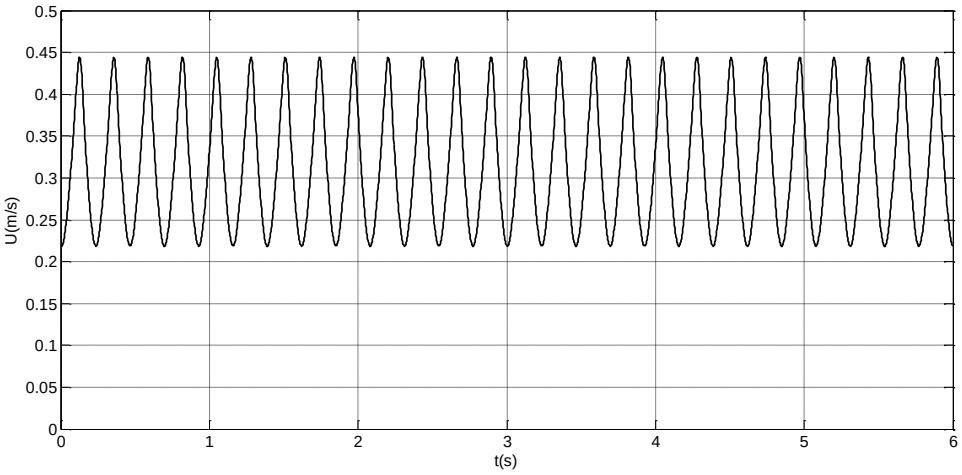

Figure 3.11 Horizontal velocity of point 10 (in Figure 3.16) from t=6s to t=12s in RANS

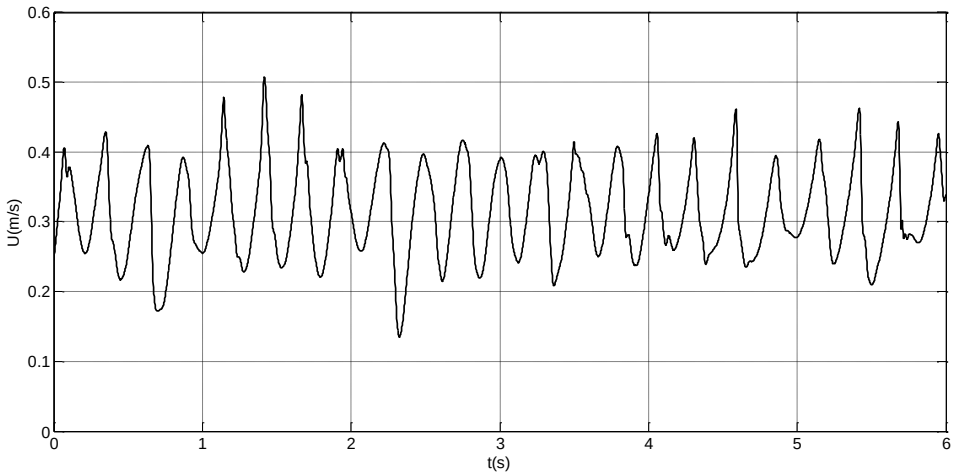

Figure 3.12 Horizontal velocity of point 10 (in Figure 3.16) from t=6s to t=12s in LES

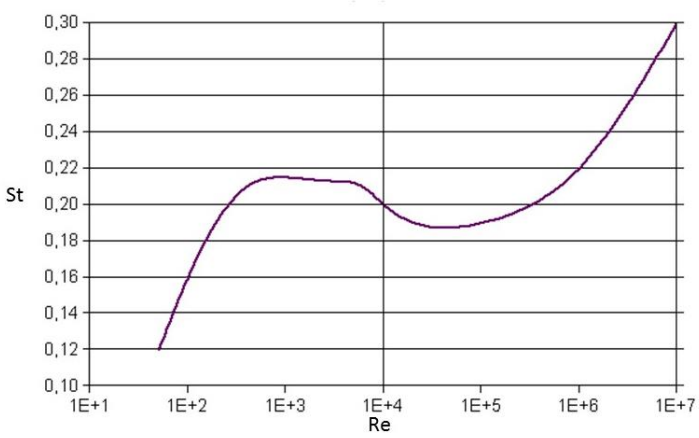

Figure 3.13 Relationship between Re and Strouhal number (Williamson 1988)

The RANS case is run on two nodes of the Computational Hydrodynamics Laboratory, using 16 Intel Core Duo 2.5GHz CPUs. It takes about 6 hours. The LES case is run with 4 nodes, using 32 Intel Core Duo 2.5GHz CPUs and it takes about 55 hours. All of the details are shown in Table 3.1. The Y-Plus values around cylinder are shown in Figure 3.14 and Figure 3.15 for both cases. In both cases, Y-Plus values are smaller than 1.50. Time histories of horizontal velocities of specific points (Figure 3.16) around the

cylinder are extracted from both cases using a surface monitor in Fluent. Drag and Lift coefficients are extracted using force monitor. Profiles of horizontal and vertical velocities along three different sections (Figure 3.17) are recorded every time step using automatic export, as well as the velocity fields in both 2D case (Figure 3.18) and 3D case (Figure 3.19).

Table 3-1 Details of CFD cases

Turbulence models	RANS(k-ω)	LES
Mesh Information	45,000 cells(2D)	1,350,000 cells(3D)
Simulated time	12s	12s
Time step	0.002s	0.002s
Total time for calculation	6 hours (16 CPUs)	55 hours (32 CPUs)

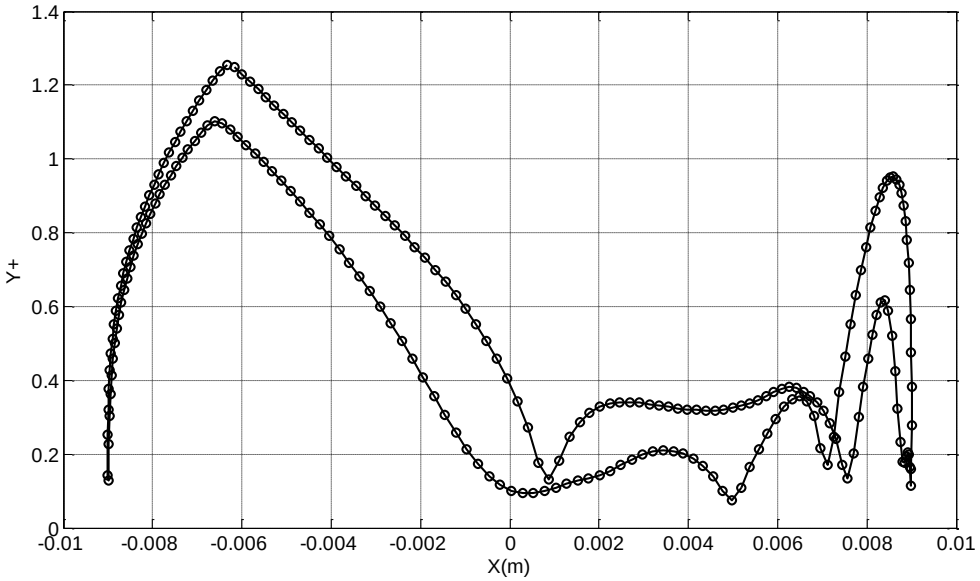

Figure 3.14 Y-Plus around the cylinder in RANS

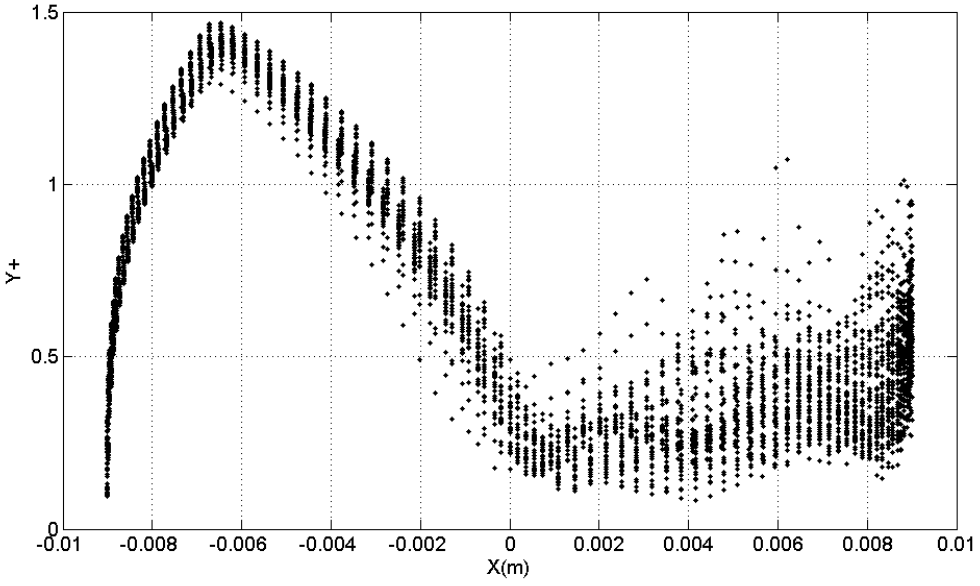

Figure 3.15 Y-Plus around cylinder in LES

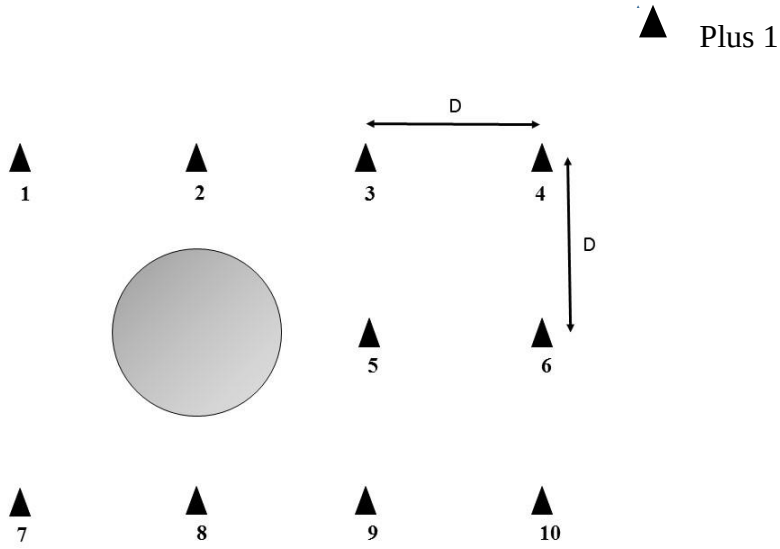

Figure 3.16 Location of points around cylinder

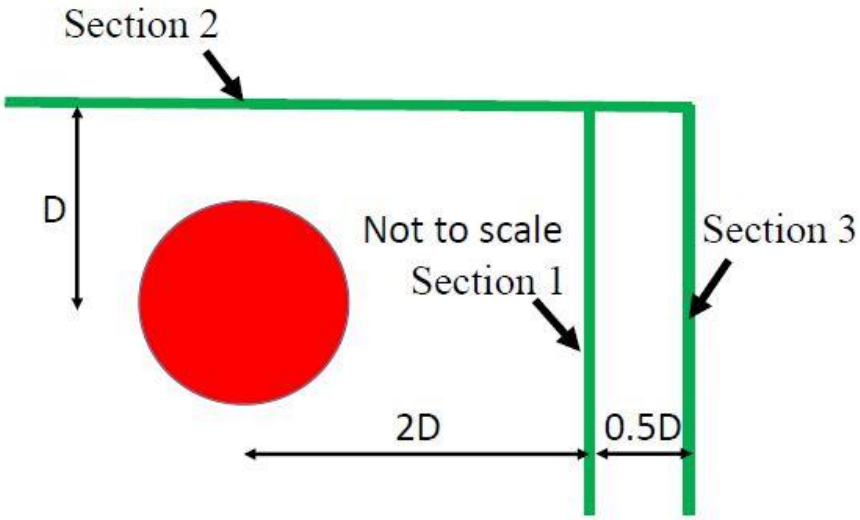

Figure 3.17 Velocity profile recording sections

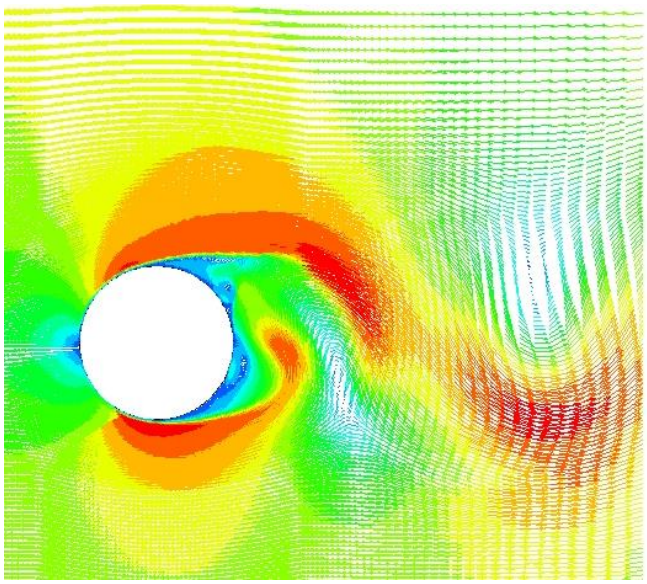

Figure 3.18 Snapshot of flow velocity field in RANS (t=3s)

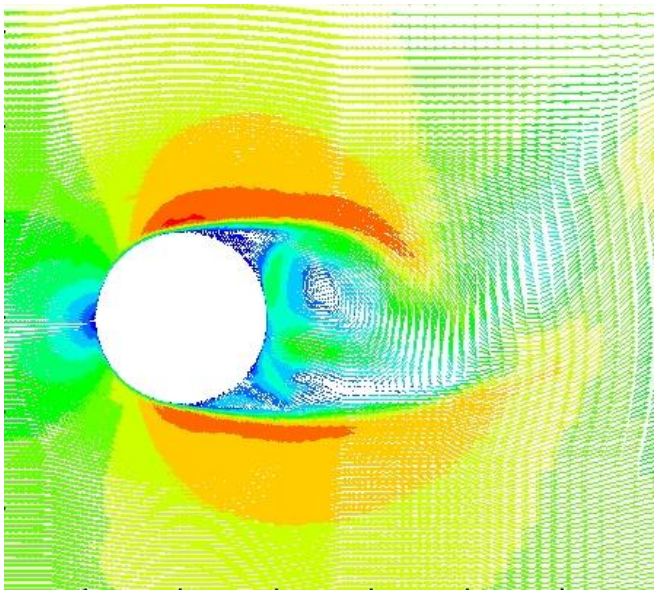

Figure 3.19 Snapshot of flow velocity field in LES (t=3s)

Chapter 4 Comparison of PIV and CFD flows

4.1 Velocity vector fields

Before comparing the flow characteristics at specific locations, we concentrate on the general trends of the velocity vector fields. While this task is more easily accomplished by showing videos from both PIV experiments and CFD simulations, the snapshots of velocity vector fields from both PIV experiment and CFD simulations can provide a general understanding of the vortex patterns. Each snapshot shows velocity vector fields with the same color scale donating the vector magnitude. In each figure, RANS vectors are shown first, then LES vectors, and finally PIV vectors are shown. Velocity vector fields are compared at three different points (t=0.2s, t=0.3s and t=0.4s). The velocity vector fields are synchronized with the horizontal velocity of point 10 (Figure 3.16) downstream of the cylinder.

The vortexes in RANS simulation are more compact, while those in LES simulation and PIV experiments are more dispersed. The result in RANS shows a smaller region of low velocities in the wake as compared to those in LES and PIV experiment. The shedding patterns in three methods are very similar to each other.

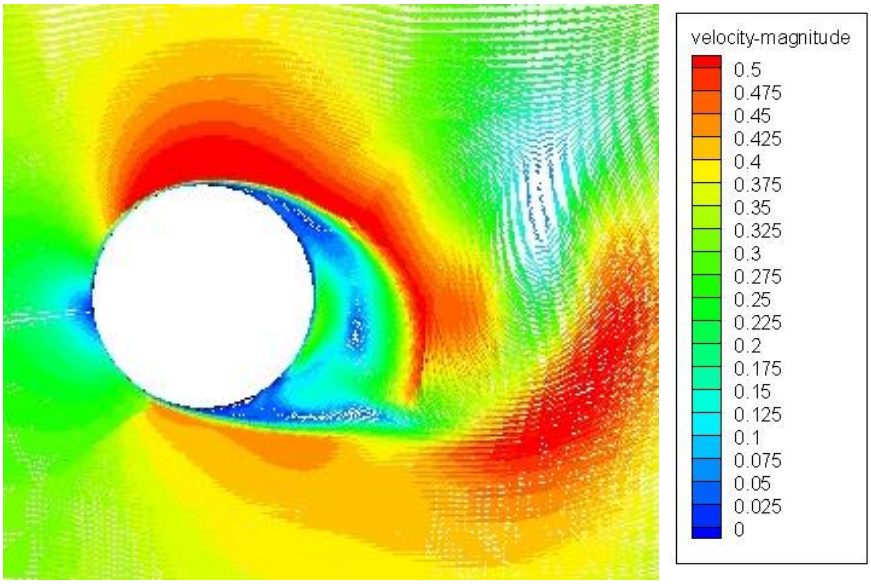

(a) Velocity vector field in RANS (t=0.2s)

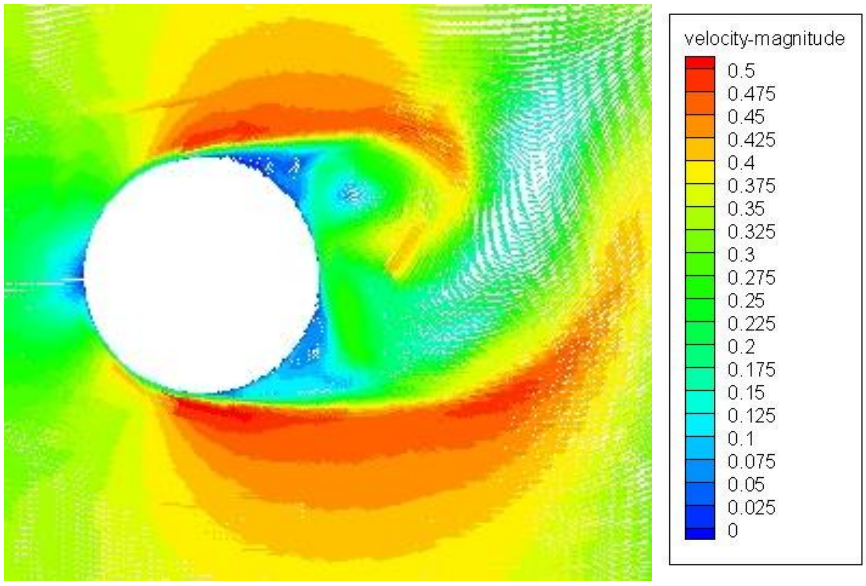

(b) Velocity vector field in LES (t=0.2s)

Figure 4.1 Velocity vector fields in RANS, LES and PIV (t=0.2s)

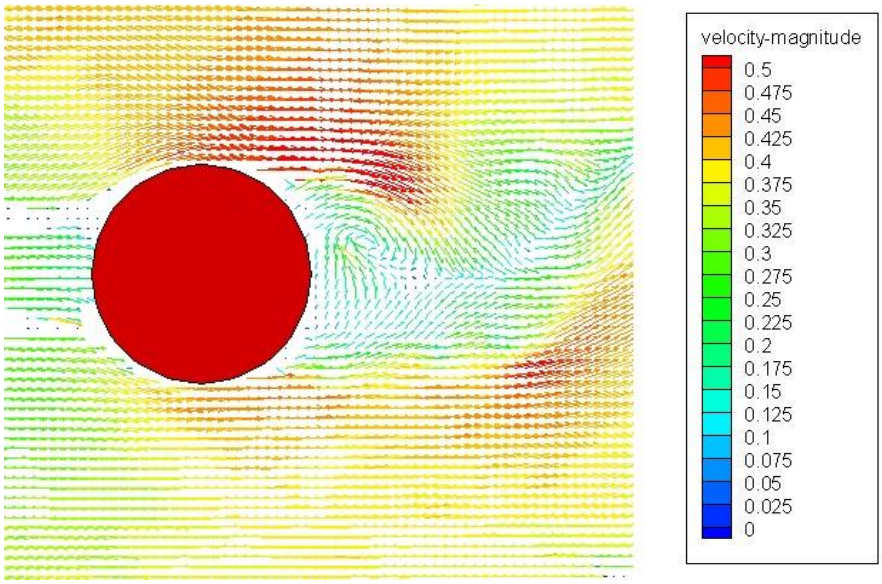

(c) Velocity vector field in PIV (t=0.2s)

Figure 4.1 Velocity vector fields in RANS, LES and PIV (t=0.2s)

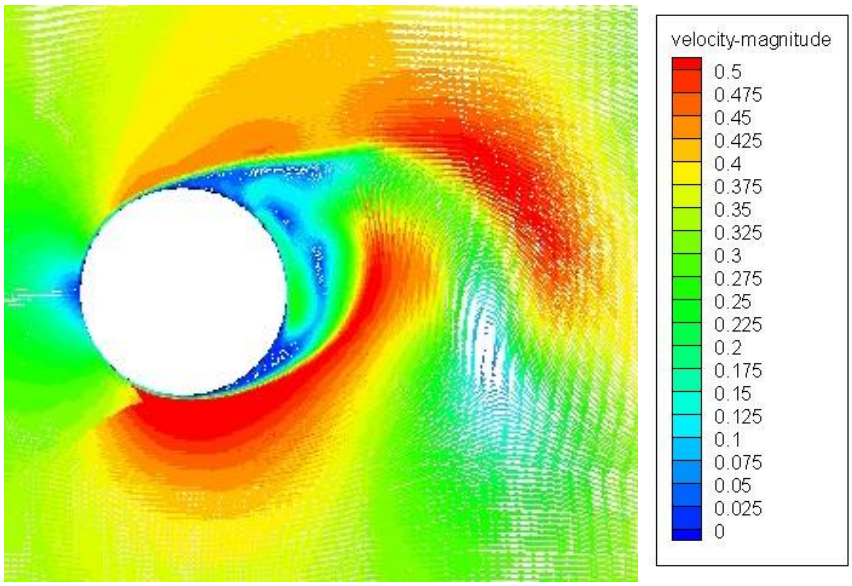

(a) Velocity vector field in RANS (t=0.3s)

Figure 4.2 Velocity vector fields in RANS, LES and PIV (t=0.3s)

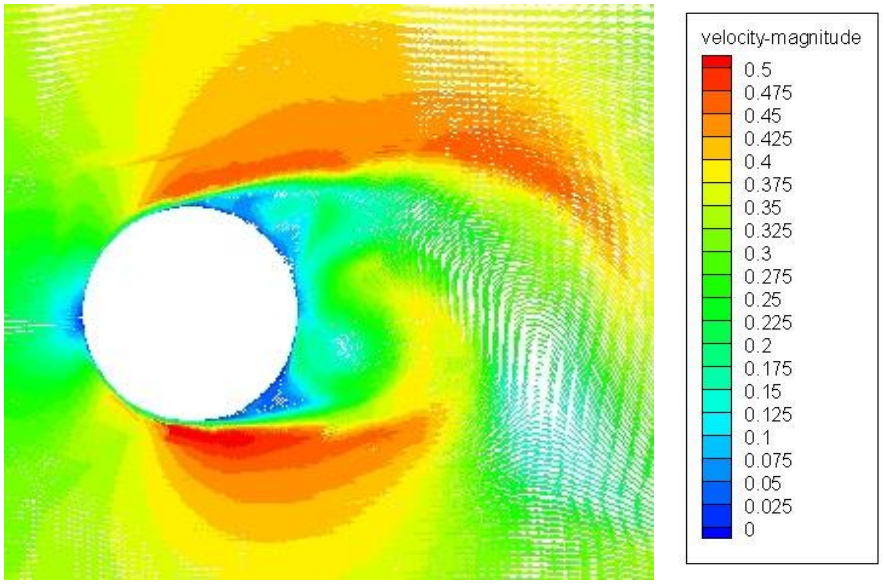

(b) Velocity vector field in LES (t=0.3s)

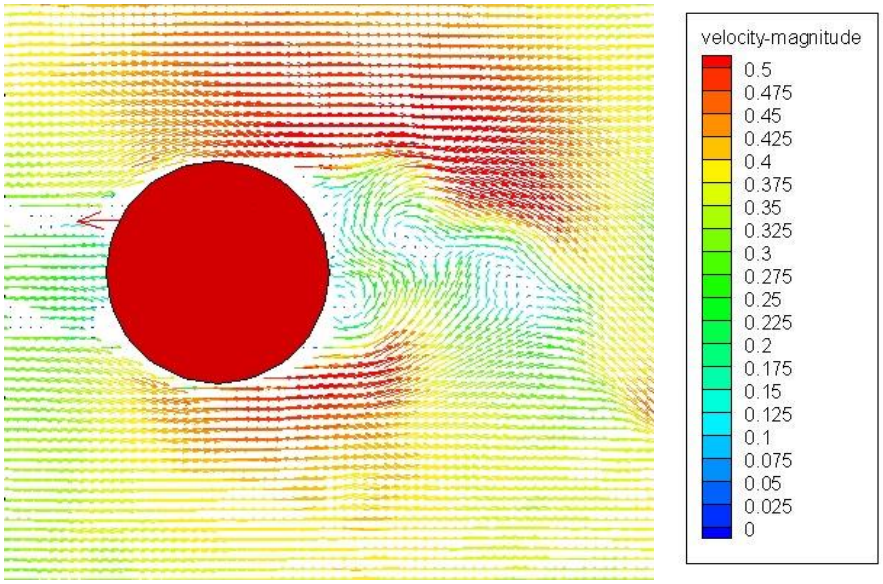

(c) Velocity vector field in PIV (t=0.3s)

Figure 4.2 Velocity vector fields in RANS, LES and PIV (t=0.3s)

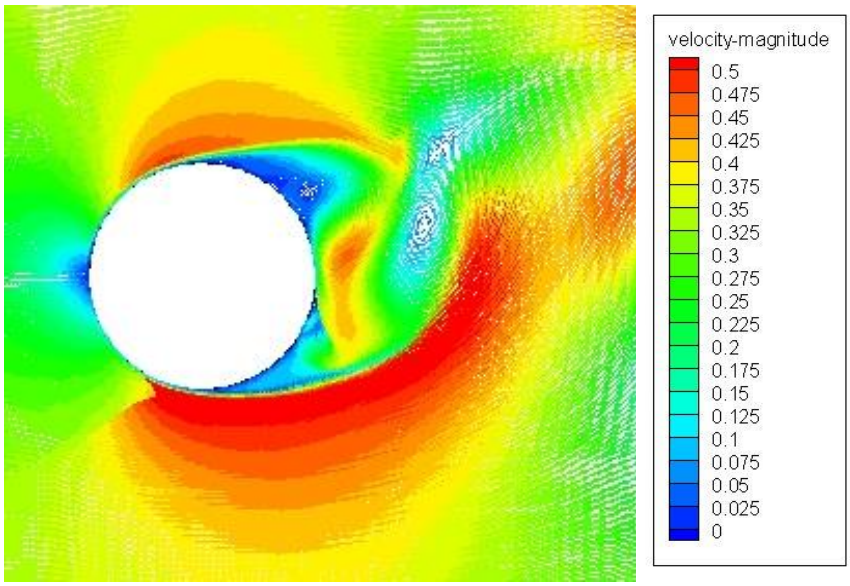

(a) Velocity vector field in RANS (t=0.4s)

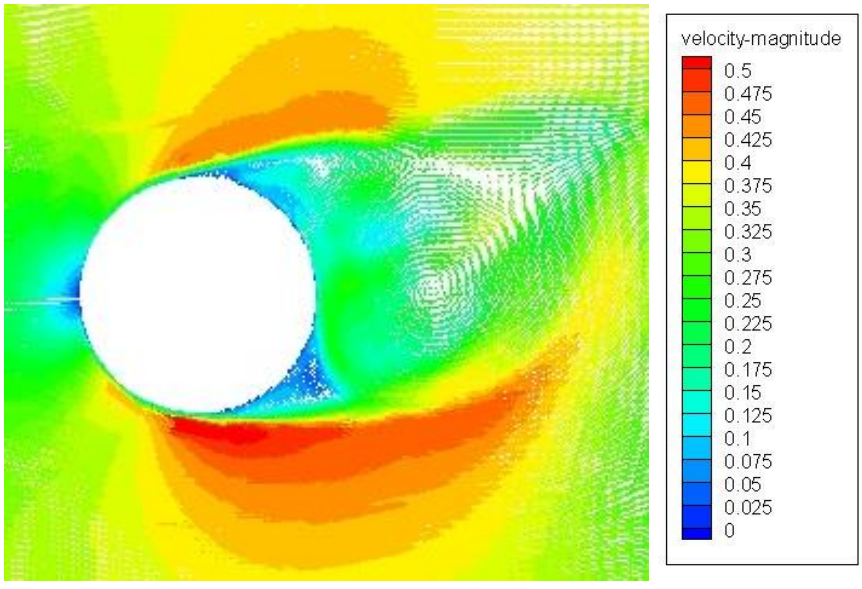

(b) Velocity vector fields in LES (t=0.4s)

Figure 4.3 Velocity vector fields in RANS, LES and PIV (t=0.4s)

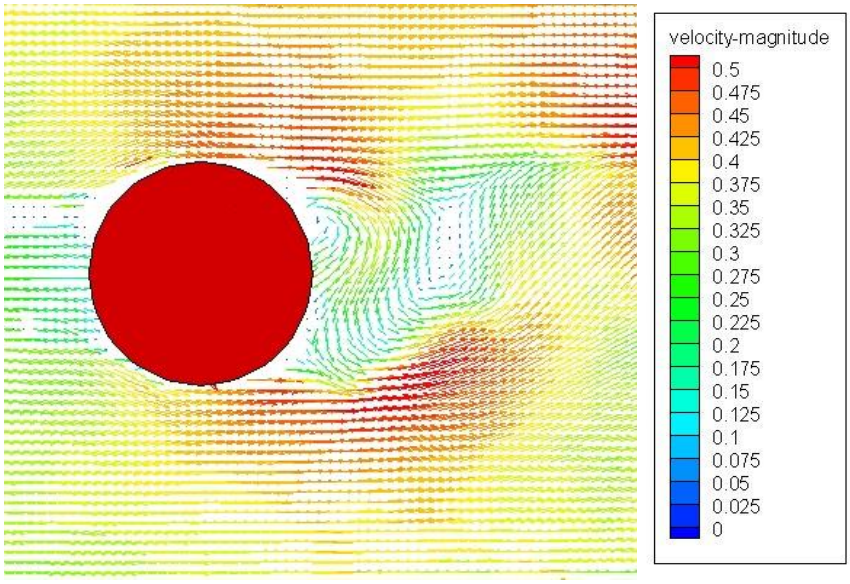

(c) Velocity vector field in PIV (t=0.4s)

Figure 4.3 Velocity vector fields in RANS, LES and PIV (t=0.4s)

4.2 Time history of velocity

The time histories of horizontal velocities are compared at specific points (Figure 4.4) around the cylinder. In each figure, the location of the velocity tracking point is noted on the right hand side with a red triangular and on the left hand side we see the PIV-CFD comparison. As expected, the periods of velocity, which are also the periods of vortex shedding, are very close to the Strouhal period (0.245s).

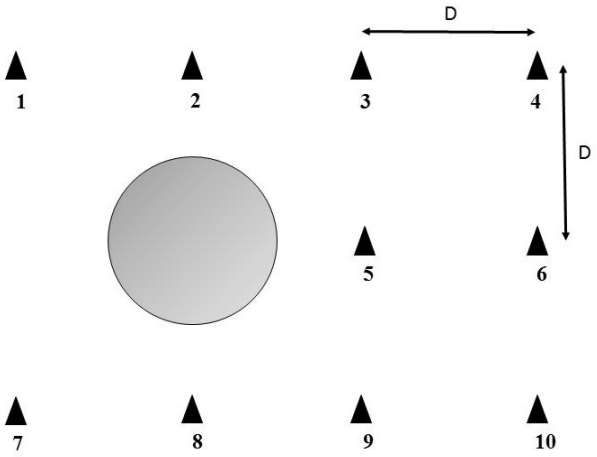

Figure 4.4 Specific points around cylinder to compare horizontal velocity

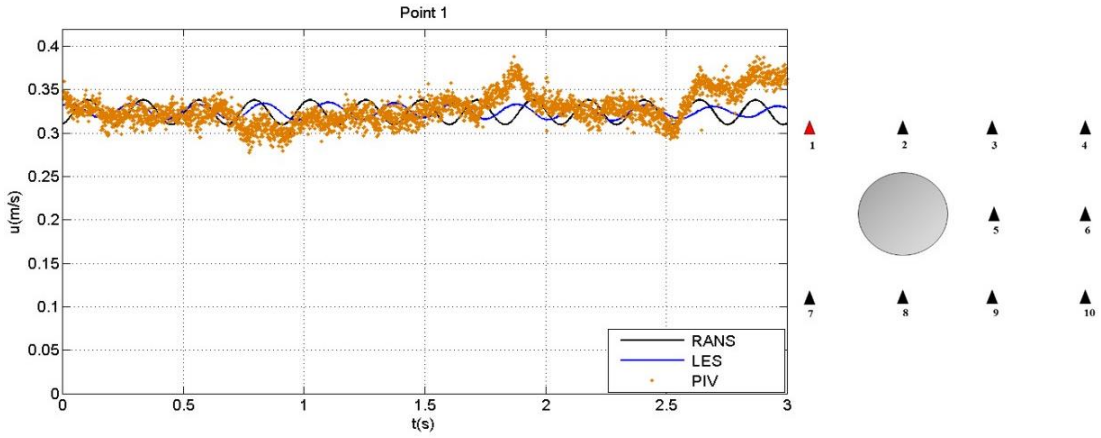

Figure 4.5 Time history of horizontal velocity of point 1

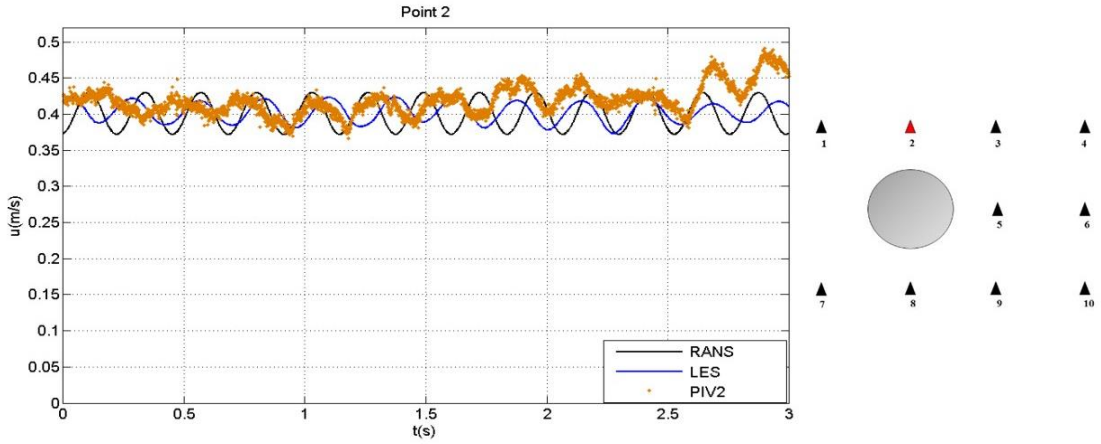

Figure 4.6 Time history of horizontal velocity of point 2

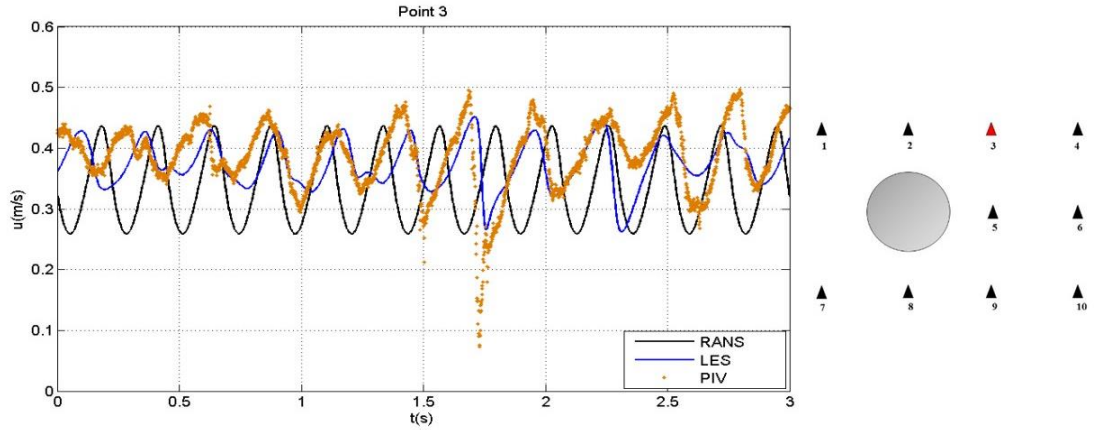

Figure 4.7 Time history of horizontal velocity of point 3

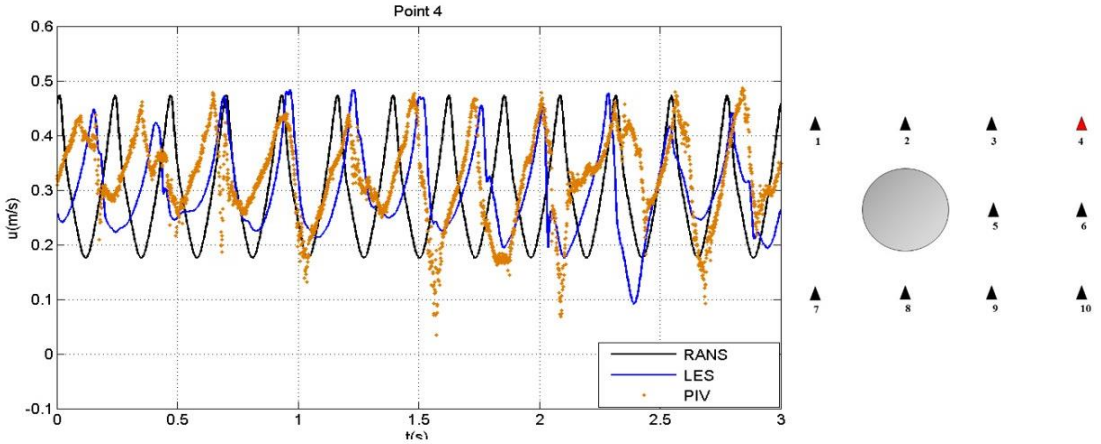

Figure 4.8 Time history of horizontal velocity of point 4

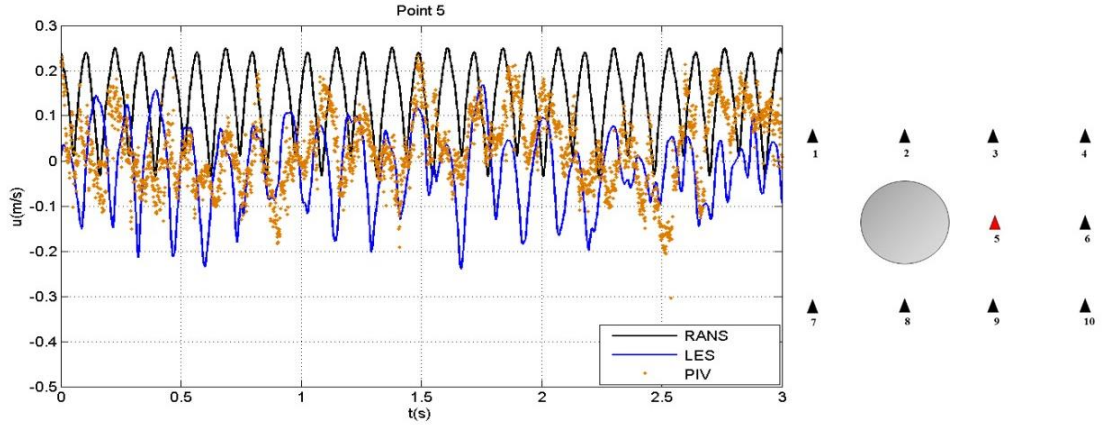

Figure 4.9 Time history of horizontal velocity of point 5

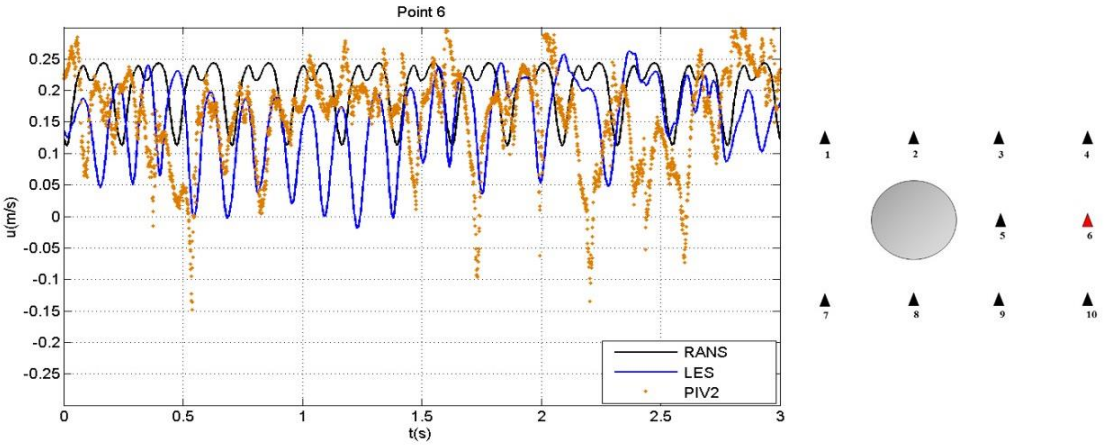

Figure 4.10 Time history of horizontal velocity of point 6

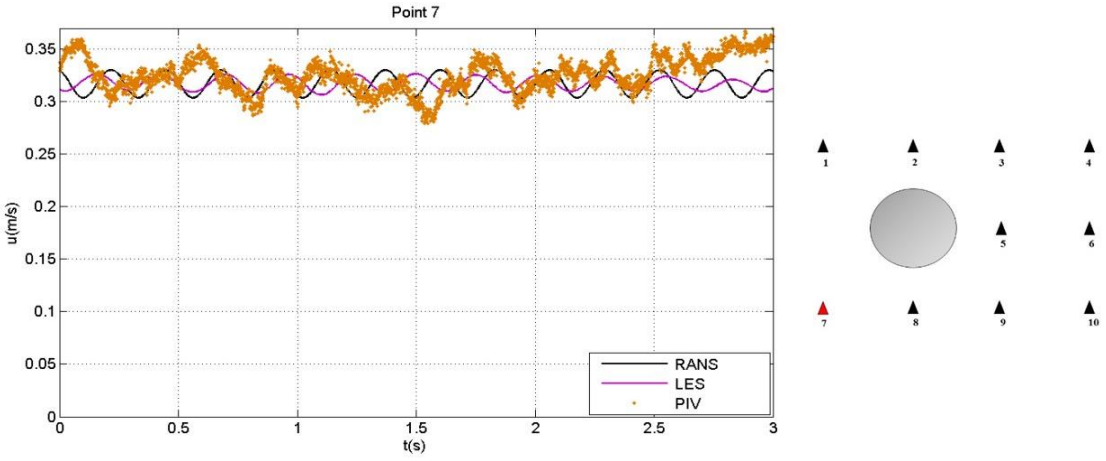

Figure 4.11 Time history of horizontal velocity of point 7

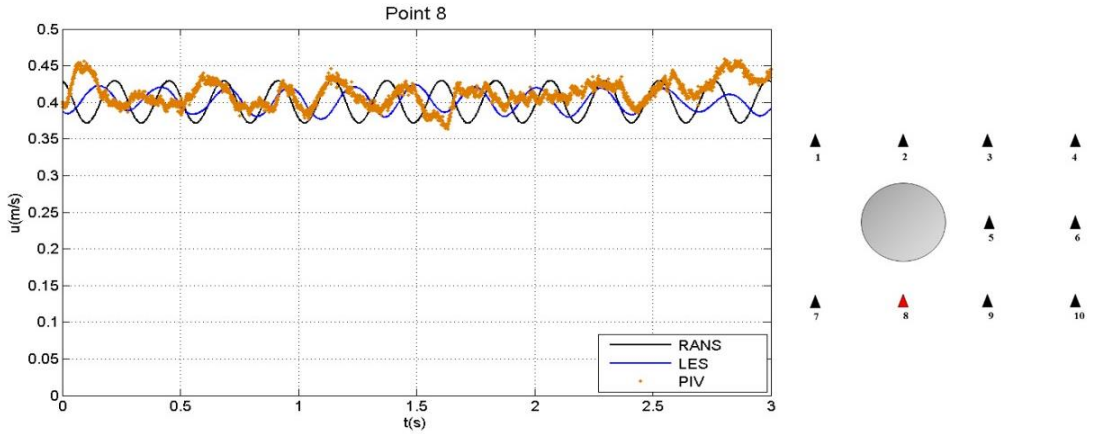

Figure 4.12 Time history of horizontal velocity of point 8

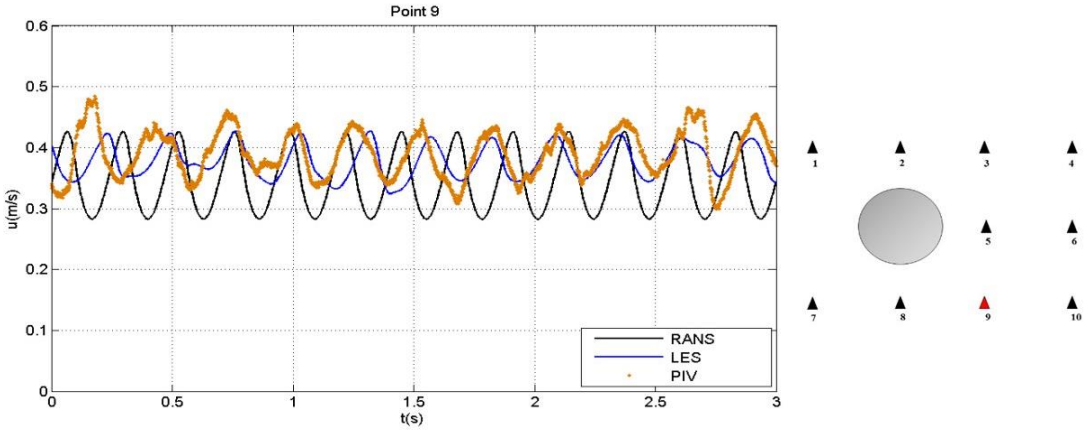

Figure 4.13 Time history of horizontal velocity of point 9

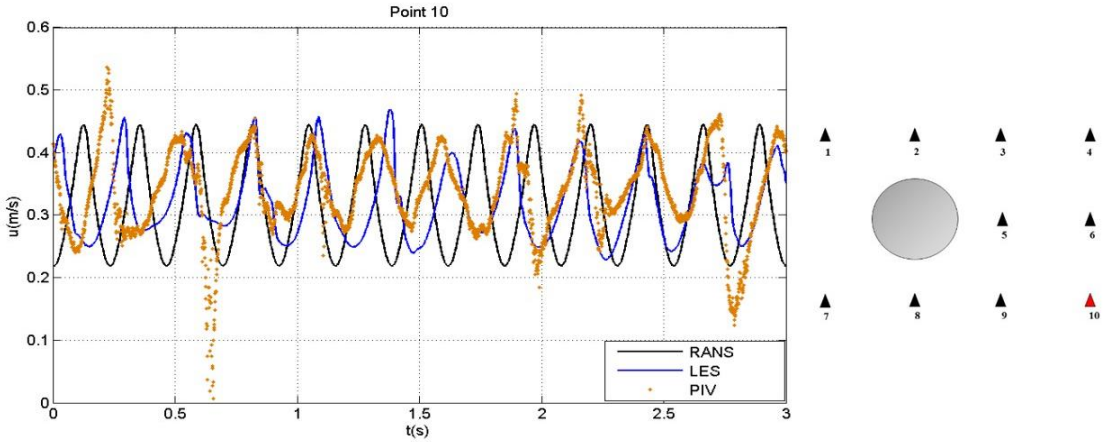

Figure 4.14 Time history of horizontal velocity of point 10

At point 1 and point 7 (Figure 4.5 and Figure 4.11), which are at the upstream of the cylinder, both RANS and LES can provide a good prediction of the velocity, concerning the mean values and amplitudes. At point 2 and point 8 (Figure 4.6 and Figure 4.12), which are at the same horizontal position as the center of cylinder, the mean values and amplitudes of velocity become larger. Both of them are still very similar to that of PIV. At point 3 and point 9 (Figure 4.7 and Figure 4.13), which are at the downstream of cylinder, the amplitudes of velocity keep increasing. The mean values and amplitudes of LES simulation and PIV experiment are much closer to each other, compared with those of RANS simulation. The mean values in LES and PIV are larger than that in RANS, while the amplitudes are smaller. As expected, the profile of velocity in RANS is very regular, which is similar to the shape of sinusoid. However, in LES and PIV, the velocity profiles tend to be irregular. At point 4 and point 10 (Fig 4.8 and Figure 4.14), the amplitudes become larger. LES tends to capture more characteristics of velocity measured in PIV experiment, compared with RANS. At point 5 and point 6 (Figure 4.9 and Figure 4.10), which are at the same vertical position as the center of cylinder, the periods of velocity from three methods all become half of those at other points. The reason is that the vortexes from both sides of cylinder, up and down, can reach the two points, however, at all other points, only the vortex from one side can reach. At the two points it is hard to the PIV system to have a good measurement due to the limited amount of particles in this region. However, the mean value in LES is still closer to that of the PIV, compared with RANS.

4.3 Time-averaged velocities and Reynolds stresses

The time-averaged velocities and Reynolds stresses are analyzed and compared at three different sections (Figure 4.15). The first section is at the downstream of the cylinder, 2 diameters (0.036m) away from the center of cylinder. The second section is above the cylinder, 1 diameter (0.018m) away from the center of cylinder. The third section is at the downstream of cylinder, 2.5 diameters (0.045m) away from the center of cylinder. Since the PIV experiment is two dimensional, only three Reynolds stresses are analyzed, including $\langle u'^2 \rangle$ $\langle v'^2 \rangle$ and $\langle u'v' \rangle$.

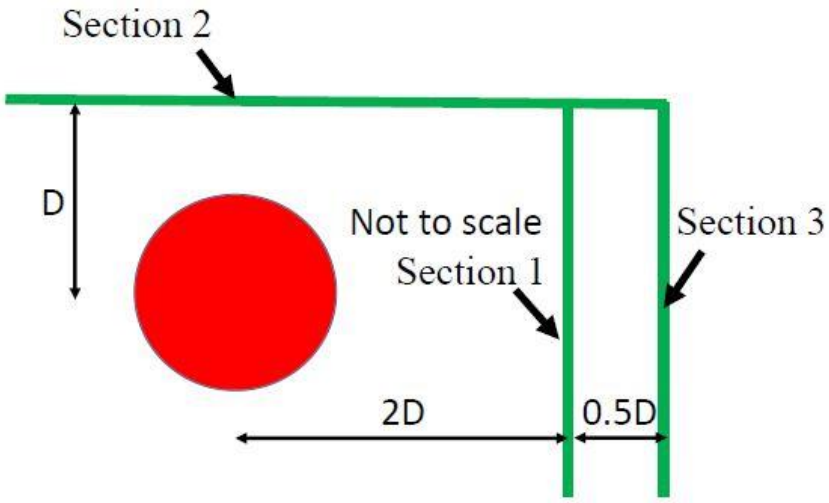

Figure 4.15 Time- averaged velocities and Reynolds stresses analyzed sections

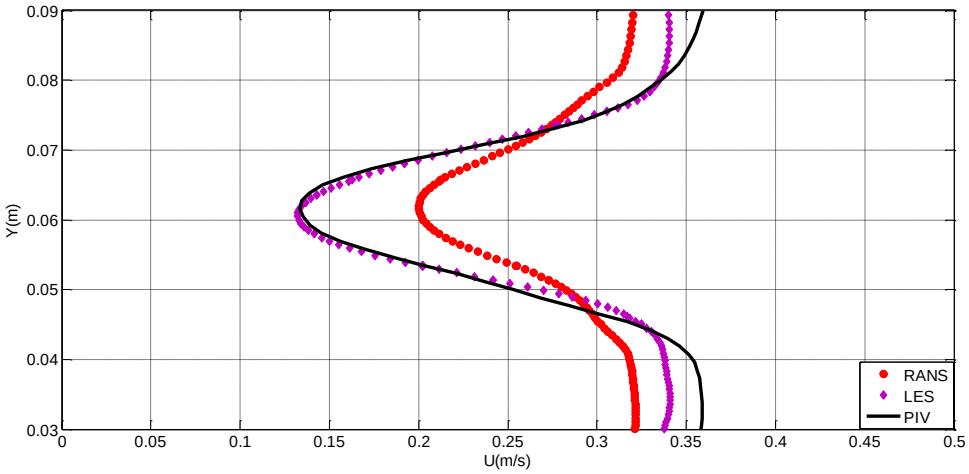

Figure 4.16 Time-averaged horizontal velocity at section 1

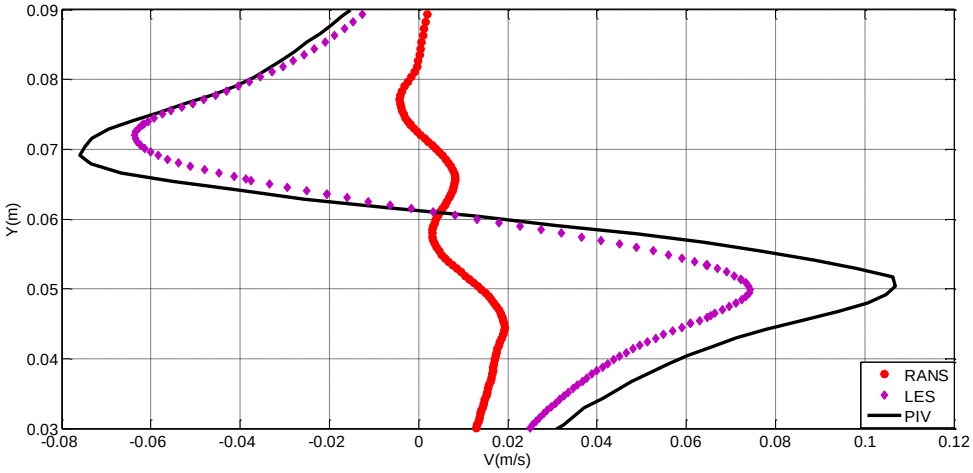

Figure 4.17 Time-averaged vertical velocity at section 1

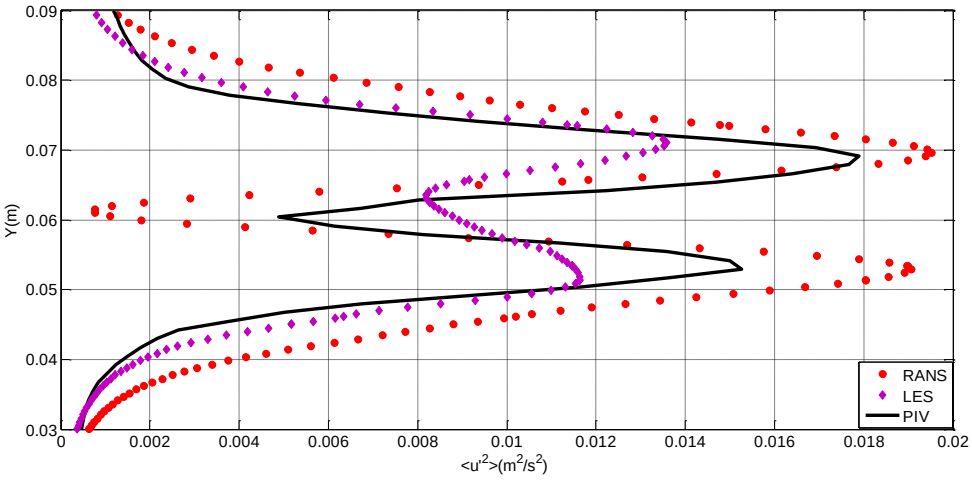

Figure 4.18 Profile of $\langle u'^2 \rangle$ at section 1

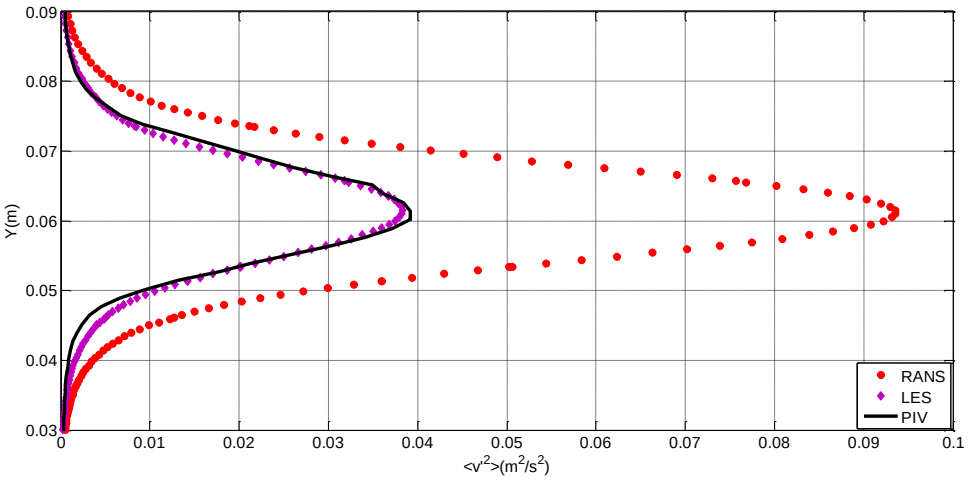

Figure 4.19 Profile of $\langle v'^2 \rangle$ at section 1

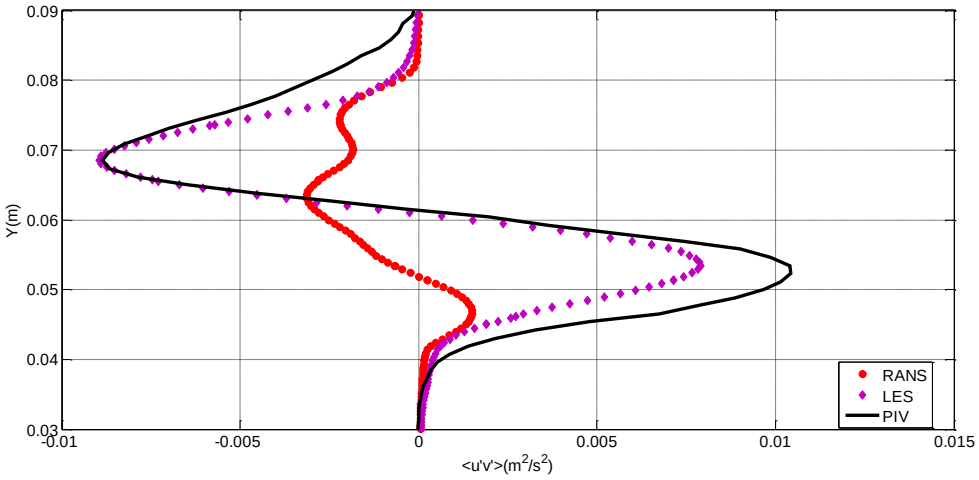

Figure 4.20 Profile of $\langle u'v' \rangle$ at section 1

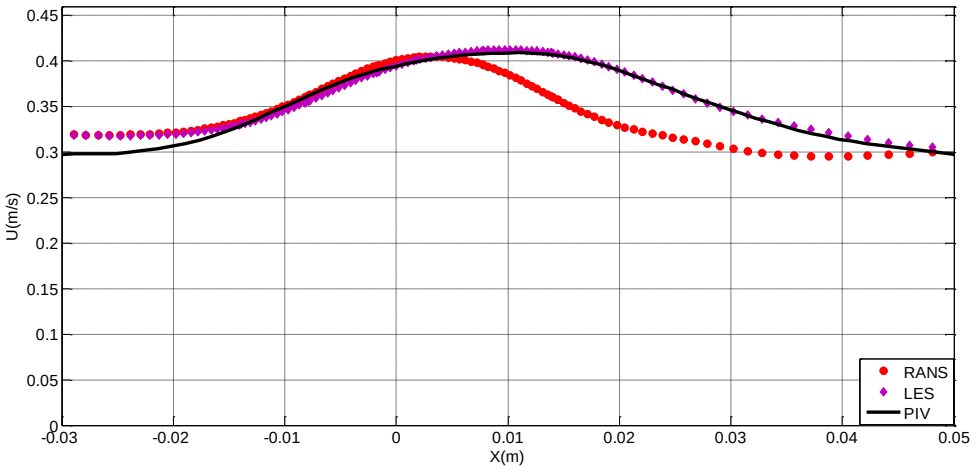

Figure 4.21 Time-averaged horizontal velocity at section 2

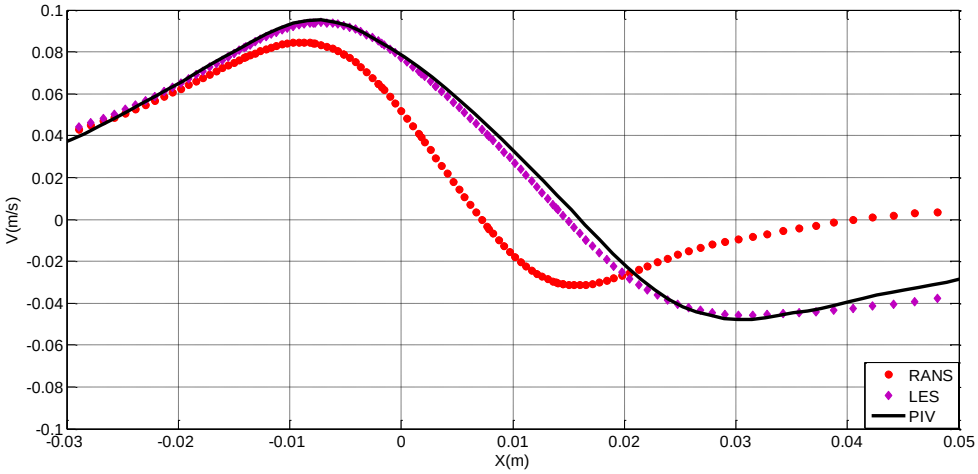

Figure 4.22 Time averaged vertical velocity at section 2

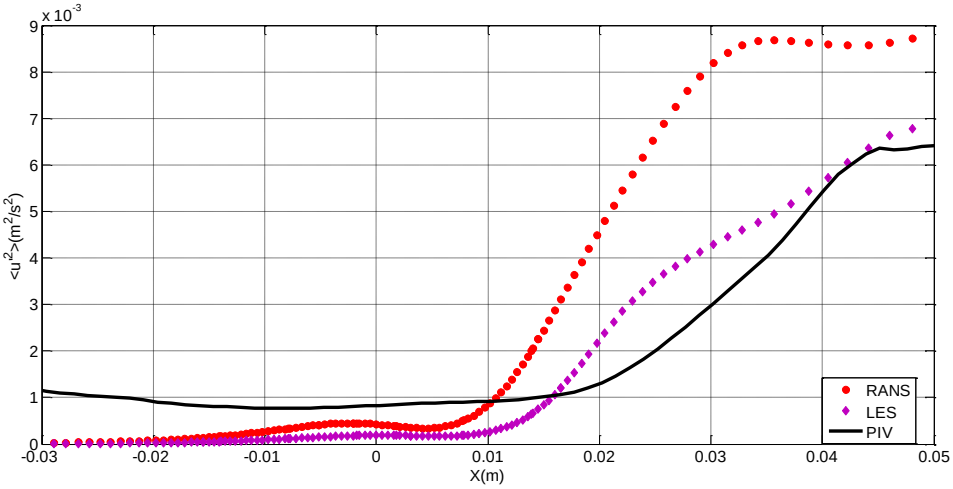

Figure 4.23 Profile of $\langle u'^2 \rangle$ at section 2

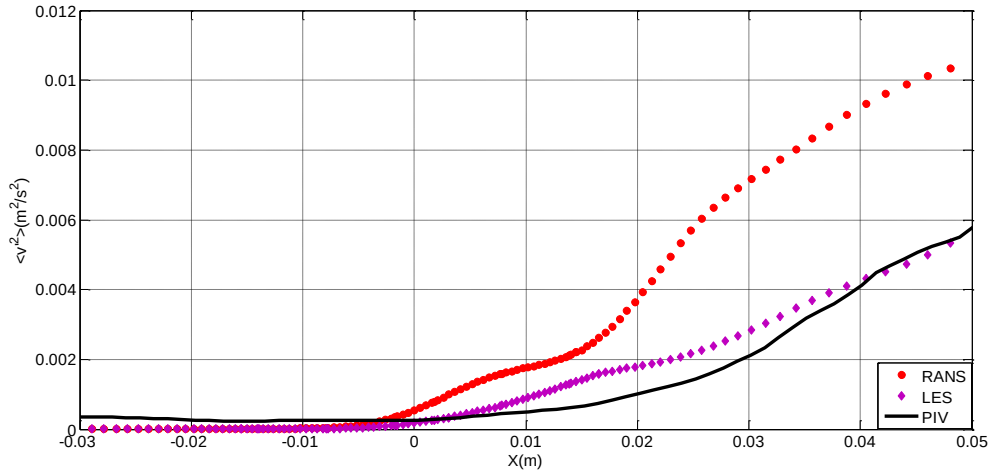

Figure 4.24 Profile of $\langle v'^2 \rangle$ at section 2

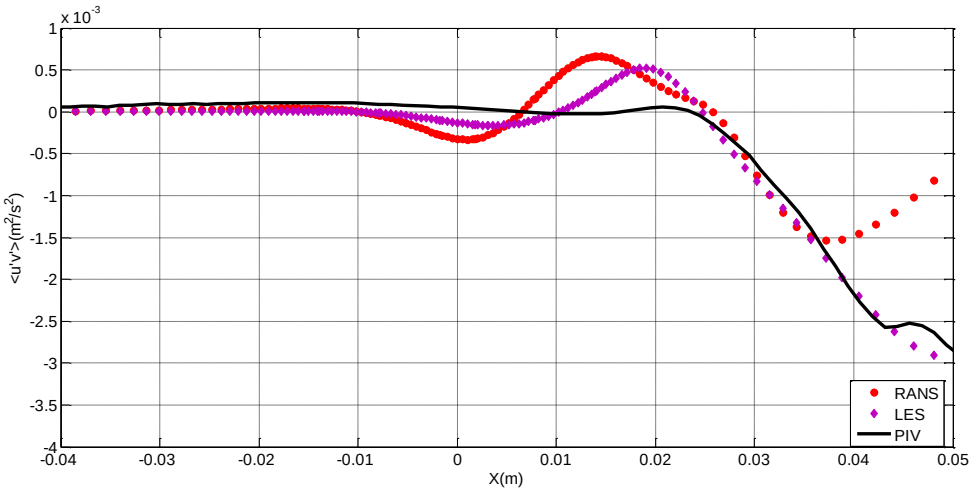

Figure 4.25 Profile of $\langle u'v' \rangle$ at section 2

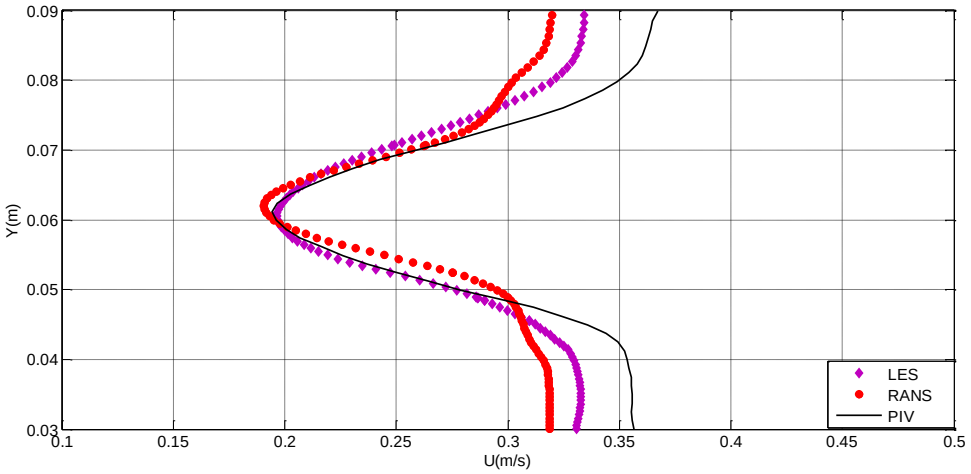

Figure 4.26 Time-averaged horizontal velocity at section 3

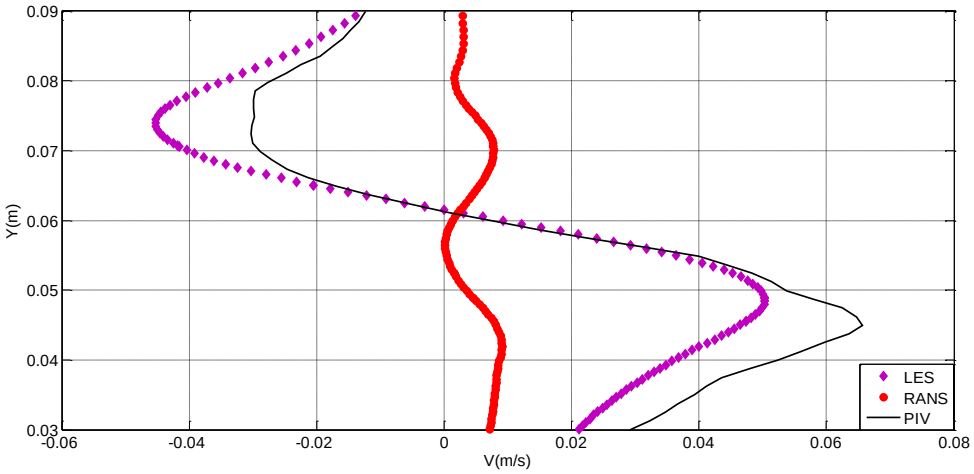

Figure 4.27 Time-averaged vertical velocity at section 3

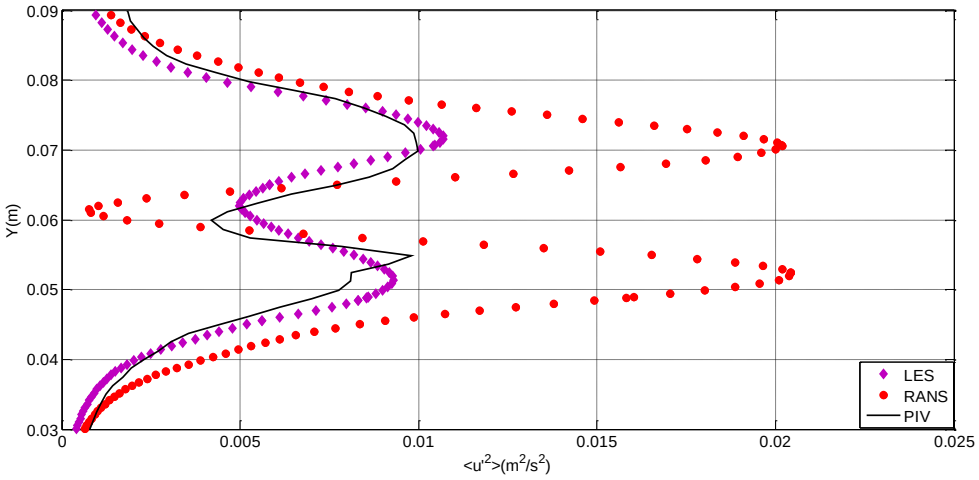

Figure 4.28 Profile of $\langle u'^2 \rangle$ at section 3

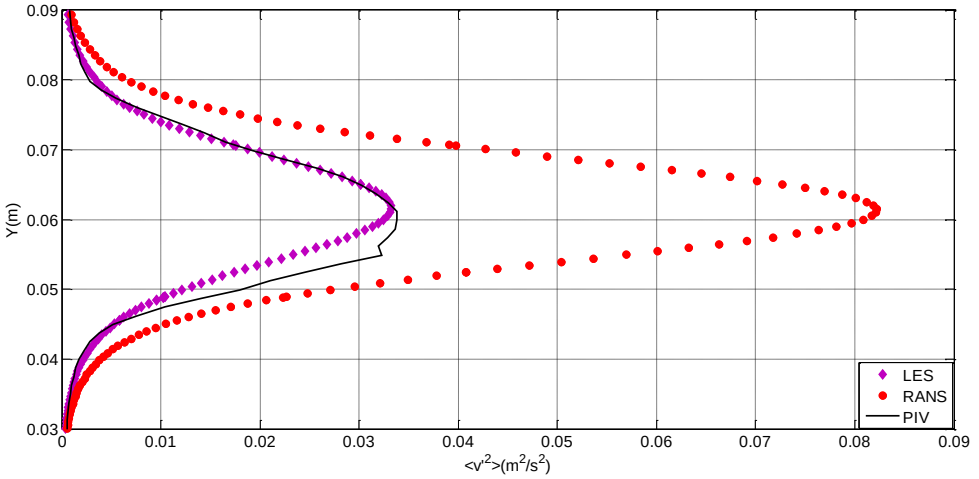

Figure 4.29 Profile of $\langle v'^2 \rangle$ at section 3

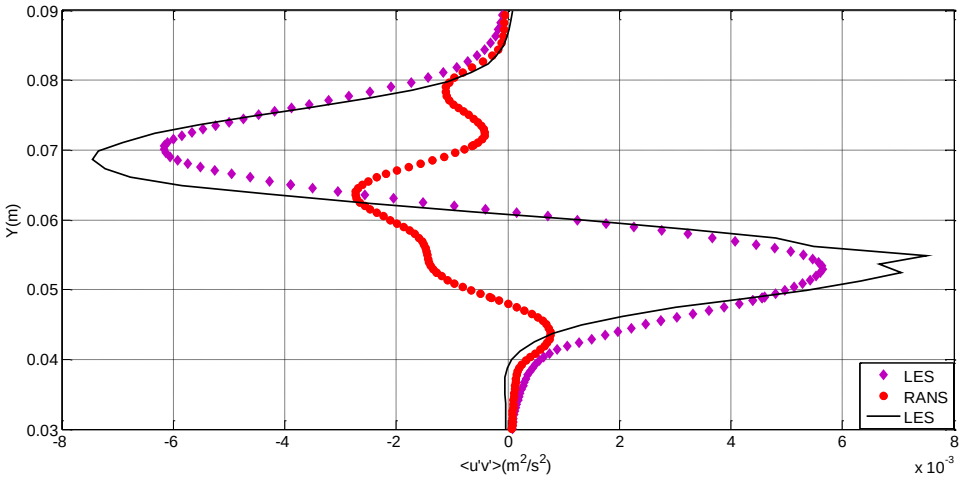

Figure 4.30 Profile of $\langle u'v' \rangle$ at section 3

At all three sections, the time-averaged velocities of LES simulation and PIV experiment are pretty close to each other. The divergence between RANS and the other two methods is significant. At section 1 and section 3, RANS simulation tends to provide smaller vertical velocities. At section 1, when approaching the center of cylinder, the RANS horizontal velocity is larger than those of the other two methods. However, at section 3, the performance of RANS is better concerning the horizontal velocity. At section 2, the effects of the presence of cylinder on horizontal velocity are more significant in LES and PIV than RANS, which means greater changes of the horizontal velocity in LES and PIV.

At section 1 the correlation concerning$\langle u'^2 \rangle$ among the three methods is poor. It is possibly due to the quality and uncertainties of the PIV measurement. However, LES has a better correlation with PIV than RANS concerning the other two Reynolds stresses. At

section 2 and section 3, all the three Reynolds stresses from LES and PIV are quite close to each other. If we pay attention to the $\langle v'^2 \rangle$, LES provides a nearly perfect prediction at both section 1 and section 3. Also, at section 3 the correlation between LES and PIV concerning $\langle u'^2 \rangle$ is better than section 1.

4.4 Turbulence intensity of inflow

In both RANS and LES cases, the turbulence intensity of flow is 2%. It is the based on the analysis of the time history of velocity of a specific point of the inflow. To study the effects of turbulence intensity on results, the RANS case is run with zero turbulence intensity of inflow. Time averaged velocities and Reynolds stresses are compared (Figure 4.31, Figure 4.32, Figure 4.33, Figure 4.34 and Figure 4.35) at section 1, which is at the downstream of cylinder. From the comparisons, we can see that the effects of turbulence intensity of inflow are not significant, even negligible for the horizontal velocity.

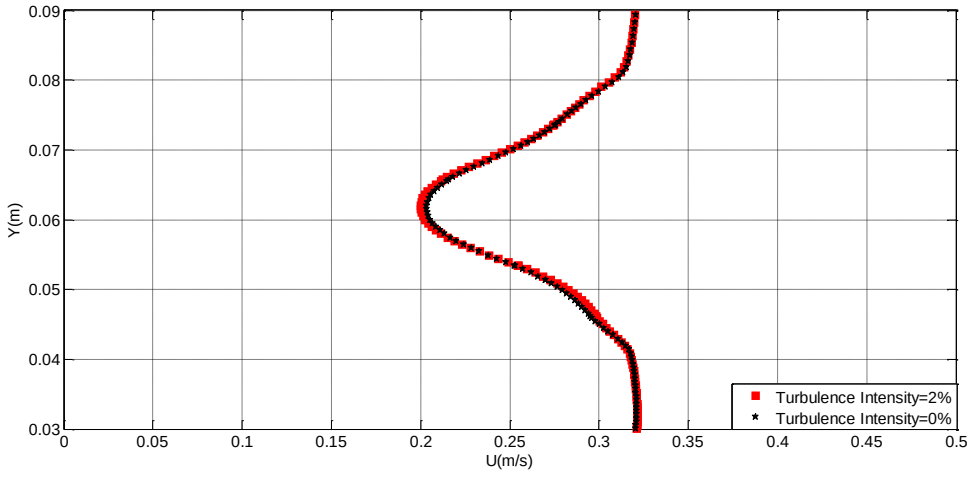

Figure 4.31 Comparison of time-averaged horizontal velocity for two turbulence intensities at section 1

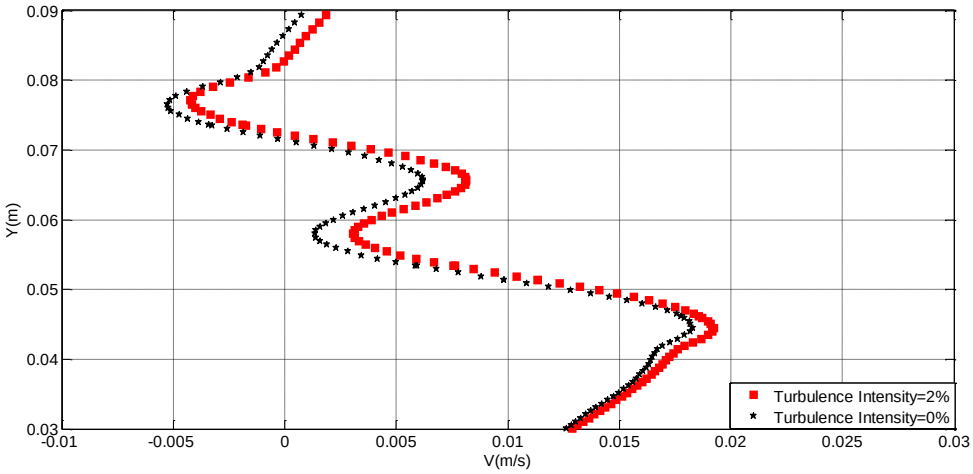

Figure 4.32 Comparison of time-averaged vertical velocity for two turbulence intensities at section 1

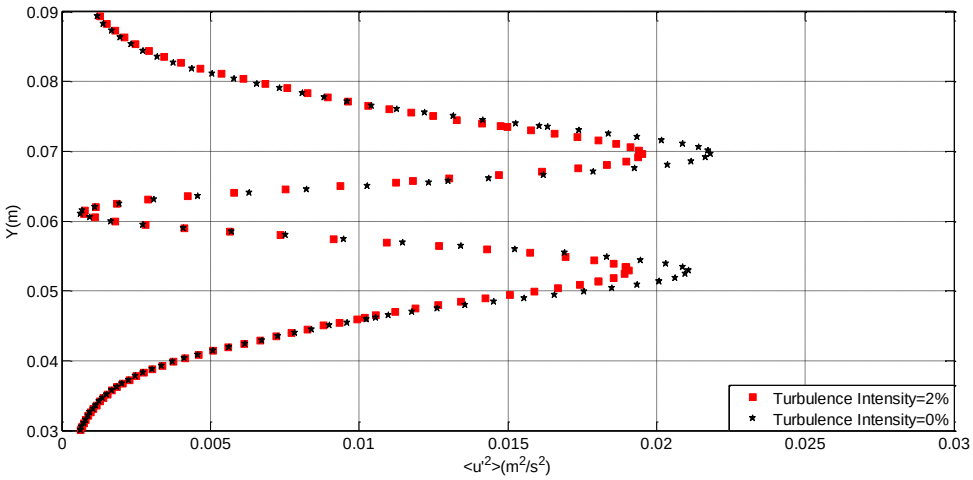

Figure 4.33 Comparison of $\langle u'^2 \rangle$ for two different turbulence intensities at section 1

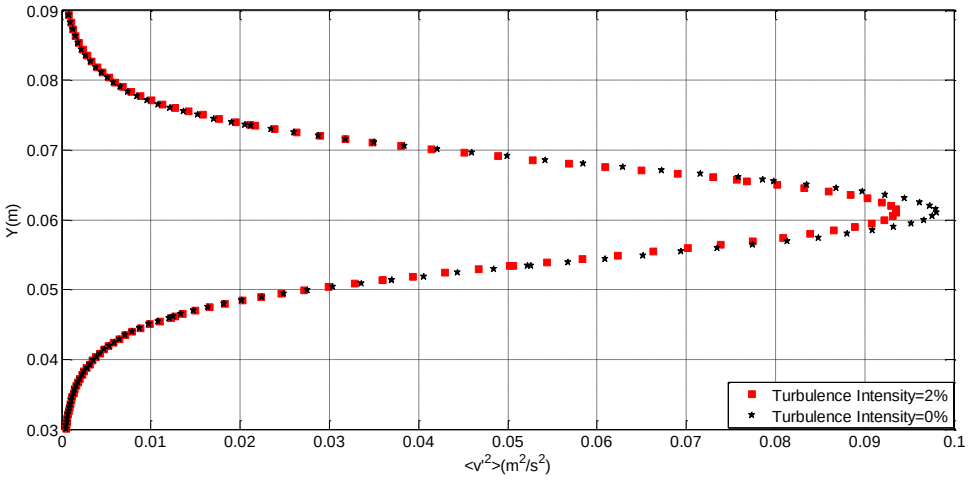

Figure 4.34 Comparison of $\langle v'^2 \rangle$for two different turbulence intensities at section 1

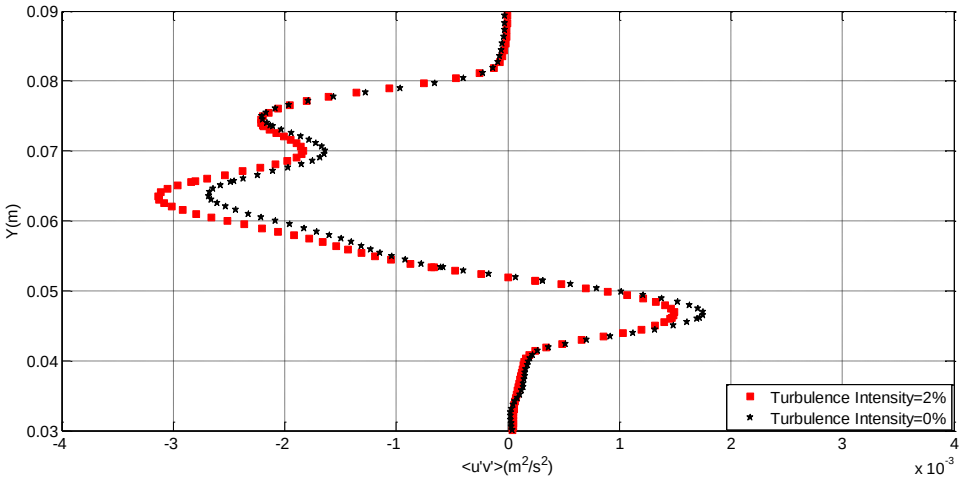

Figure 4.35 Comparison of $\langle u'v' \rangle$for two different turbulence intensities at section 1

4.5 CFD simulations including free surface

In the PIV experiment, the top side of the measured domain is under the free surface, instead of at the positon of free surface. Thus, in the CFD simulations, the domain is just one part of the whole flow field, which does not include the free surface. To study

whether the free surface has significant effects on the results, two meshes (2D and 3D) including free surface are created (Figure 4.36 and Figure 4.37) and two CFD simulations applying the new meshes are run. In the two simulations including free surface, the boundary condition for the top side of the original small domain is no longer needed. To simplify the problem, the air above the free surface is not considered. The boundary condition for the free surface is stationary wall with zero shear stress. For the lower part of the inflow, the velocity profile is the same as original simulations. For the higher part of the inflow, the velocity is the same as the free stream velocity, 0.35m/s. The turbulence intensity for the inflow is still 2%. The distance between the inflow and the center of cylinder is still 18.5 cm. However, the distance between the center of cylinder and outflow is extended from 11.9 cm to 30.0 cm. The comparison is made at the section 1, including time-averaged velocity profiles (Figure 4.38 and Figure 4.39) and Reynolds stresses (Figure 4.40, Figure 4.41 and Figure 4.42). In the simulations including free surface, the horizontal velocities tend to be larger than those of the simulations without free surface.

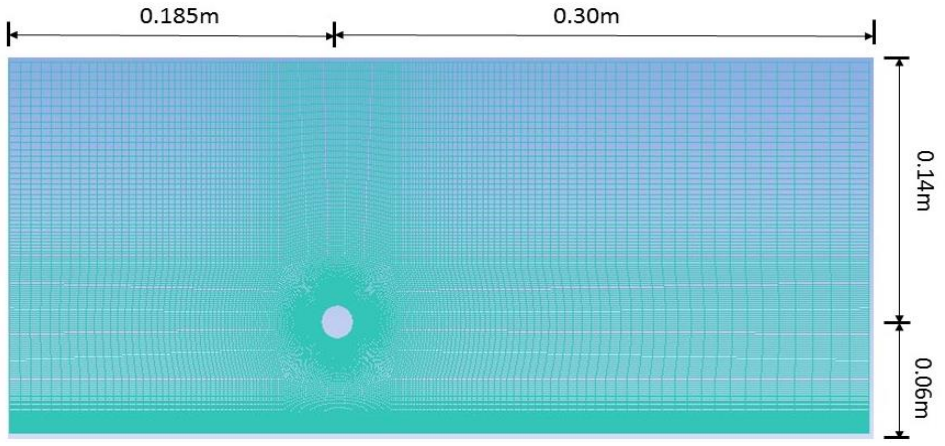

Figure 4.36 2D mesh including free surface

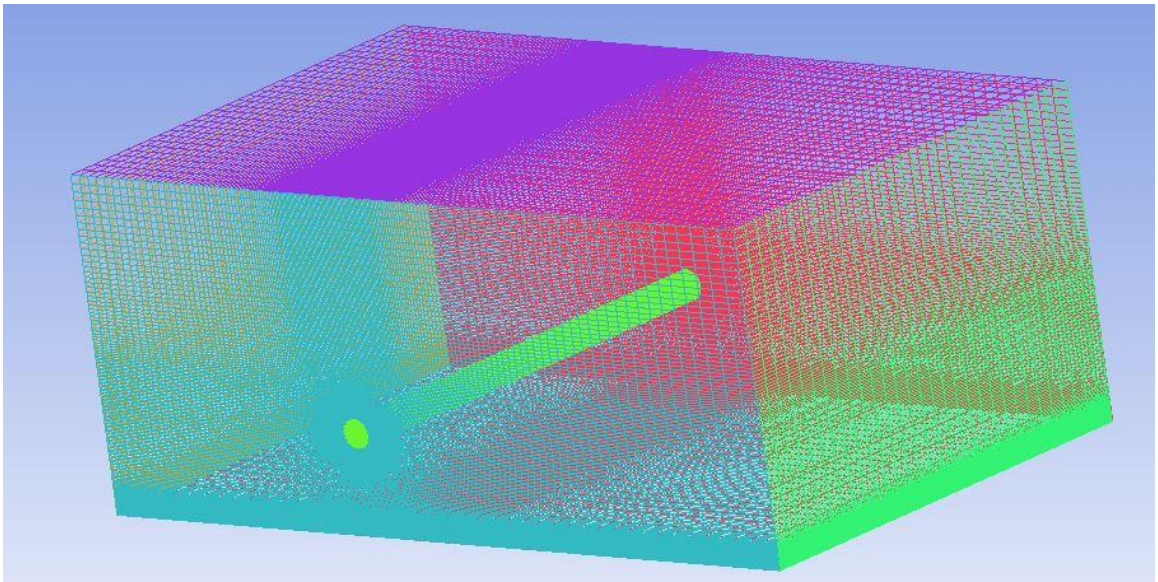

Figure 4.37 3D mesh including free surface

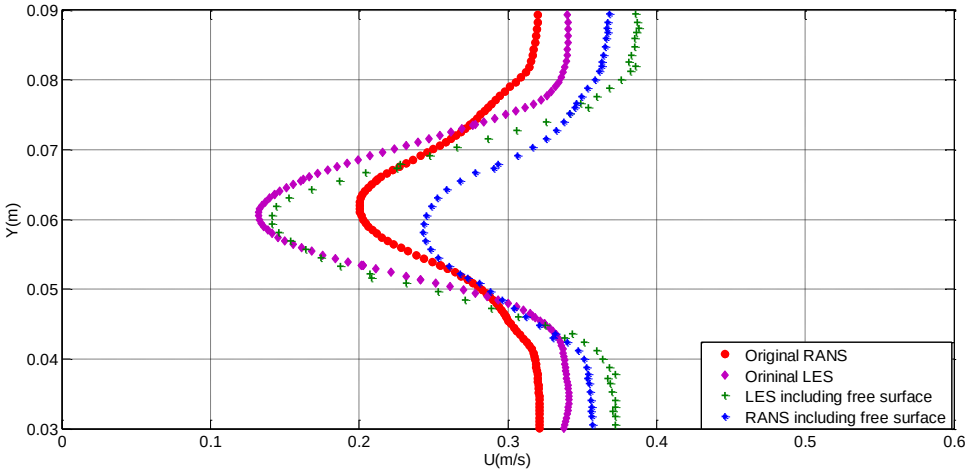

Figure 4.38 Comparison of time averaged horizontal velocity with and without free surface at section 1

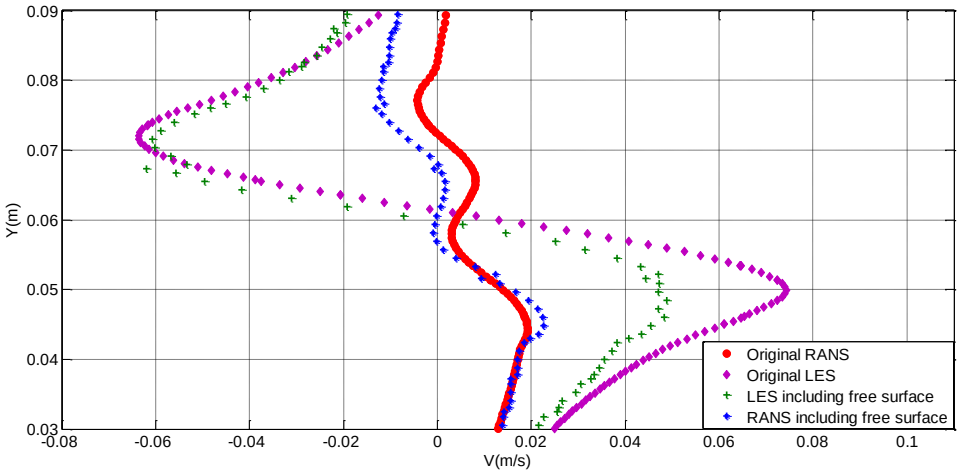

Figure 4.39 Comparison of time averaged vertical velocity with and without free surface at section 1

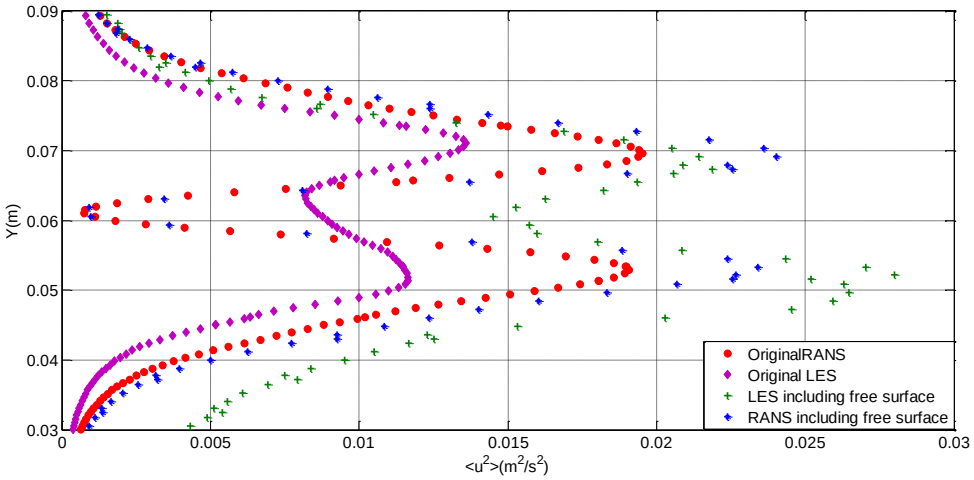

Figure 4.40 Comparison of $\langle u'^2 \rangle$ with and without free surface at section 1

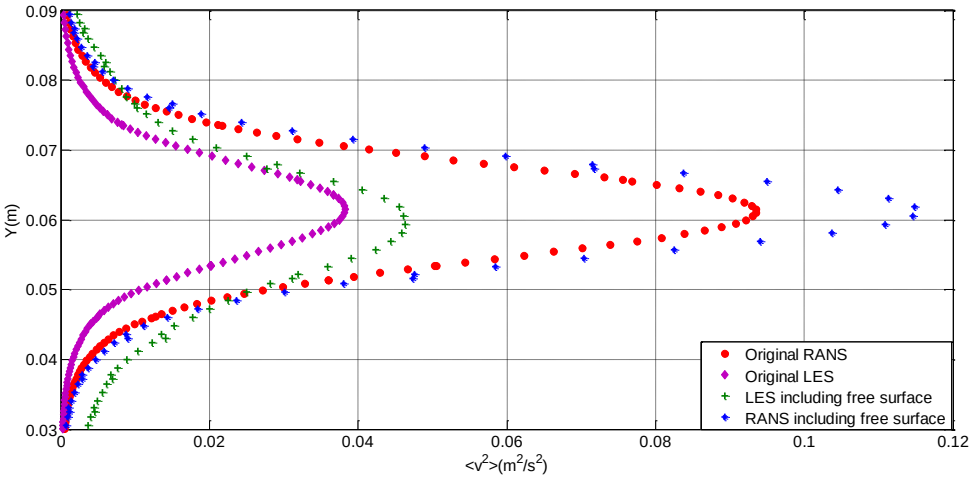

Figure 4.41 Comparison of $\langle v'^2 \rangle$ with and without free surface at section 1

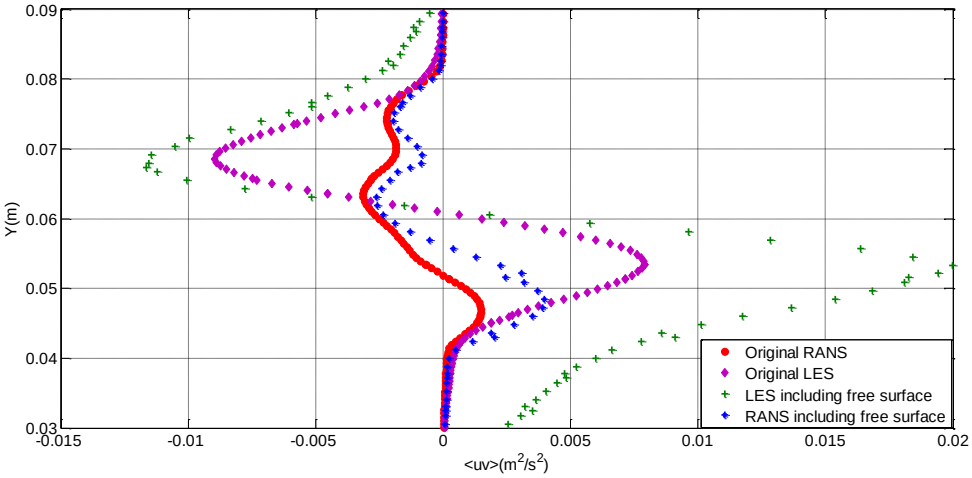

Figure 4.42 Comparison of $\langle u'v' \rangle$ with and without free surface at section 1

Chapter 5 Assessment of Morison's Equation

5.1 Introduction

This chapter is aimed at the assessment of Morison's equation using CFD. As shown in Figure5.1, this problem is in two dimensions. The cylinder is subject to an oscillating flow with $U = U_m \cdot \cos(\omega t)$, where U_m is the amplitude of the flow velocity, ω is the frequency of the flow and t is the flow time.

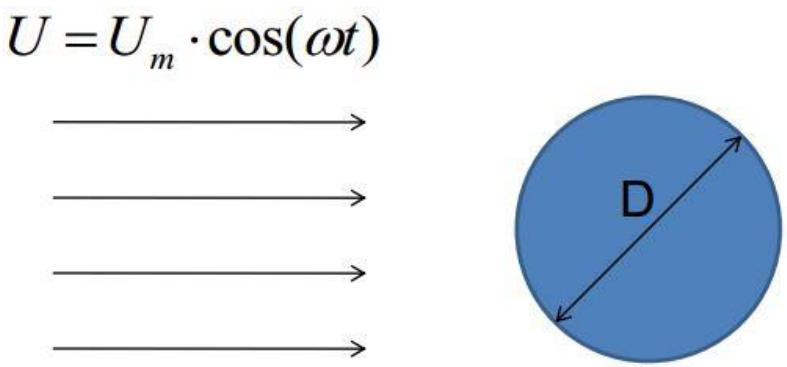

Figure 5.1 Two dimensional cylinder in oscillating flow

There are two important numbers, Reynolds number $(Re) = \frac{U_m D}{\nu}$, where U_m is the amplitude of velocity of the oscillatory flow, and Keulegan-Carpenter number $(KC) = \frac{U_m T}{D}$ $(T = \frac{2\pi}{\omega})$, where T is the period of the oscillating flow. The main task of this part is to study and compare cases with different combinations of Reynolds number (Re) and Keulegan–Carpenter number (KC). The evaluations of C_d and C_M will be conducted based on the results from CFD.

5.2 Methodology

5.2.1 Geometry and mesh

One two dimensional mesh is created in the ANSYS CFD ICEM meshing software. The center of the cylinder is at the origin of the coordinate system. To make sure that the boundaries do not restrict the alternating flow, the flow field should be large enough. W=100D and L=100D. Thus,the geometry is symmetric about both x and y axes. There are 108,000 cells in this mesh (Figure 5.2). The Y-Plus values on the cylinder are shown in Figure 5.3.

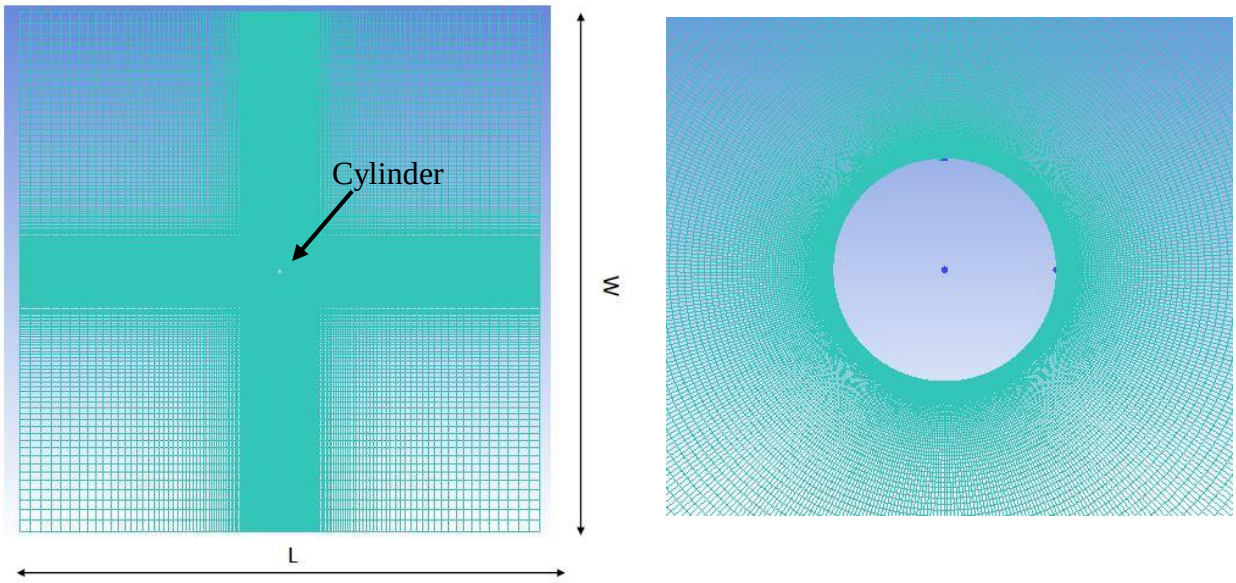

(a)Full view of the two dimensional mesh, W=100D, L=100D

(b) Closeup in the vicinity of cylinder

Figure 5.2 Two dimensional mesh

Figure 5.3 Y-Plus values on the surface of cylinder

5.2.2 Turbulence models

Basically RANS is applied in this research. In RANS, the two-equation k-ω shear-stress transport (SST) eddy viscosity model will be adopted (Eswaran and Biswas 2002). In order to study the effects of turbulence model on the result, the Reynold's Stress Model (RSM) is applied (Hanjalic and Launder 1972), which is a higher level, elaborate turbulence model. In RSM, the eddy viscosity approach has been discarded and the Reynolds stresses are directly computed. The exact Reynolds stress transport equation accounts for the directional effects of the Reynolds stress fields.

5.2.3 Boundary conditions

The boundary condition for the left side of the geometry is velocity-inlet. The velocity is given as equation 5.4.

$$U = U_m \cdot \cos(\omega t) \tag{5.4}$$

The realization of the periodic velocity is through the application of user defined function (UDF). The top and bottom sides of the geometry are set as symmetry. The right side is set as pressure outlet. Finally, the boundary condition for the cylinder is no-slip wall.

5.2.4 Evaluation of C_D and C_M

We first define that $C_x = \frac{F}{\frac{\rho}{2}U_m^2 D}$. The time history of C_x can be obtained from the application of surface monitor in the Ansys Fluent. From Morison's equation, C_x can be given as

$$C_x = C_D \cos(\omega t)\left|\cos(\omega t)\right| - \frac{\omega \pi D C_m \sin(\omega t)}{2U_m} \tag{5.5}$$

Then the integral of C_x, which is from CFD simulation, is performed as equation 5.6.

$$\int_0^{\frac{T}{2}} C_x dt = \int_0^{\frac{T}{2}} C_D \cos(\omega t)\left|\cos(\omega t)\right| - \frac{\omega \pi D C_m \sin(\omega t)}{2U_m} dt \tag{5.6}$$

From the above integral, C_M can be calculated as equation 5.7

$$C_M = -\frac{U_m}{\pi D}\int_0^{\frac{T}{2}} C_x dt \tag{5.7}$$

The second integral is performed as equation 5.8

$$\int_0^{\frac{T}{2}} C_x \cos(\omega t) dt = \int_0^{\frac{T}{2}} C_D \cos^2(\omega t)\left|\cos(\omega t)\right| - \frac{\omega \pi D C_m \sin(\omega t)\cos(\omega t)}{2U_m} dt \tag{5.8}$$

From the second integral, C_D can be calculated as equation (5.9)

$$C_D = \frac{\int_0^{\frac{T}{2}} C_x \cos(\omega t) dt}{\int_0^{\frac{T}{2}} \cos^2(\omega t) |\cos(\omega t)| dt} \quad (5.9)$$

Equation 5.7 and Equation 5.9 are calculated over five periods and then averaged to get the final results.

5.2.5 Combinations of KC and Re

There are totally 21 different combinations of KC and Re as shown in Table 5.1. There are three different Reynolds numbers: 1,070, 20,000 and 300,000. There are seven different Keulegan–Carpenter numbers: 2, 6, 12, 20, 30, 40 and 50.

5.3 Correlation between CFD and Morison's equation

5.3.1 Inviscid flow

In order to verify that $C_M = 2$ for inviscid flow around 2-D cylinder, the case of inviscid flow is run first. In this case, $U_m = 0.3 m/s$ and $KC = 12$. With $C_M = 2$ and $C_D = 0$, Morison's equation provides a good correlation with the C_x from CFD (Figure 5.4).

Table 5-1 Combinations of KC and Re

Case No.	KC	Re
1	2	1,070
2	6	1,070
3	12	1,070
4	20	1,070
5	30	1,070
6	40	1,070
7	50	1,070
8	2	20,000
9	6	20,000
10	12	20,000
11	20	20,000
12	30	20,000
13	40	20,000
14	50	300,000
15	2	300,000
16	6	300,000
17	12	300,000
18	20	300,000
19	30	300,000
20	40	300,000
21	50	300,000

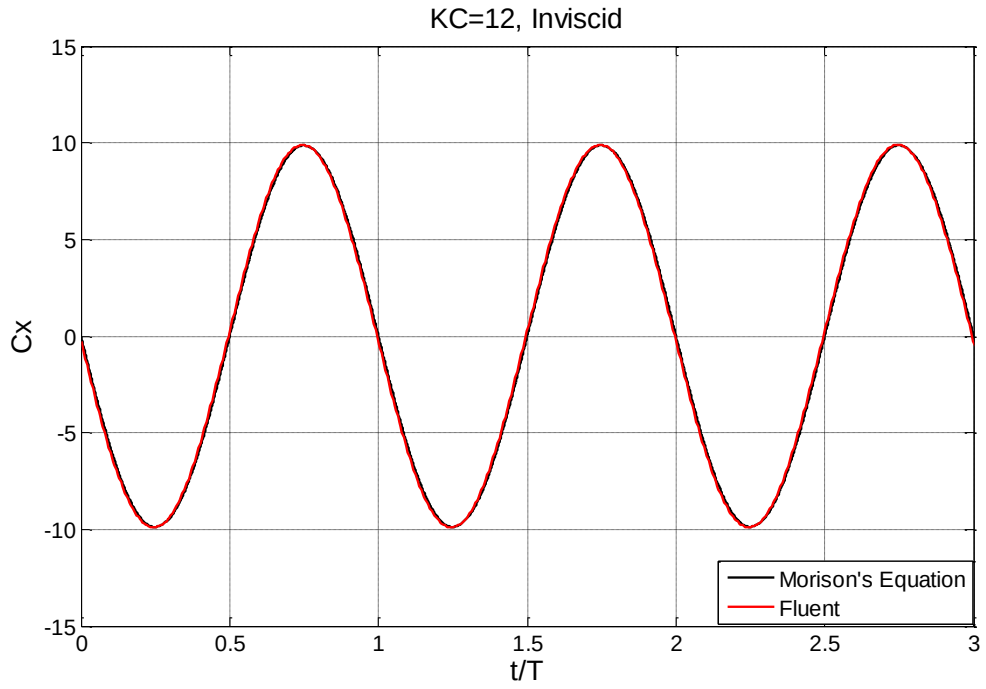

Figure 5.4 C_x for inviscid flow

5.3.2 **Viscous flow**

For the viscous flow, there are 21 cases as shown in Table 5.1. The time is normalized by the period of each case. The range of time is from 0 to 5 periods. The time histories of C_x from both CFD simulation and Morison's equation are compared for each case (Figure 5.5 to Figure 5.25).

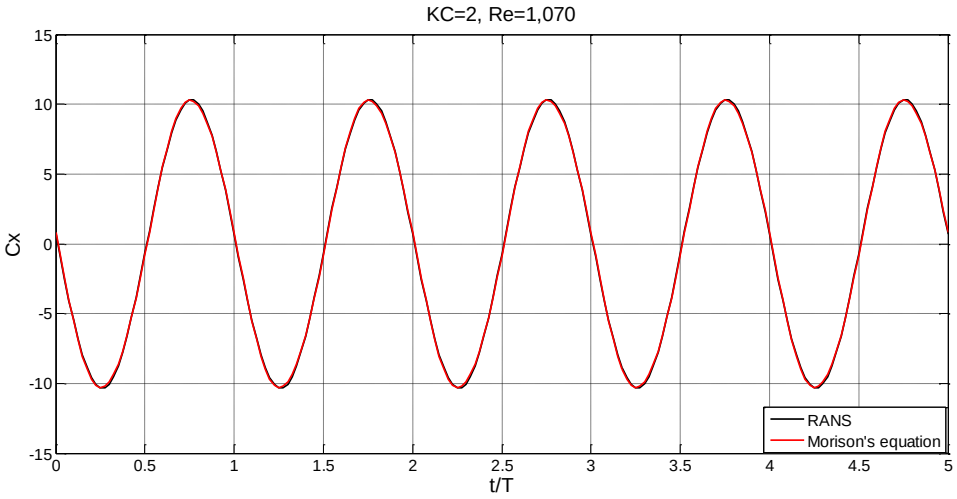

Figure 5.5 C_x for $KC = 2$ and $Re = 1{,}070$

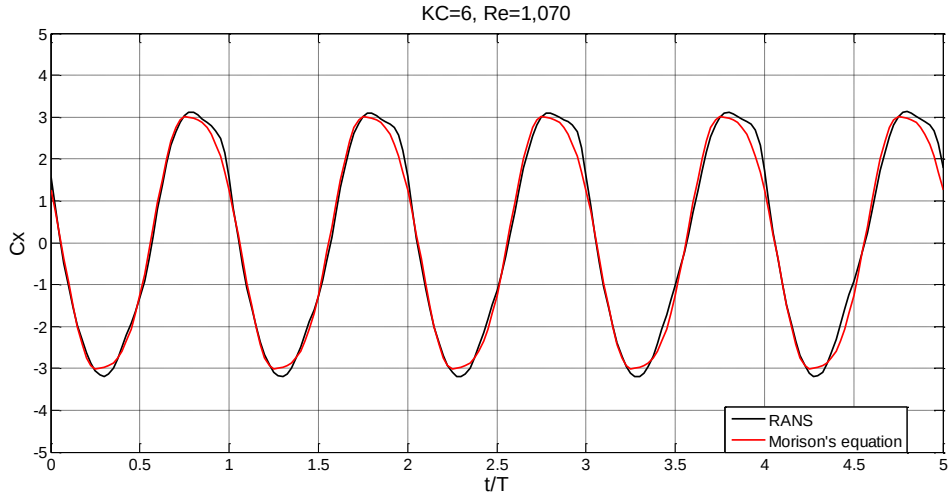

Figure 5.6 C_x for $KC = 6$ and $Re = 1{,}070$

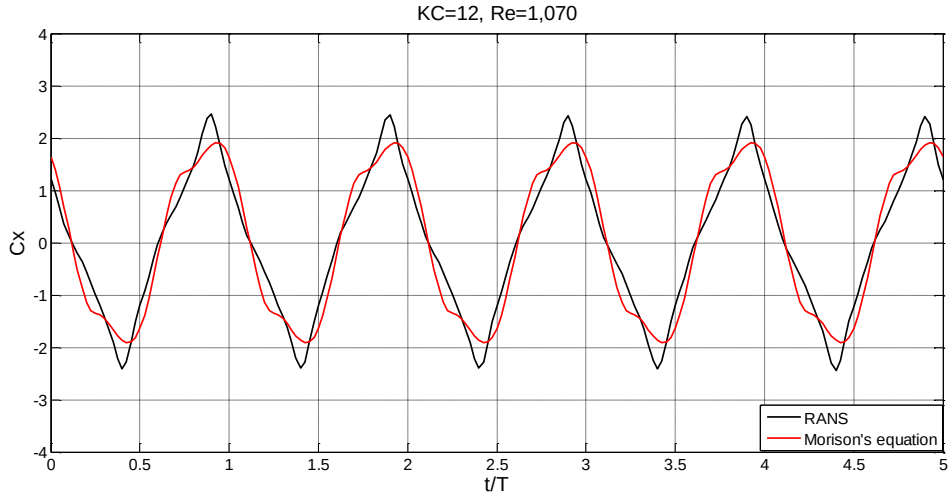

Figure 5.7 C_x for $KC = 12$ and $Re = 1{,}070$

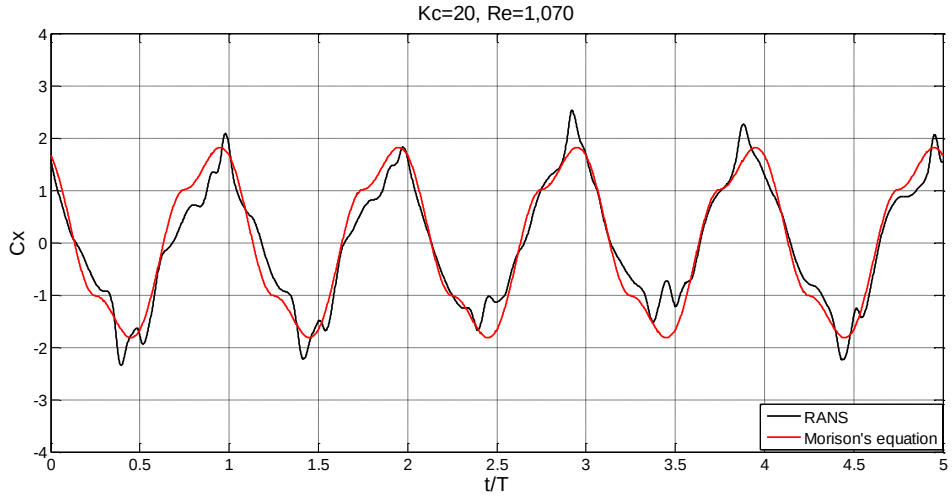

Figure 5.8 C_x for $KC = 20$ and $Re = 1{,}070$

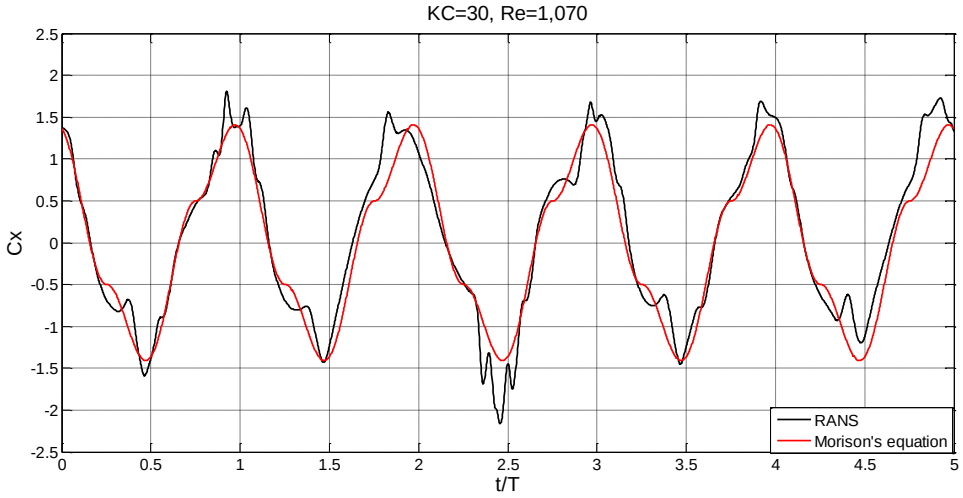

Figure 5.9 C_x for $KC = 30$ and $Re = 1{,}070$

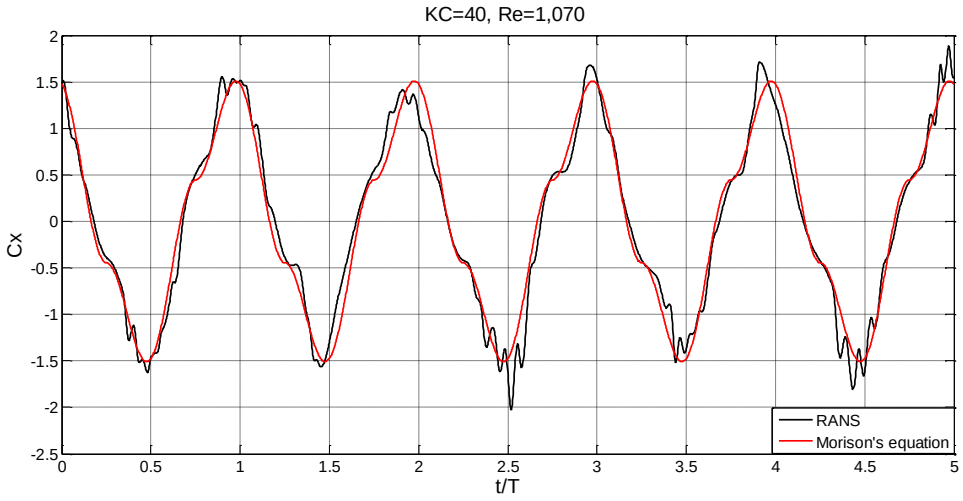

Figure 5.10 C_x for $KC = 40$ and $Re = 1{,}070$

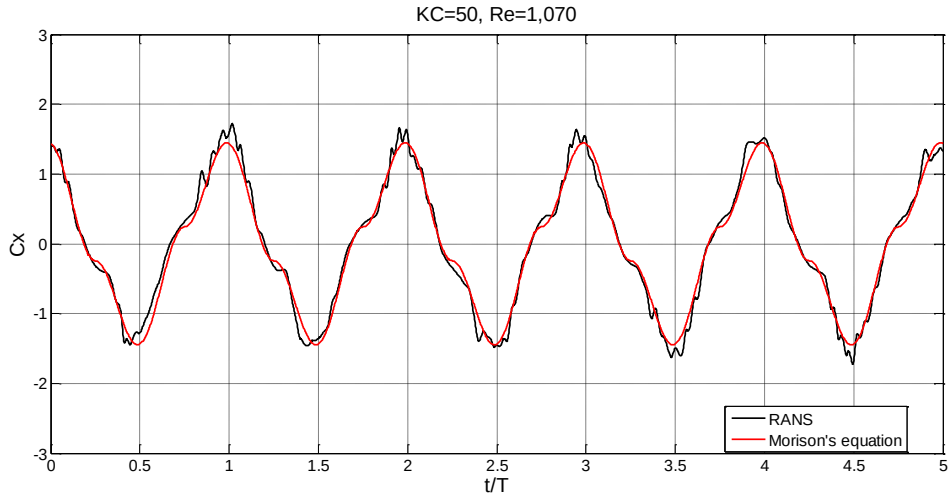

Figure 5.11 C_x for $KC = 50$ and $Re = 1{,}070$

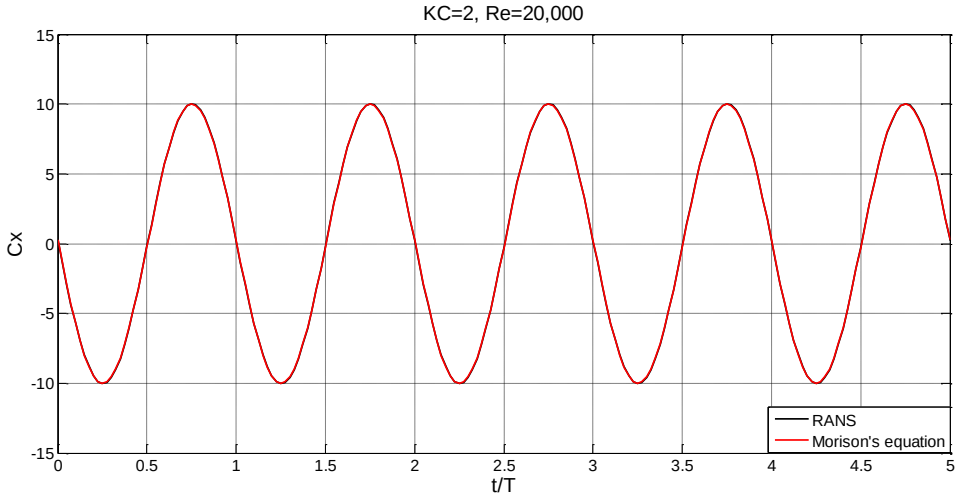

Figure 5.12 C_x for $KC = 2$ and $Re = 20{,}000$

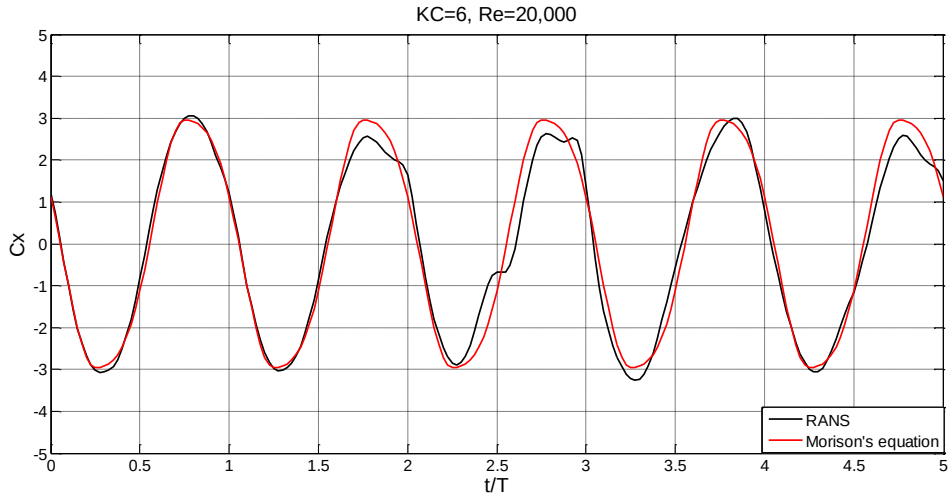

Figure 5.13 C_x for $KC = 6$ and $Re = 20{,}000$

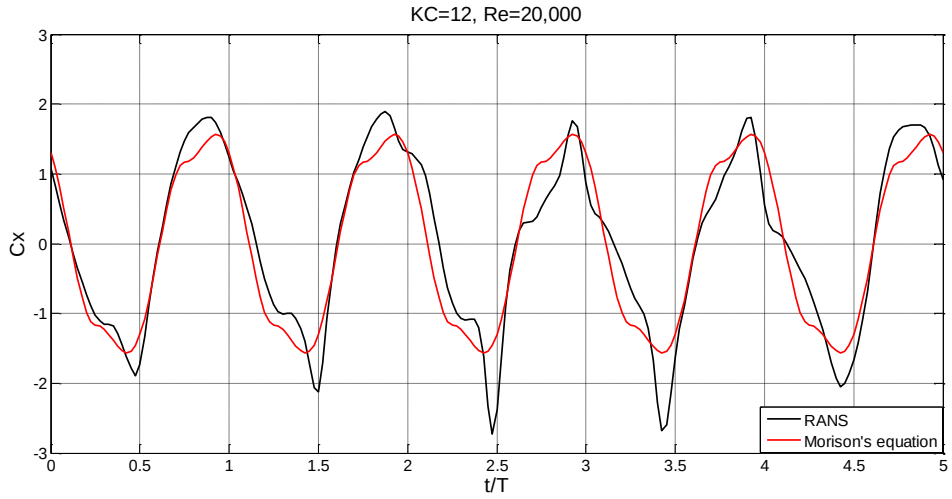

Figure 5.14 C_x for $KC = 12$ and $Re = 20{,}000$

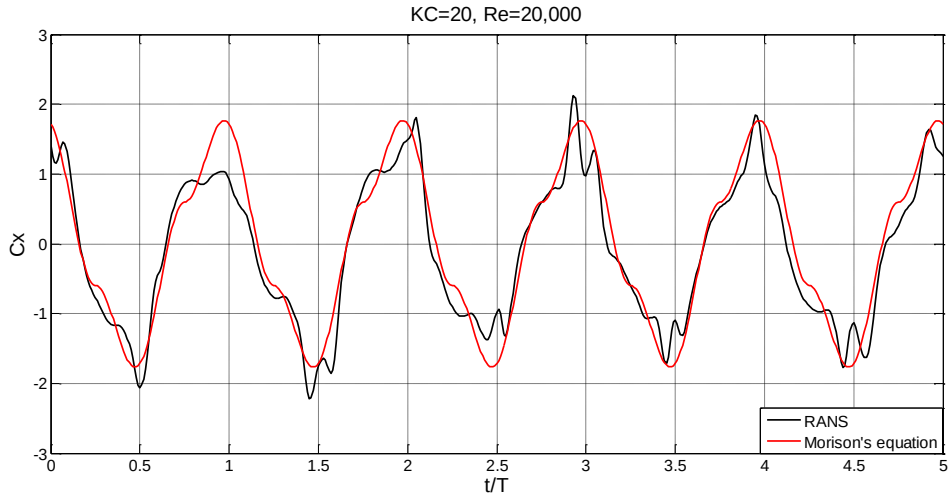

Figure 5.15 C_x for $KC = 20$ and $Re = 20{,}000$

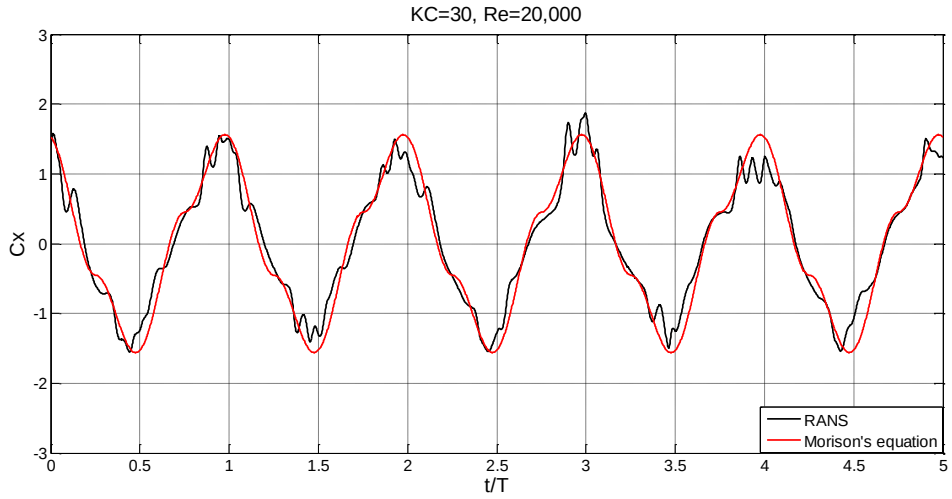

Figure 5.16 C_x for $KC = 30$ and $Re = 20{,}000$

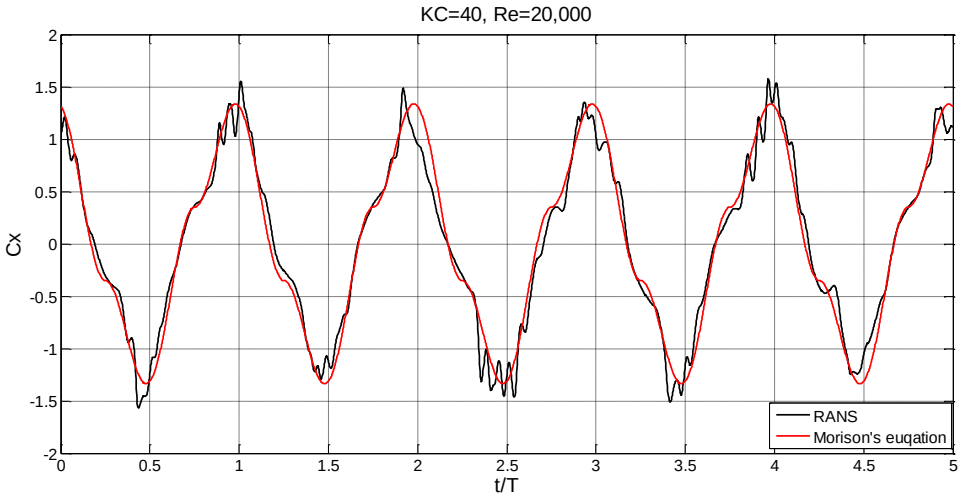

Figure 5.17 C_x for $KC = 40$ and $Re = 20{,}000$

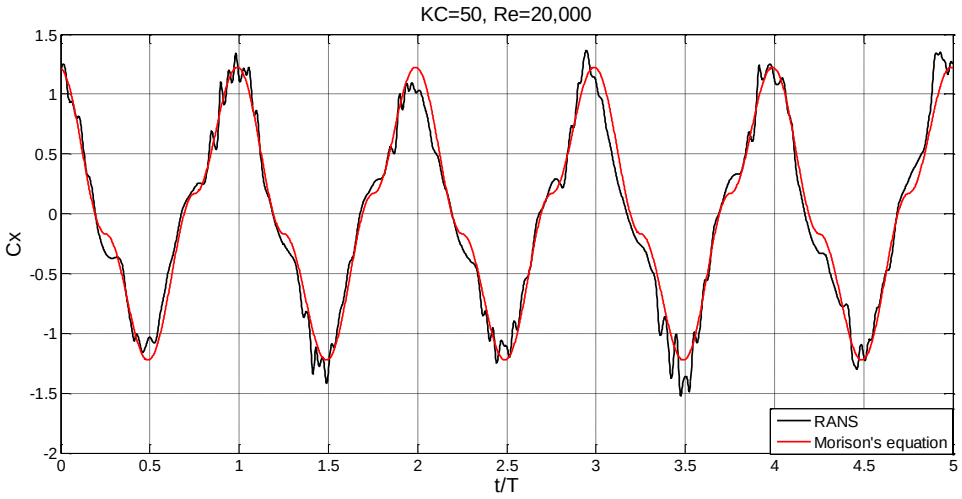

Figure 5.18 C_x for $KC = 50$ and $Re = 20{,}000$

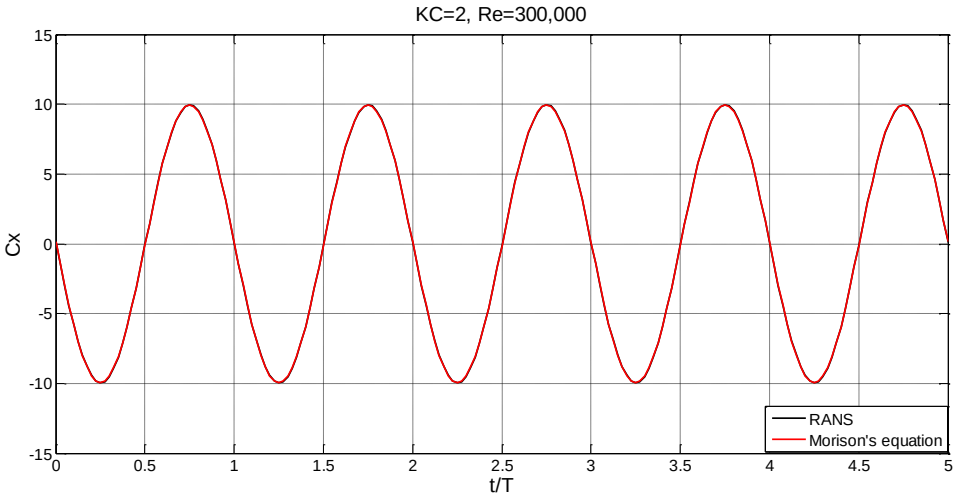

Figure 5.19 C_x for $KC = 2$ and $Re = 300{,}000$

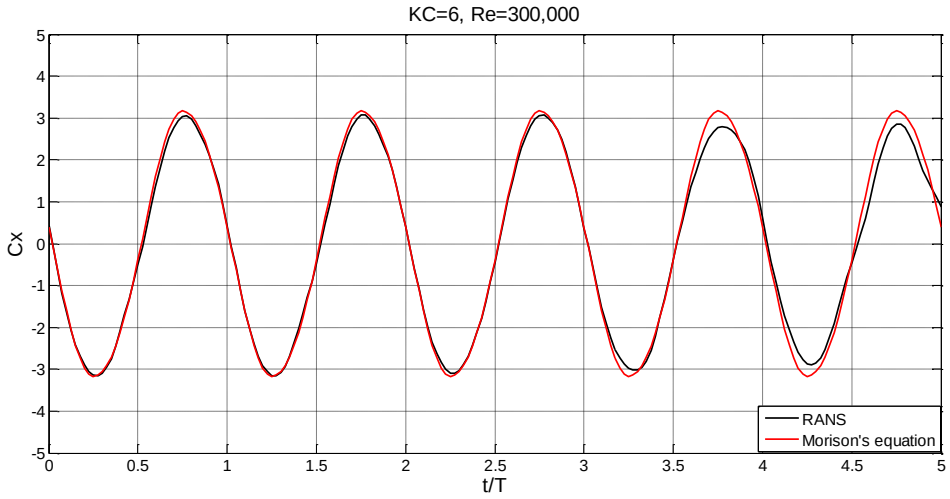

Figure 5.20 C_x for $KC = 6$ and $Re = 300{,}000$

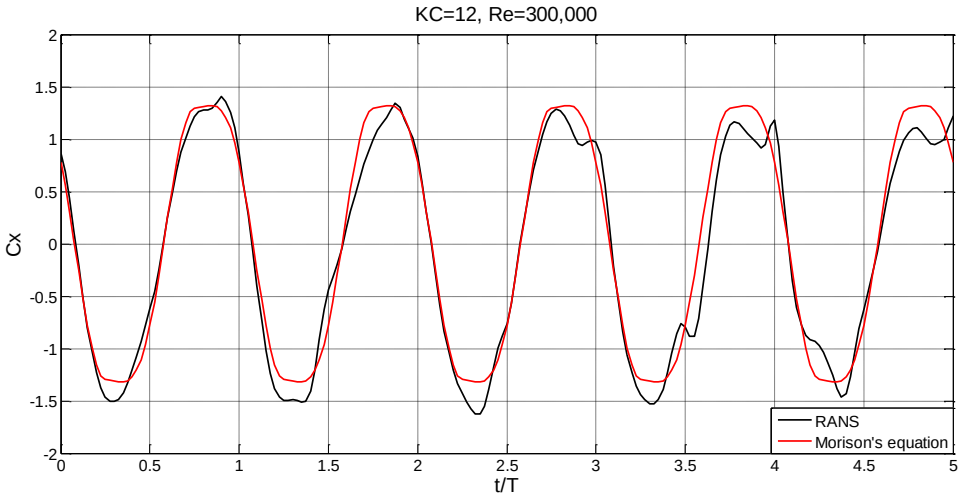

Figure 5.21 C_x for $KC = 12$ and $Re = 300{,}000$

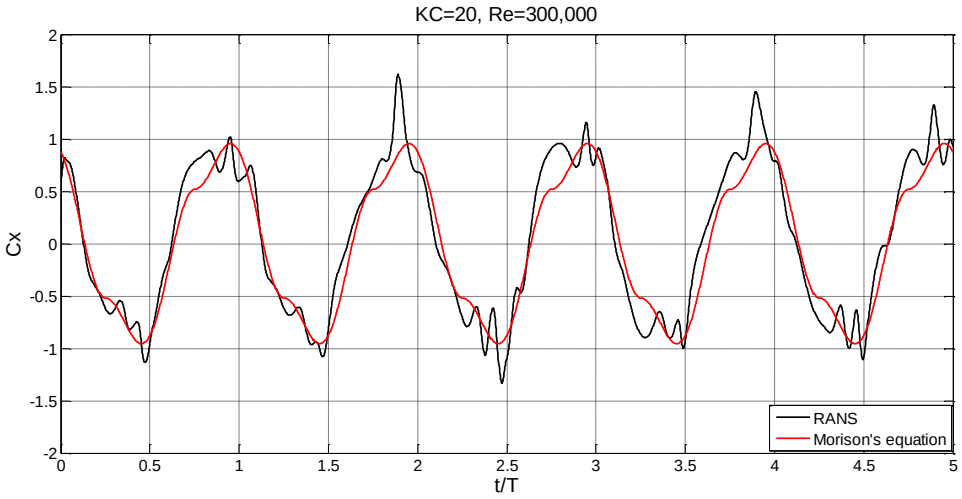

Figure 5.22 C_x for $KC = 20$ and $Re = 300{,}000$

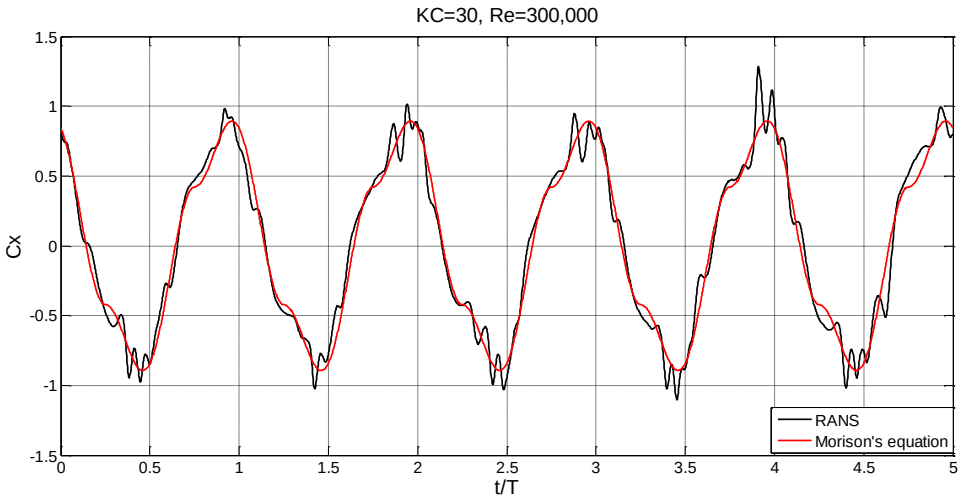

Figure 5.23 C_x for $KC = 30$ and $Re = 300{,}000$

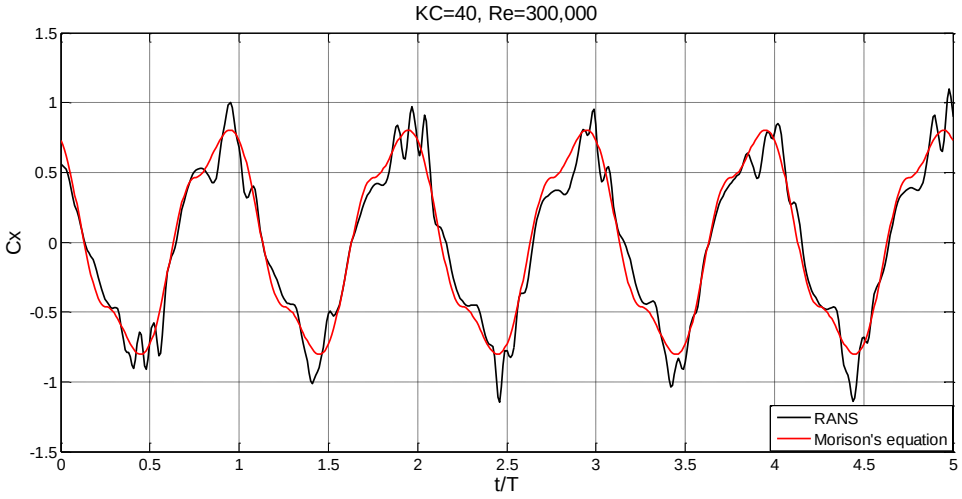

Figure 5.24 C_x for $KC = 40$ and $Re = 300{,}000$

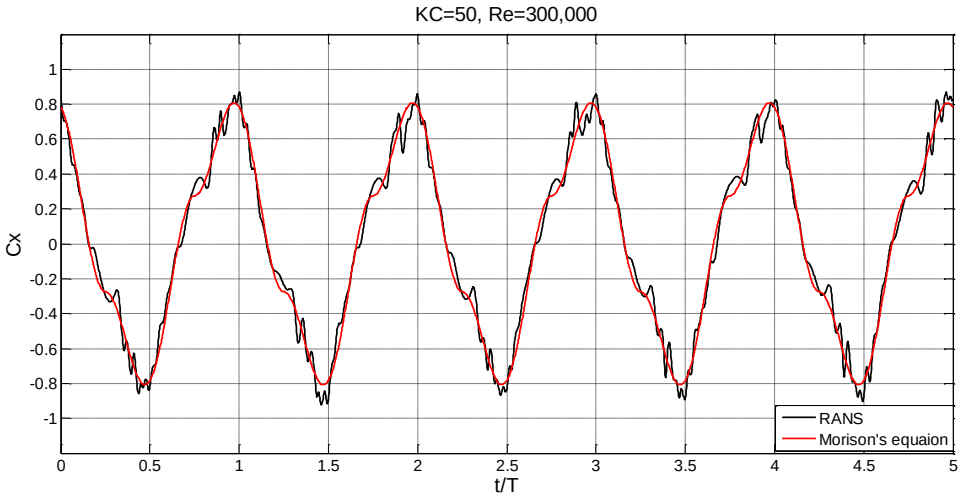

Figure 5.25 C_x for $KC = 50$ and $Re = 300{,}000$

For low KC numbers ($KC \leq 12$), the profiles of C_x from CFD are smooth and the Morison's equation can match those quite well. When KC number become larger ($KC \geq 20$), the profiles of C_x from CFD are no longer smooth and there are some fluctuations，especially at the crest and trough. It is hard for Morison's equation to match those fluctuations. However, the Morison's equation can still provide a good estimation of the general trend of profiles of C_x, including mean values, maximum and minimum values, and the general shape of the profiles.

5.3.3 Analyses of C_M and C_D

Based on the data from different combinations of Re and KC, we can get the corresponding values of C_M and C_D. The relations between KC and C_D are shown in Figure 5.26 for three different Reynolds numbers (1,070, 20,000 and 300,000). The relations

between KC and C_M are shown in Figure 5.27 for three different Reynolds numbers (1,070, 20,000 and 300,000).

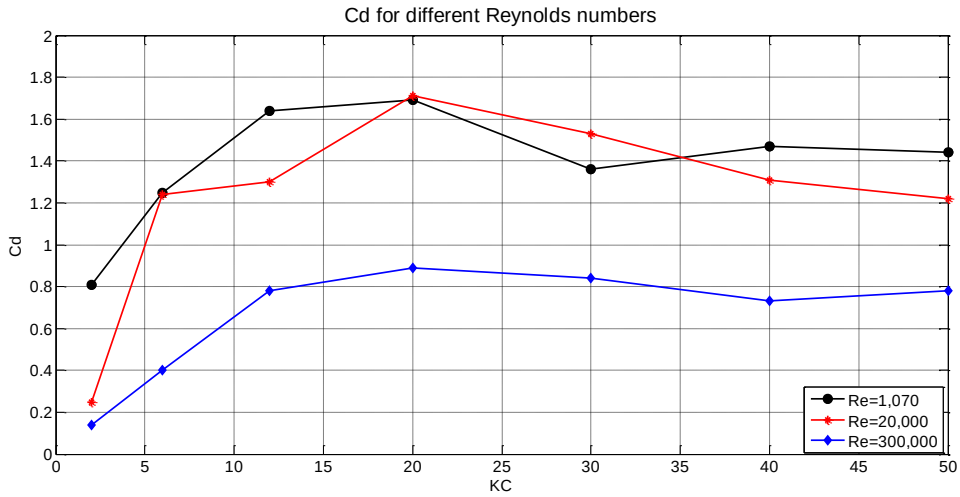

Figure 5.26 C_D vs. KC

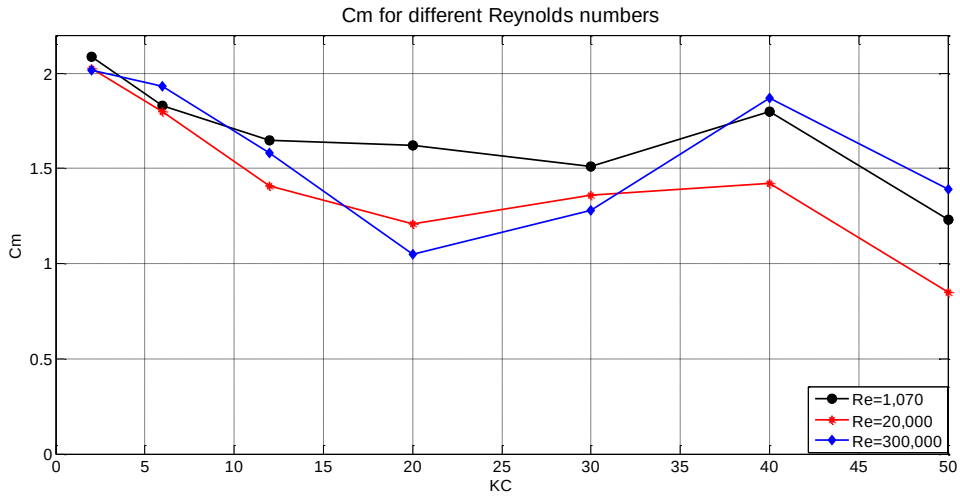

Figure 5.27 C_M vs. KC

American Petroleum Institute (API) also provides the values of C_D and C_M corresponding to different KC numbers. For most offshore structures in the extreme design environment, Reynolds number are well into the post-critical flow regime, where C_D , C_M and C_{ds} for cylinders are independent of Reynolds number (RP2A-WSD 2000). Thus, the results of C_D and C_M for Re=300,000 from this study and those from API are compared. The black solid line denotes the result from API and the blue line denotes the result from this study. Figure 5.28 shows the comparison of C_D for KC<12. C_D is normalized by C_{ds}, which is 0.6 for smooth cylinders and K denotes KC. Figure 5.29 shows the comparison of C_D for larger KC numbers and KC is normalized by C_{ds}. Figure 5.30 shows the comparison of C_M for KC<12. Figure 5.31 shows the comparison of C_M for larger KC numbers and KC is normalized by C_{ds} .

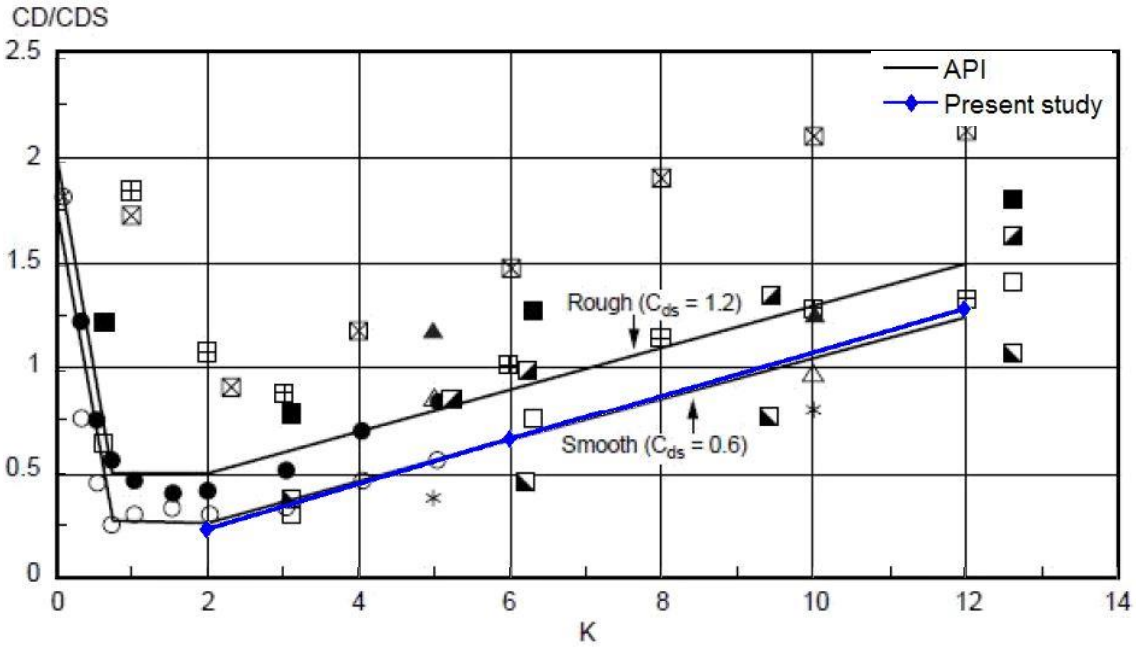

Figure 5.28 Comparison of C_D for KC<12

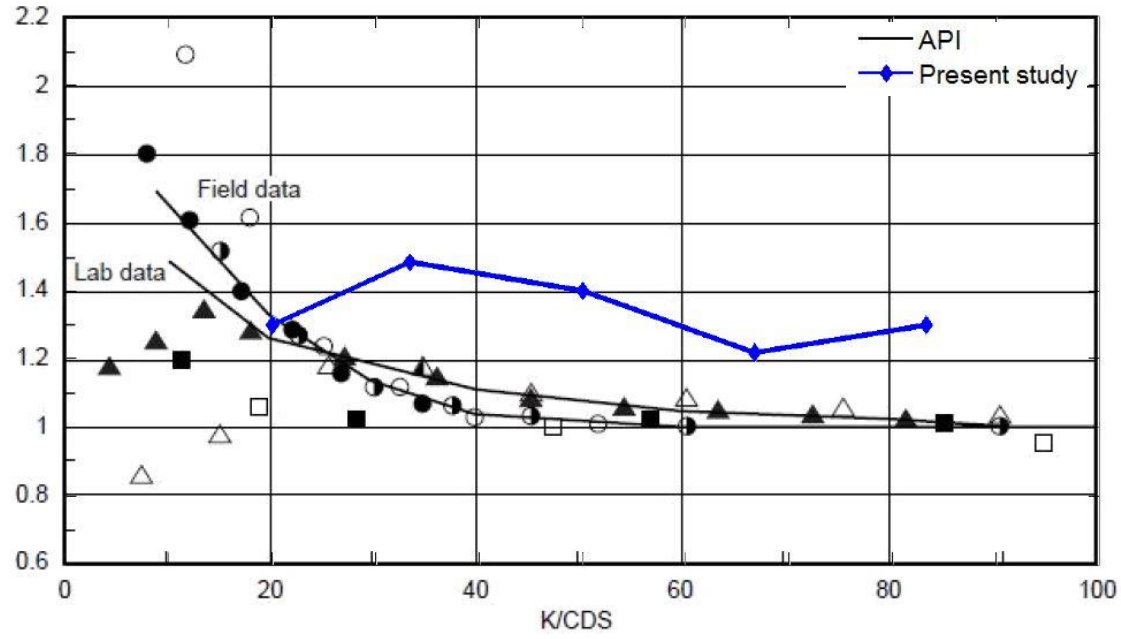

Figure 5.29 Comparison of C_D for larger KCs

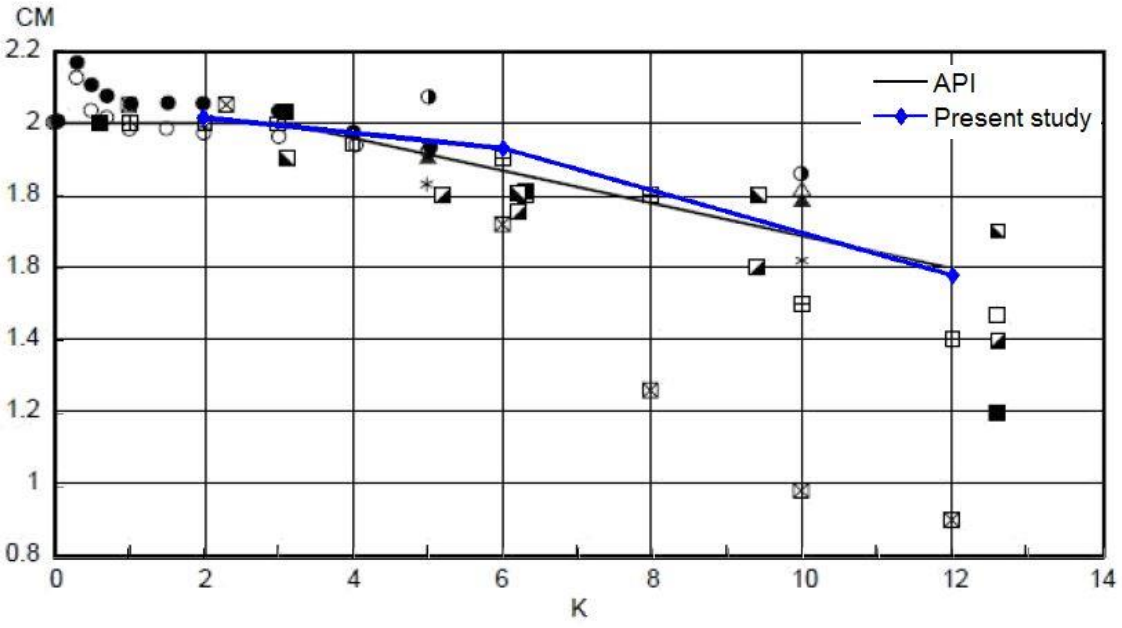

Figure 5.30 Comparison of C_M for KC<12

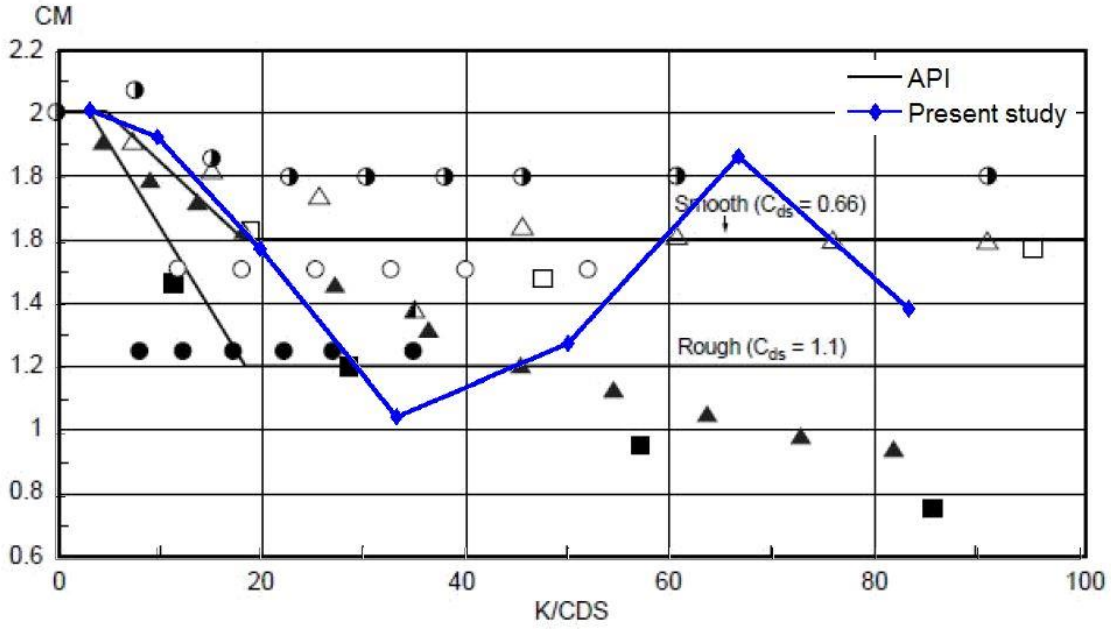

Figure 5.31 Comparison of C_M for larger KCs

For KC<12, the result from this study can match that provided by API very well for both C_D and C_M. However when KC>12, the results from this study tend to provide larger values of C_D and C_M than those of API. A possible reason for this discrepancy might be that the flow domain shown in Figure 5.2 needs to be enlarged for higher KC numbers. This is something that needs to be studied further.

5.4 Effects of turbulence models

In order to study the effect of turbulence models on the result, several cases are run with the Reynolds Stresses model and compared with the results from RANS $k-\omega\ sst$.

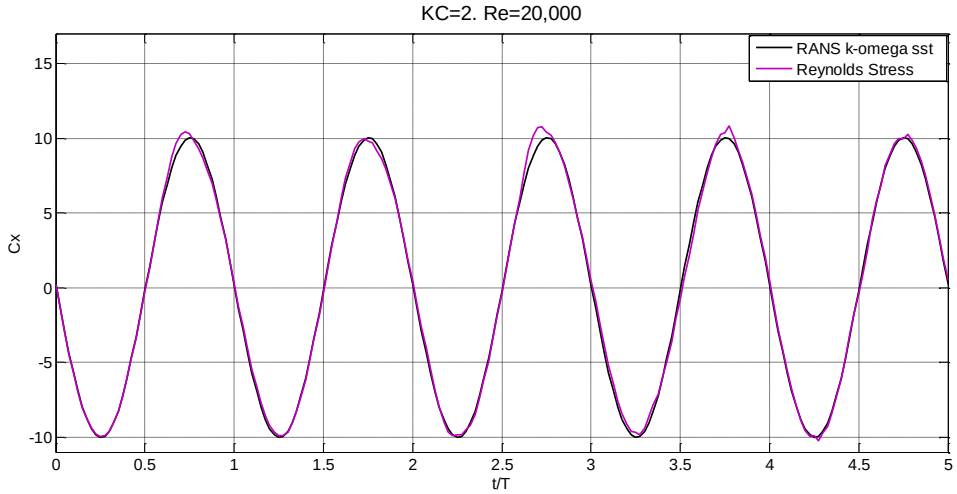

Figure 5.32 Comparison of C_x for KC=2, Re=20,000 of two models

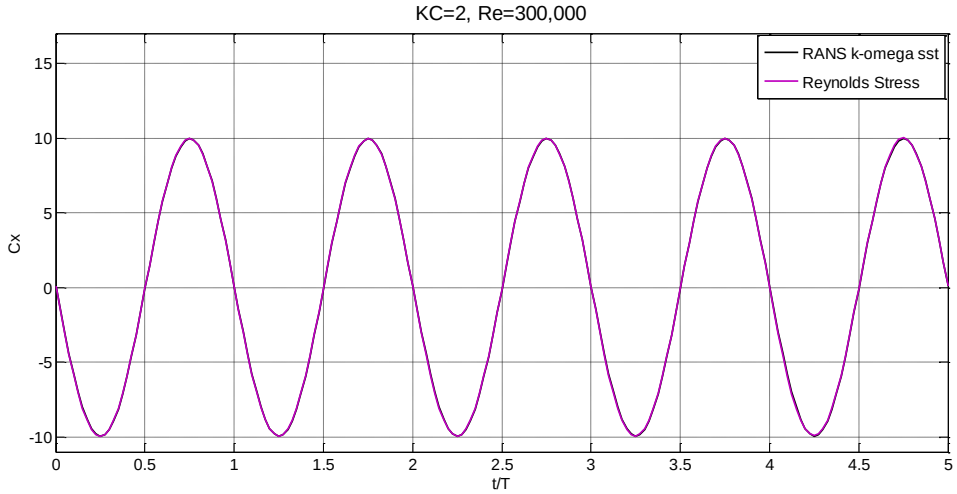

Figure 5.33 Comparison of C_x for KC=2, Re=300,000 of two models

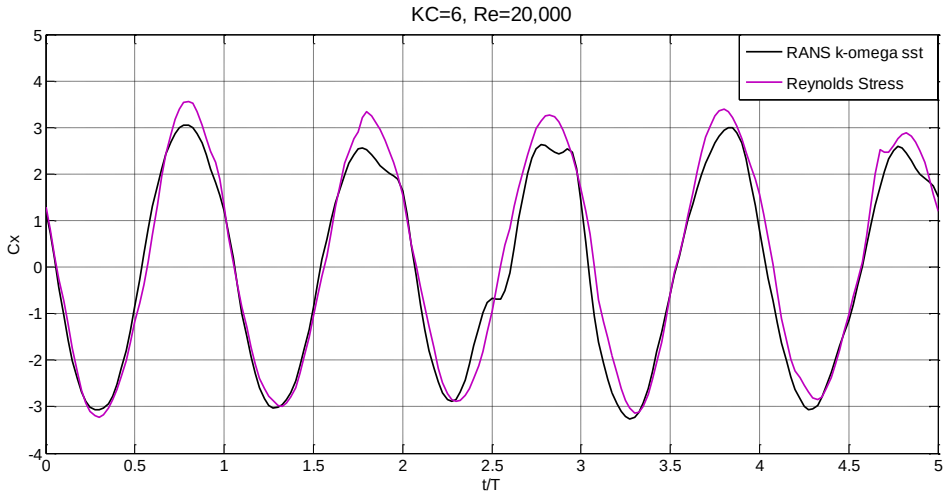

Figure 5.34 Comparison of C_x for KC=6 Re=20,000 of two models

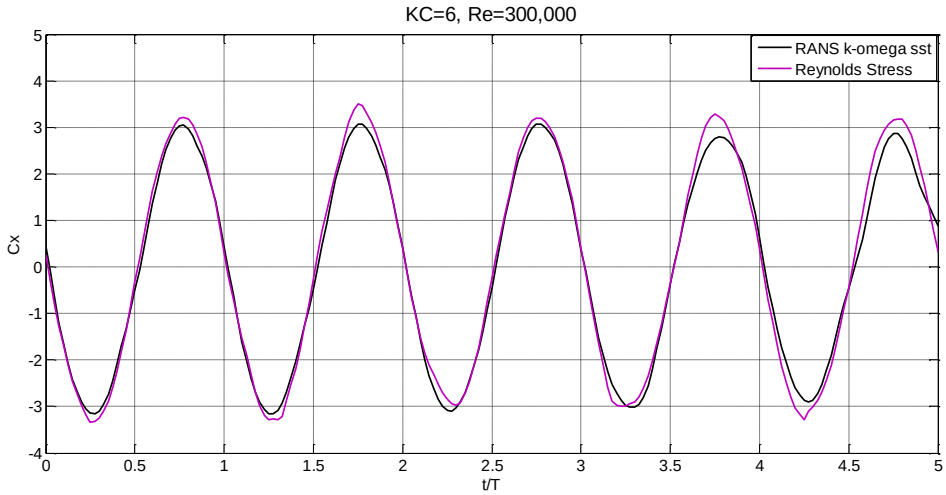

Figure 5.35 Comparison of C_x for KC=6, Re=300,000 of two models

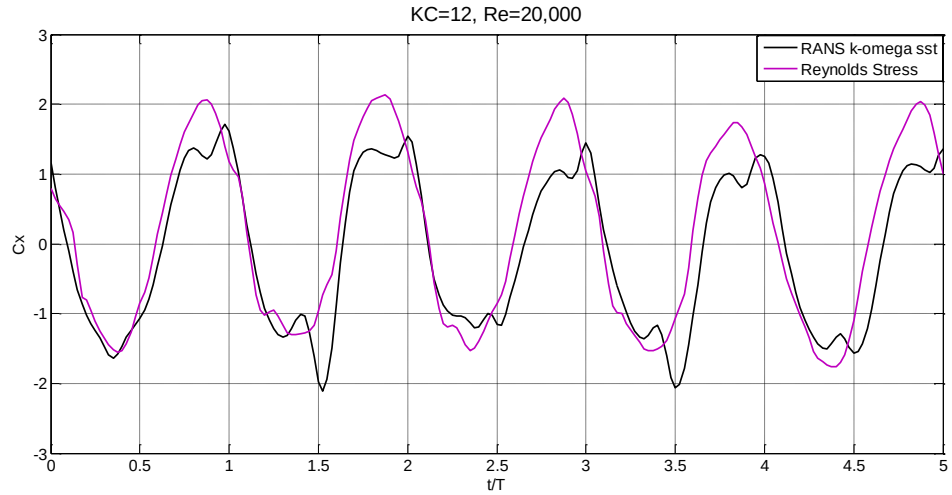

Figure 5.36 Comparison of C_x for KC=12, Re=20,000 of two models

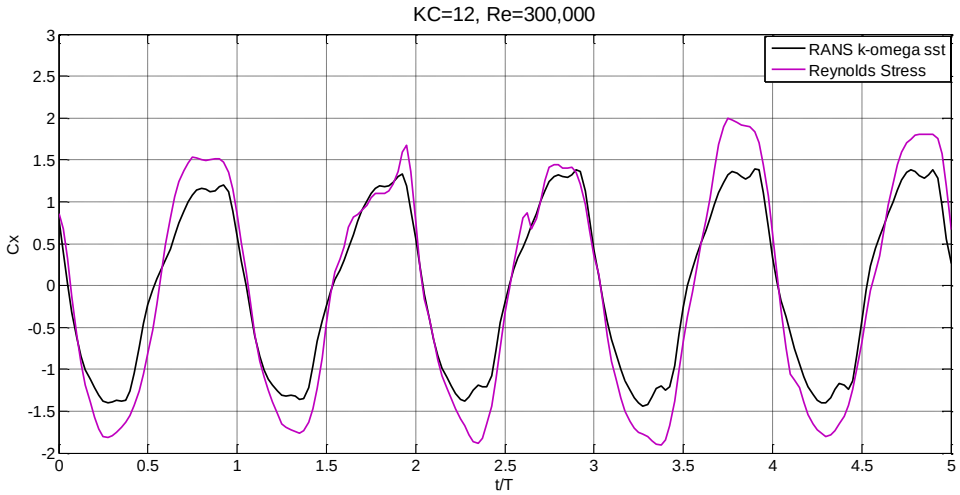

Figure 5.37 Comparison of C_x for KC=12, Re=300,000 of two models

In Reynolds Stress model, the maximum values of C_x tend to be larger than those in RANS $k-\omega\ sst$. When KC=2, the difference between two models is not significant. With the increase of KC, the difference between results from two models becomes more

significant. Especially when KC=12 and Re=300,000, the percentage of difference between two models reaches about 33%.

5.5 Least squares error method to evaluate C_D and C_M

The method of least squares error is an alternative way to evaluate C_D and C_M. It can be done by the application of Curve Fitting Tool in Matlab. The comparisons between the two methods to evaluate C_D and C_M is are made for three different combinations of KC and Re (Figure 5.38, Figure 5.39 and Figure 5.40). In addition, the corresponding values of C_D and C_M from two methods are shown in Table 5.2. The comparisons indicate that the difference between the two methods is quite small. The maximum values from both methods are nearly the same and the shapes of profiles are pretty similar to each other.

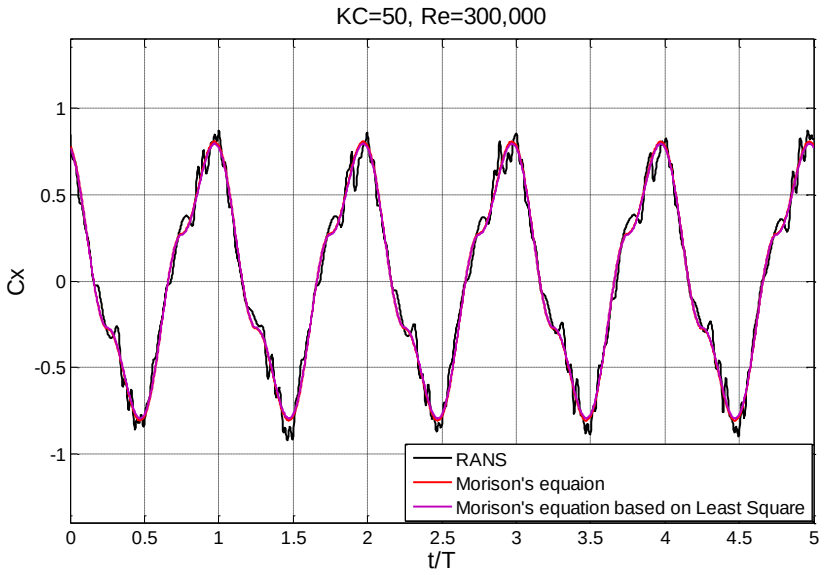

Figure 5.38 Comparison of C_x for KC=50, Re=300,000 of two methods

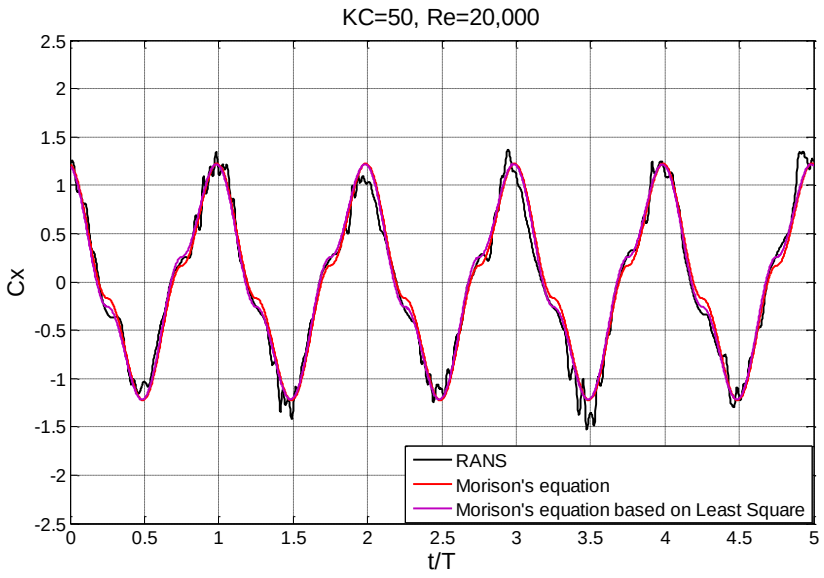

Figure 5.39 Comparison of C_x for KC=50, Re=20,000 of two methods

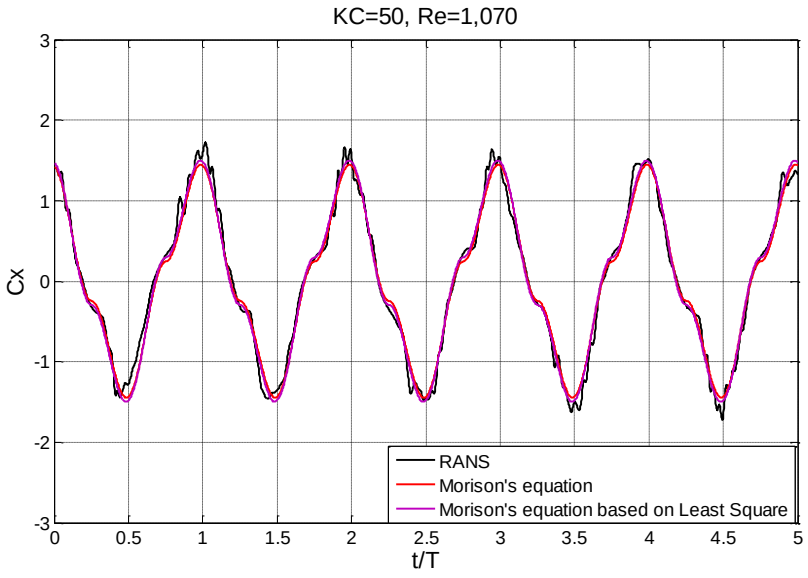

Figure 5.40 Comparison of C_x for KC=50, Re=1,070 of two methods

Table 5-2 Comparison of C_D and C_M of two methods

		Least Squares Error	Integral method
KC=50	C_D	0.77	0.78
Re=300,000	C_M	1.36	1.39
KC=50	C_D	1.21	1.22
Re=20,000	C_M	1.29	0.85
KC=50	C_D	1.48	1.44
Re=1,070	C_M	1.47	1.23

Chapter 6 Conclusions and Future Work

6.1 Conclusions

It is not a trivial task to measure and interpret the turbulent flow around a cylinder via PIV, nor is the task of accurately predicting the flow in two-dimensional and three-dimensional CFD simulations.

The periods of vortex shedding in PIV experiment and CFD simulations are nearly identical to each other, which are also the same as the Strouhal period. Based on the comparison with PIV experiment, both RANS and LES can provide a good prediction of the velocity at specific points, concerning mean values and magnitudes, at the upstream of the cylinder, where the vortex shedding has not happened.

At the downstream of the cylinder, where the vortex shedding occurs, two dimensional RANS is unable to capture the flow characteristics, such as velocity magnitudes, velocity vector fields, time-averaged velocities and Reynolds stresses. However, the three dimensional LES has a better performance in predicting these flow characteristics at the downstream of the cylinder. The possible reason for different performance of 2D RANS and 3D LES is the three dimensionality of the phenomenon of vortex shedding.

A method based on the time history of in-line force, which is from CFD simulations or experiments, to evaluate drag and inertia coefficients for Morison's equation has been presented. Despite the well-known oversimplification of Morison's equation this method

is found to be useful based on the comparison between results of Morison's equation and data from CFD simulations for different combinations of Reynolds numbers and Keulegan–Carpenter numbers. Nevertheless, for several combinations of Re and KC numbers, the detailed time history of the predicted inline force from ANSYS Fluent is quite different from that provided from Morison's equation. The small differences between this method and least squares error method also suggest that the method presented in this study is successful. In addition, the relationship between the drag coefficient and Keulegan–Carpenter numbers is analyzed, as well as that between the inertia coefficient and Reynolds numbers and compared with other experiments.

6.2 Future Work

To have a better understanding of the three dimensionality of vortex shedding, it is necessary to have a good measurement of flow at different planes in the spanwise direction. In this study, the PIV system is two dimensional. If available, a three dimensional PIV system will help a lot to understand the complex turbulent flow at the downstream of cylinder.

In order to have direct drag and lift coefficients comparisons, it is necessary to incorporate the force measurement in the flume experiment or to deduce the forces from the flow characteristics around cylinder.

In Ansys Fluent, Smagorinsky–Lilly model is the only choice of sub-grid scale model for LES. If possible, it would be good to try some other sub-grid models, such as dynamic models, functional (eddy-viscosity) models, etc.

The flow domain shown in Figure 5.2 needs to be enlarged for higher KC numbers in order to get better results for cases of higher KC numbers. In this study, the range of Keulegan–Carpenter number is$0\sim50$. However, in offshore engineering, the KC number can reach 100. So analyses of cases for larger Keulegan–Carpenter number are needed, which could better meet the requirements of designing offshore structures.

Appendix 1 Grid Convergence Studies

When performing the CFD simulations, the mesh has been adjusted and improved several times until appropriate Y-plus values are achieved. The original 2D mesh is shown in Figure 7.1 and a closeup near the cylinder is shown in Figure 7.2. Then the mesh is refined in the wake region which is close to the cylinder (Figure 7.3 and Figure 7.4) in order to perform the convergence study, which means determining whether a proper level of grid convergence has been achieved. The number of cells in the original mesh is 45,000 and it is 55,000 in the refined mesh.

The comparisons include the pressure coefficients on the cylinder (Figure 7.5), wall Y-plus values on the cylinder at t=12s (Figure 7.6), contours of vorticities at t=12s (Figure 7.7 and Figure 7.8), and time history of horizontal velocity at point 10 (Figure 7.9). All the comparison above show that adequate grid convergence has been achieved with the original mesh applied in the CFD simulations.

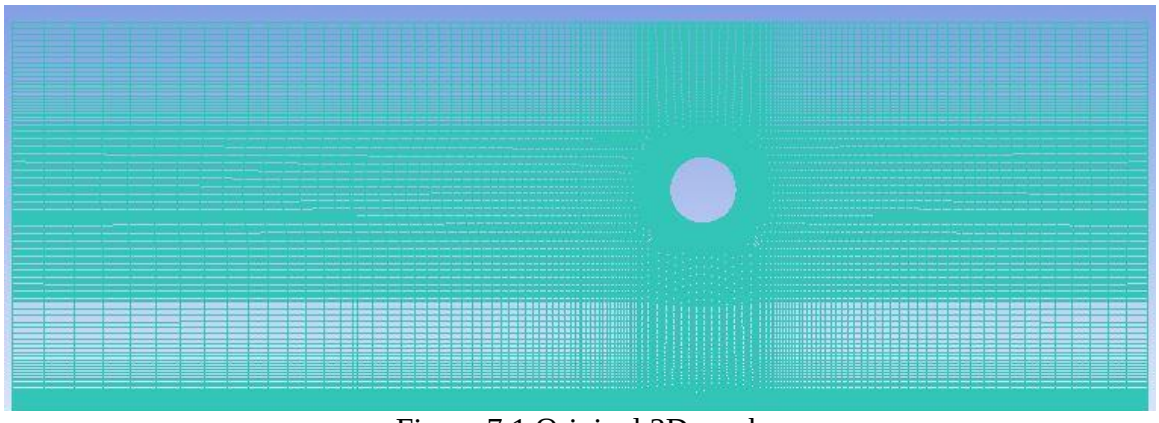

Figure 7.1 Original 2D mesh

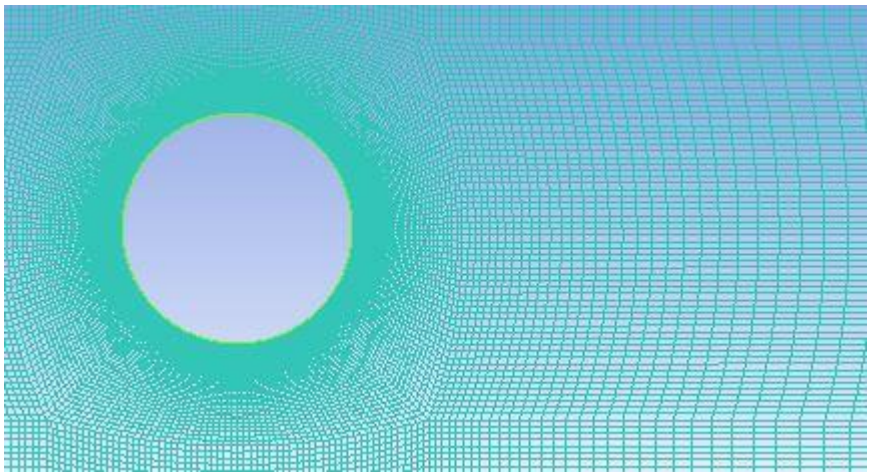

Figure 7.2 Closeup near the cylinder of the original mesh

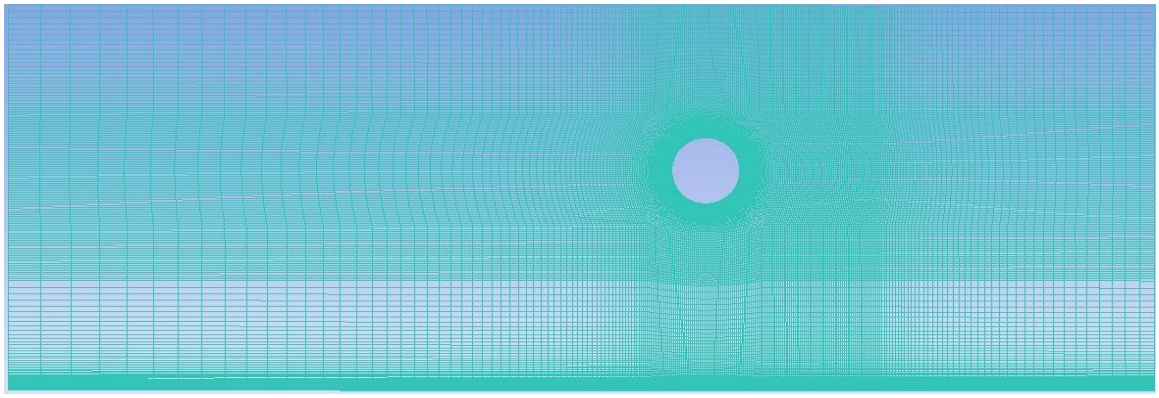

Figure 7.3 Refined 2D mesh

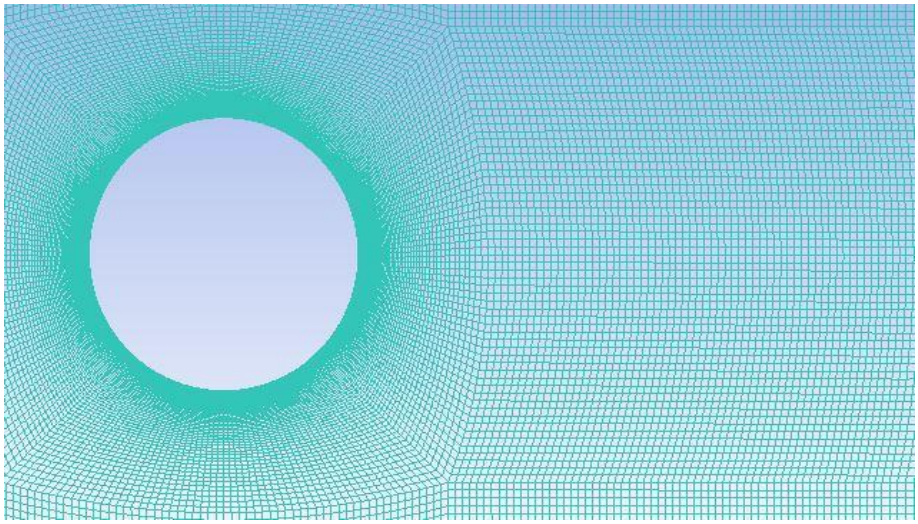

Figure 7.4 Closeup near the cylinder of the refined mesh

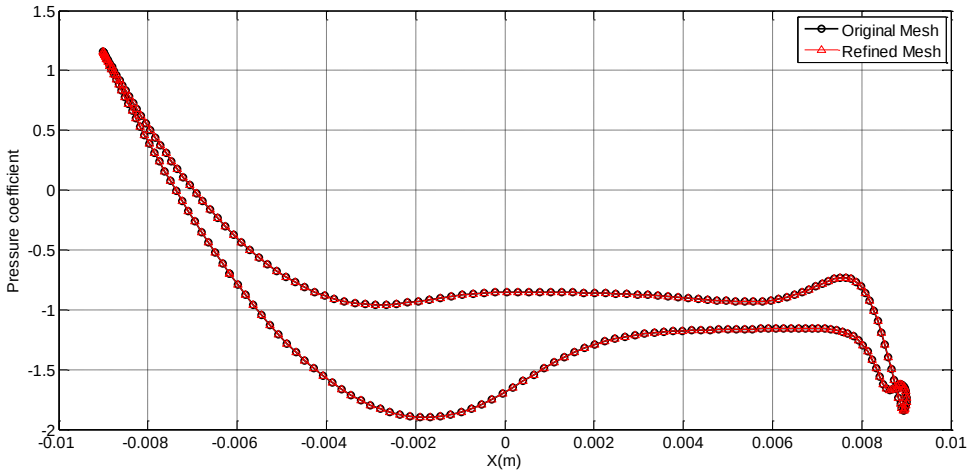

Figure7.5 Comparison of pressure coefficient on the cylinder (t=12s)

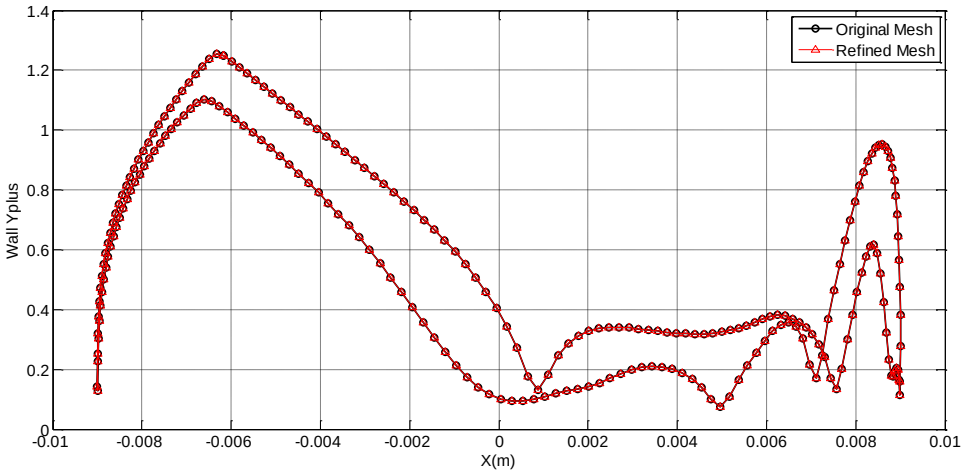

Figure 7.6 Comparison of wall Yplus values on the cylinder (t=12s)

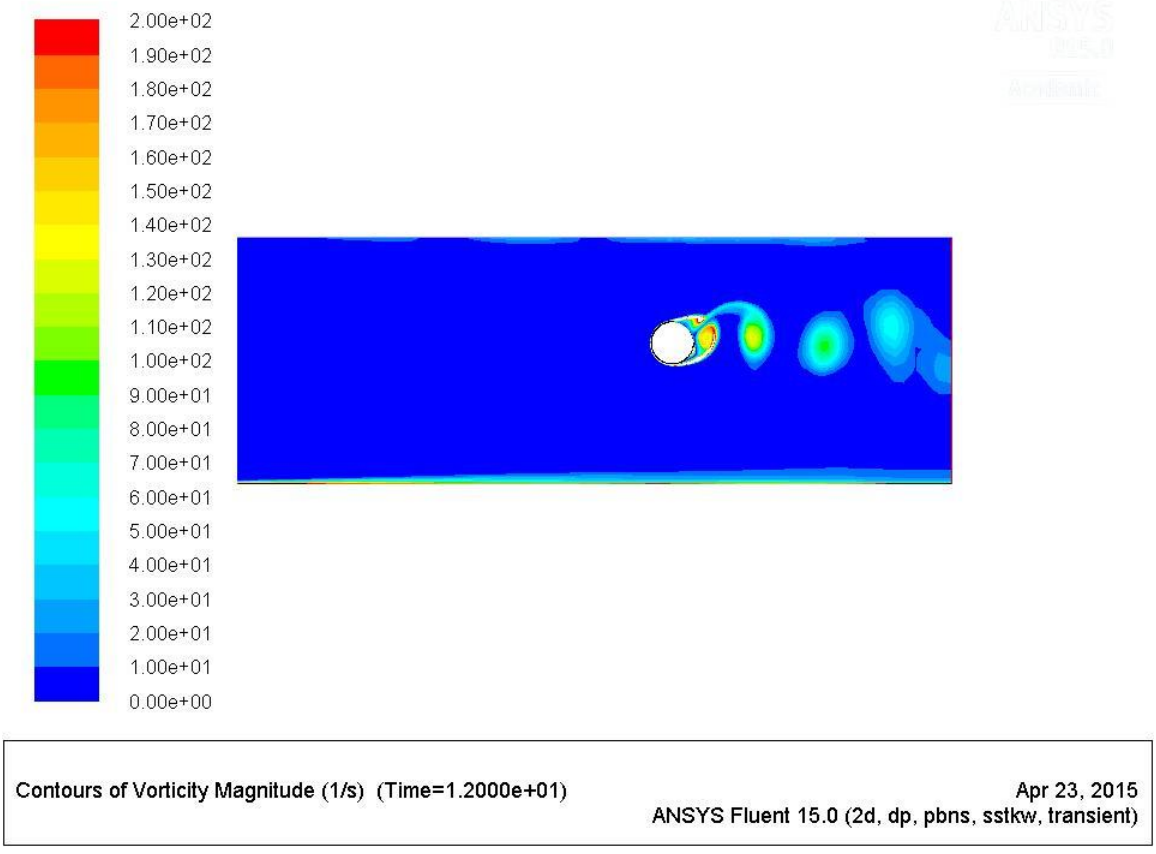

Figure 7.7 Vorticity of the original mesh (t=12s)

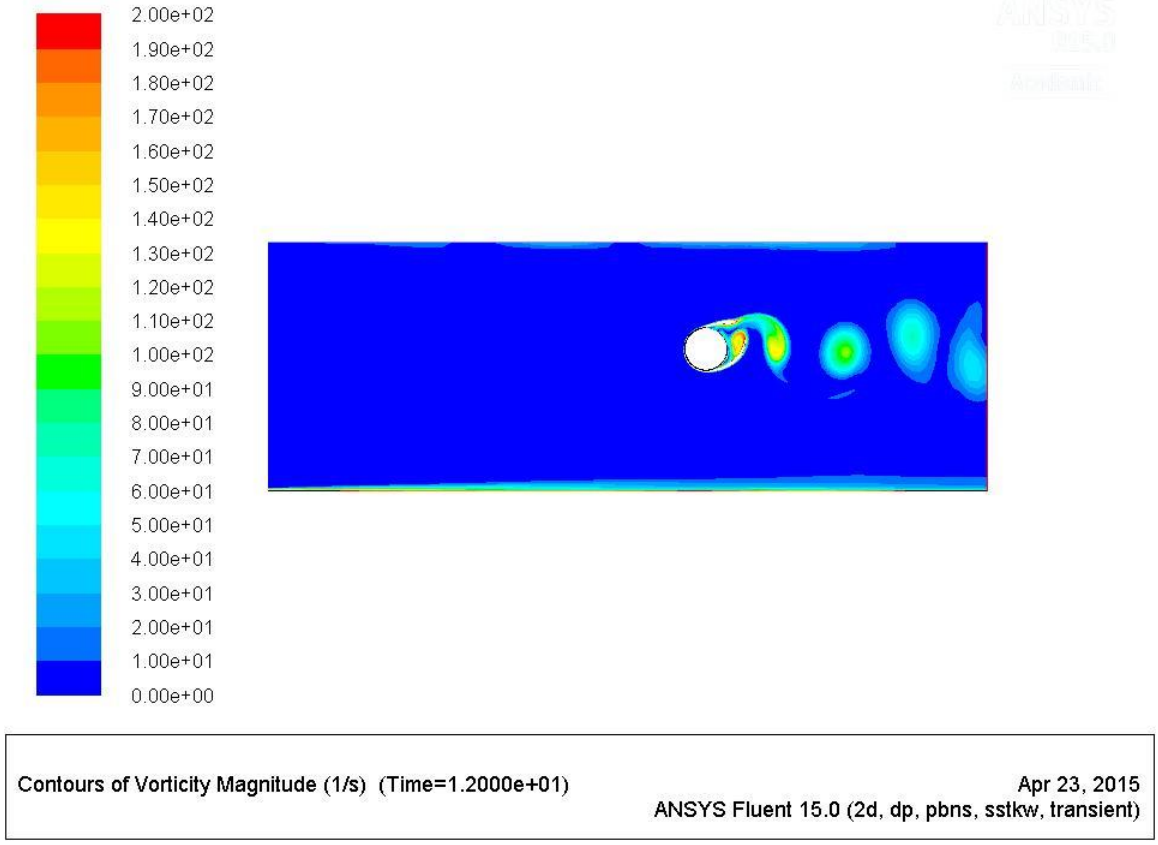

Figure 7.8 Vorticity of the refined mesh (t=12s)

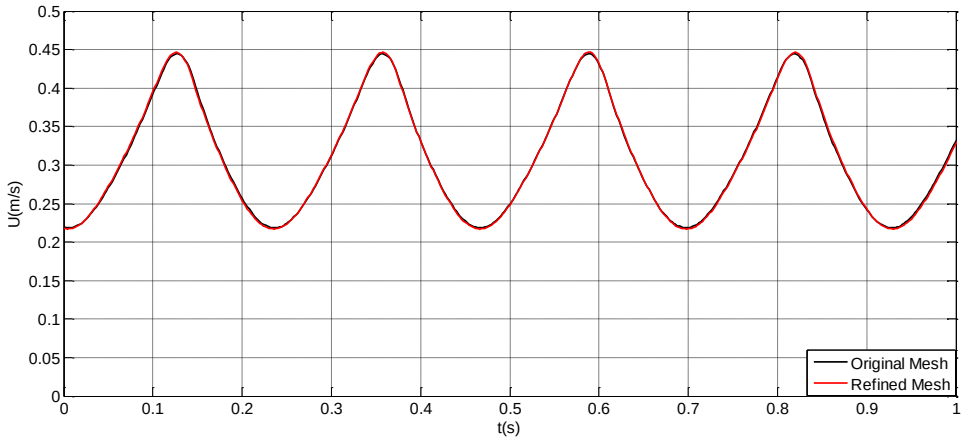

Figure 7.9 Comparison of time history of horizontal velocity at point 10 (Figure 3.16)

Bibliography

[1] Afshar, M. A. and M. javad Ketabdari "Evaluation of Inertia and Drag Coefficients Sensitivity to Pile Inclination using numerical Methods."

[2] Al-Jamal, H. and C. Dalton (2004). "Vortex induced vibrations using large eddy simulation at a moderate Reynolds number." Journal of Fluids and Structures 19(1): 73-92.

[3] Asyikin, M. T. (2012). "CFD Simulation of Vortex Induced Vibration of a Cylindrical Structure."

[4] Bearman, P. W. (1984). "Vortex shedding from oscillating bluff bodies." Annual Review of Fluid Mechanics 16(1): 195-222.

[5]Blackburn, H. M., R. Govardhan and C. Williamson (2001). "A complementary numerical and physical investigation of vortex-induced vibration." Journal of Fluids and Structures 15(3): 481-488.

[6] Burrows, R., R. Tickell, D. Hames and G. Najafian (1997). "Morison wave force coefficients for application to random seas." Applied Ocean Research 19(3): 183-199.

[7] Eswaran, V. and G. Biswas (2002). Turbulent flows: fundamentals, experiments and modeling, CRC Press.

[8] Gabbai, R. and H. Benaroya (2005). "An overview of modeling and experiments of vortex-induced vibration of circular cylinders." Journal of Sound and Vibration 282(3): 575-616.

[9] Garrison, C. (1980). A review of drag and inertia forces on circular cylinders. Offshore Technology Conference, Offshore Technology Conference.

[10] Hanjalic, K. and B. Launder (1972). "A Reynolds stress model of turbulence and its application to thin shear flows." Journal of fluid Mechanics **52**(04): 609-638.

[11] Huang, Z. (2011). CFD simulation of riser VIV, Texas A&M University.

[12] Kang, Z. and L. Jia (2013). "An experiment study of a cylinder's two degree of freedom VIV trajectories." Ocean Engineering 70: 129-140.

[13] Keulegan, G. H., G. H. Keulegan and L. H. Carpenter (1958). "FORCES ON CYLINDERS AND PLATES IN AN OSCILLATING FLUID." Journal of research of the National Bureau of Standards (1934) 60(5): 423-440.

[14] Morison, J., J. Johnson and S. Schaaf (1950). "The force exerted by surface waves on piles." Journal of Petroleum Technology 2(05): 149-154.

[15] RP2A-WSD, A. (2000). Recommended practice for planning, designing and constructing fixed offshore platforms–working stress design

[16] Shur, M., P. R. Spalart, K. D. Squires, M. Strelets and A. Travin (2005). "Three-Dimensionality in Reynolds-Averaged Navier-Stokes Solutions Around Two-Dimensional Geometries." AIAA journal 43(6): 1230-1242.

[17] Stetson, P. B. (2013). "PIV measurements of flow-field downstream of a cylinder with and without fairing and comparison with CFD."

[18] Verma, A. and K. Mahesh (2012). "A Lagrangian subgrid-scale model with dynamic estimation of Lagrangian time scale for large eddy simulation of complex flows." Physics of Fluids (1994-present) 24(8): 085101.

[19] Wade, B. G. and M. Dwyer (1978). "Application of morison's equation to fixed offshore platforms." J. Pet. Technol 30(3): 447-454.

[20] Wang, Q., M. Li and S. Xu (2014). "Experimental study on vortex induced vibration (VIV) of a wide-D-section cylinder in a cross flow." Theoretical and Applied Mechanics Letters 5(1): 15-20.

[21] Wilde, J.J. de, Huijsmans, R.H.M., Tukker, J., "Experimental investigation into the vortex formation on the wake of an oscillation cylinder using Particle Image Velocimetry", submitted ISOPE 2006.

[22] Williamson, C. (1988). The existence of two stages in the transition to three-dimensionality of a cylinder wake, DTIC Document.

[23]Williamson, C. H. (1988). "Defining a universal and continuous Strouhal–Reynolds number relationship for the laminar vortex shedding of a circular cylinder." Physics of Fluids (1958-1988) **31**(10): 2742-2744

[24] Zhou, C. and J. Graham (2000). "A numerical study of cylinders in waves and currents." Journal of Fluids and Structures 14(3): 403-428.

Vita

Guangyao Wang was born in Cangzhou, Hebei, China. He received the Bachelor of Science in Port, Channel and Coast Engineering from Tianjin University, China in July, 2013. In August 2013, he started his graduate studies as member of the Ocean Engineering Group at the University of Texas at Austin.

Address:gw5923@utexas.edu

This manuscript was typed by Guangyao Wang.